

**Numerical Modeling of Two-Phase Flow for Solitary Porosity Waves
and Transport of Trace Elements within Melt**

Dissertation
zur Erlangung des Doktorgrades
der Naturwissenschaften

vorgelegt beim Fachbereich 11, Geowissenschaften/Geographie
der Johann Wolfgang Goethe-Universität
in Frankfurt am Main

von
Janik Dohmen
aus Viersen

Frankfurt 2022
(D30)

vom Fachbereich 11 Geowissenschaften/Geographie der
Johann Wolfgang Goethe-Universität Dissertation angenommen.

Dekan: Prof. Dr. Jürgen Runge

Gutachter: Prof. Dr. Harro Schmeling und Prof. Dr. Thibault Duretz

Datum der Disputation: 14.4.2023

"Mostly Harmless"

— THE GUIDE'S DESCRIPTION OF EARTH

The Hitchhiker's Guide to the Universe
Douglas Adams

Abstract

Melting inside Earth is a common phenomenon and can be observed in many different regions where melt travels through the mantle and crust to eventually reach the surface where it crystallizes to build large volcanic provinces, whole stratigraphic layers of flood basalts, or even the oceanic crust. Often, melt reaching the surface is a good source of information. It can be used to achieve a better understanding about processes taking place in deeper regions inside the mantle and it is therefore essential to fundamentally understand melting and melt percolation processes. In order to achieve a deeper understanding, the aim of this thesis is to investigate processes that are connected to melting by using numerical models.

The physical model used is a so called *two-phase flow* model which describes the ability of melt to percolate through a viscously deforming, partially molten matrix. A famous feature of *two-phase flow* are *solitary porosity waves*, which are waves of locally higher porosity ascending through a partially molten background, keeping its shape constant, driven by decompaction and compaction of the solid matrix in front and behind the wave.

The viscosity law for shear- and volume viscosity was strongly simplified in most previous studies that modeled solitary waves. Often the porosity dependency is underestimated or its influence on the volume viscosity is even neglected, leading to too high viscosities. In this work more realistic laws are used that strongly decrease for small melt fractions. Those laws are incorporated into a 2D Finite Difference mantle convection code with two-phase flow to study the ascent of solitary porosity waves.

The model results show that an initial Gaussian-shaped wave rapidly evolves into a solitary wave with a certain amplitude, traveling upwards with constant velocity. Even though strongly weaker viscosities are used, the effect on dispersion curves and wave shape are only minor as long as the background porosity is rather small. The results are still in agreement to semi-analytical solutions which neglect shear stresses in the melt segregation equation. Higher background porosities and wave amplitudes lead to significant decrease in phase velocity and wave width, as the viscosity is strongly affected. However, the models show that solitary waves are still a possible mechanism for more realistic matrix viscosities.

While the ascending of porosity waves are mostly described by the movement of fluid melt, partially molten regions inside Earth trigger upwelling of both, solid and fluid phases, which can be called diapirism. While diapirs can have a wide variety of wavelengths, porosity waves are restricted to a few times the compaction length. The size of a melt perturbation in terms of compaction length therefore describes whether material is transported by diapirism or porosity waves. In this thesis we study the

transition from diapiric rise to solitary porosity waves by systematically changing the size of a porosity perturbation from 1.8 to 120 times the compaction length. In case of a perturbation of the size of a few times the compaction length a single porosity wave will emerge, either with a positive or negative vertical matrix flux and if melt is not allowed to move relative to the matrix a diapir will emerge. In between these physical end members a regime can be observed where the partially molten perturbation will split up into numerous solitary waves, whose phase velocity is low compared to the Stokes velocity and the swarm of solitary waves will ascend jointly as a diapir, slowly elongating due to a higher amplitude main solitary wave.

Solitary waves will always emerge from a melt perturbation as long as two-phase flow is enabled, but the time for a solitary wave to emerge increases non-linearly with the perturbation radius in terms of compaction length. In nature, in many cases this time might be too long for solitary waves to emerge.

Another important feature when it comes to two-phase flow is the transport of trace elements in melt. Incompatible elements prefer to go into the melt, which eventually enriches the area where it crystallizes again. In order to model this redistribution, the code FDCON was extended to allow for fully consistent transport of elements in melt, including melting, freezing and re-equilibration with time. A 2D model, a simple representation of a volcanic back arc, is set up to investigate the behavior of trace elements. The influence of retention number and re-equilibration time is examined. Lava-lamp like convection can be observed in the lower part of the model, producing melt, that eventually leads to enrichment in trace elements in the upper high-viscous layer. The total enrichment in this layer approaches an asymptotic value and a 0D model is introduced to recreate this behavior. Additionally to geochemical parameters it incorporates parameters describing the movability of melt, the ratio of source area to emplacement area, and the ratio of molten to unmolten area in the source region, i.e. the dynamics of the model. The amount of enrichment in the emplacement area will reach an asymptotic value, that depends on the three additional parameters mentioned above, the partition coefficient, re-equilibration and degree of melting. The time that is needed to approach the asymptote only depends on the ratio of molten to unmolten area in the source region, as this is an indicator on how strong the source becomes depleted per melting event.

Solitary waves are also interesting when it comes to their mass transport capabilities. In the past it was long thought that they are not able to transport mass, that they just pass through material, during which the latter is slightly ascended. Recently, it was shown that solitary waves are in fact able to encapsulate material in their center and transport material until they vanish at one point due to obstacles. In this work we could reproduce these mass transport capabilities, using the full two-phase flow equations, allowing for the self consistent evolving of solitary waves. It could be shown that the material trapped in the center of the wave is not from the melt source region, but from a region slightly above, because the wave needs some time to build up and to encapsulate material in it.

Contents

Abstract	i
Contents	v
List of Figures	viii
List of Tables	ix
1 Motivation and Aim of this Thesis	1
2 Introduction	3
2.1 Partial Melting inside Earth and Melt Transport	3
2.2 Diapirism and Solitary Porosity Waves	6
2.3 Trace Elements and their Behavior during Melting	11
3 Methods	21
3.1 General Equations of Two-Phase Flow	21
3.2 Equations of Trace Element Transport with Melt	27
3.3 Derivation of the Equations in the Publications	30
3.3.1 Publication 1	30
3.3.2 Publication 2	32
3.3.3 Publication 3	33
3.3.4 Unpublished Manuscript	35
4 Publication 1: The Effect of effective Rock Viscosity on 2D Magmatic Porosity Waves	37
4.1 Introduction	38
4.2 Theoretical Approach	39
4.2.1 Governing Equations	39
4.2.2 The effective Viscosity of a Porous Matrix	41
4.2.3 Methods and Model Setup	42
4.3 Results	44
4.3.1 Dispersion Curves for varied Widths and Amplitudes	44
4.3.2 Effect of different Viscosity Laws for $n=2$ and 3 on Dispersion Curves	46
4.4 Discussion	50

4.5	Conclusion	52
5	Publication 2: Magma ascent mechanisms in the transition regime from solitary porosity waves to diapirism	55
5.1	Introduction	56
5.2	Methods	57
5.2.1	Governing Equations	57
5.2.2	Model Setup	62
5.2.3	Numerical Approach	62
5.3	Results	64
5.3.1	The Transition from Porosity Wave to Diapirism: Varying the initial Wave Radius	64
5.3.2	Effects on the Mass Flux	67
5.4	Discussion	70
5.4.1	Application to Nature	70
5.4.2	Model Limitations	71
5.5	Conclusion	72
6	Publication 3: Modeling trace element transport in melt using two-phase flow: Investigation of element redistribution in the upper Earth	77
6.1	abstract	77
6.2	Introduction	78
6.3	Methods	79
6.3.1	Governing Equations for Two-Phase Flow	79
6.3.2	Equations for Trace Element Transport	82
6.3.3	Model Setup	85
6.4	Results	87
6.5	Discussion	95
6.6	Conclusions	98
7	Unpublished manuscript: Transport of volatiles and trace elements in solitary porosity waves	103
7.1	Introduction	104
7.2	Governing Equations	104
7.3	Results	106
7.3.1	Passing through an Enriched Layer	106
7.3.2	Origin of the Encapsulated Material	109
7.4	Conclusions	110
8	Conclusions	115
9	Fazit	119
10	Zusammenfassung	123
	Personal Contribution to Publications	129

Eidesstattliche Erklärung

131

List of Figures

2.1	Global distribution of volcanoes active in Quaternary.	4
2.2	Visualization of causes for melting inside the upper 250 km of the Earth.	5
2.3	Seismic section of a salt diapir in Angola from Schultz-Ela et al. (1993).	7
2.4	A photograph of a laboratory plume.	8
2.5	Decay of a 1-D solitary wave into several 2-D waves.	9
2.6	A swarm of elongated solitary waves, due to decompaction weakening.	10
2.7	Ionic radius versus ionic charge for some important trace elements.	15
2.8	Trace Element concentrations of fluid and solid during melting and crystallization.	16
3.1	A simple phase-diagram for a two-component solid phase.	27
4.1	Shear and bulk viscosity for several aspect ratios as a function of the melt fraction.	43
4.2	a) Non-dimensional melt fraction during the ascent of a solitary wave. b) Horizontal cross section through the center of the initial wave and the solitary wave at a later time.	45
4.3	Dispersion curves for three models with an initial width bigger, smaller and approximately equal to the resulting solitary wave.	46
4.4	Dispersion curves for 44 models with 4 different initial amplitudes and 11 different initial widths each.	47
4.5	Dispersion curves of solitary waves with different n and melt network geometries.	48
4.6	Non-dimensional half-width, plotted against non-dimensional phase velocity for different viscosity laws.	49
4.7	Matrix velocity in the center of a wave as a function of the aspect ratio of the films.	50
4.8	a) Horizontal profiles through ascending waves and b) dispersion curves with different background porosities but the same non-dimensional amplitude.	51
5.1	The segregation to Stokes velocity ratio given as a function of initial perturbation radius.	61
5.2	Depiction of a model with an initial perturbation radius of 12 times the compaction length but with different numerical grid resolutions.	63

5.3	Melt ascent morphology as function of initial perturbation radius in terms of compaction length.	65
5.4	Solitary wave phase velocity compared to Stokes sphere velocity.	66
5.5	Solid and fluid mass fluxes through solitary waves and the corresponding melt fractions.	68
5.6	Quantitative parameters as function of initial perturbation radius in terms of compaction length.	69
6.1	Comparison of numerical results to literature equations for fractional and equilibrium melting and freezing.	86
6.2	Typical model states of an uprising partially molten plume.	87
6.3	Three time steps of the trace element concentration in a rising plume.	88
6.4	Logarithmic total concentrations of a model with after four different melting events.	90
6.5	Conceptual sketch of a 0D model representing trace element redistribution in a closed convection system.	91
6.6	a) Horizontally averaged vertical profiles of the total concentration after four different melting events. b) Comparison of 2D model results with a 0D model.	93
6.7	Horizontally averaged vertical profiles of 2D models with a) different retention numbers and b) different reaction times.	95
6.8	Relative concentrations for different trace elements.	97
7.1	The total concentration of a trace element at the point where the solitary waves have reached $z' = 0.7$	107
7.2	Non-dimensional phase and segregation velocity as a function of time of a solitary wave.	108
7.3	Marker fields from the models already shown.	109
7.4	Trajectories of a few selected markers.	110
7.5	Marker fields a) in the beginning and b) at the end of a model with a 1D porosity wave initially placed at the bottom of the model box.	111
7.6	Figure shows a zoom of Fig. 7.5b on the second solitary wave from the right.	111

List of Tables

4.1	Parameters to calculate the viscosities for a melt network consisting of 50% tubes and 50% films using Eqs. (4.26) and (4.27)	42
-----	---	----

Chapter 1

Motivation and Aim of this Thesis

Earth is to the most part a giant solid rock whose interior can be observed or interpreted using for example geophysical measurements like seismics or geomagnetics, but those measurements represent only the current state and give only vague information. Estimates about the past of rocks and minerals can be made using other measurements and observations, but to better understand the physical processes that are happening deep below our feet, the scientific field of geodynamics uses numerical and analog models. As computers became more powerful, numerical models became better, more complicated and included more physical processes taking place inside Earth. One of those processes is the generation and transport of melt through a viscous, partially molten rock matrix, which is called two-phase flow. One big topic in this kind of modeling is *solitary porosity waves*, which are a feature of two-phase flow and, although they were heavily studied in the past 30–40 years, there are still open questions. In this thesis I clarify a few of these questions:

How do solitary porosity waves react to different viscosity laws?

Most of the studies working on solitary waves used simple viscosity laws for the effect of porosity on shear and volume viscosity (e.g. Scott and Stevenson, 1984; Barcilon and Lovera, 1989; Wiggins and Spiegelman, 1995). More realistic viscosity laws predict viscosities strongly decreasing for low porosities and complete disaggregation of the grains for much lower porosities (Schmeling et al., 2012). Can solitary waves build up under these circumstances and how do their properties, like phase velocity and shape, change?

What happens to solitary waves on the transition regime between solitary waves and diapirism?

While most studies either investigate one of these end-members (e.g. Simpson and Spiegelman, 2011; Bittner and Schmeling, 1995), it is still not fully understood what happens at the transition. Do diapirs and solitary waves overlay each other and are there regimes where one of these mechanisms becomes dominant? Under which conditions are solitary waves able to build up and what time do they need to build up? Are they able to build up under natural circumstances or will diapirism always hold back their emergence?

Another big topic with regards to modeling two-phase flow and/or melting is that of trace elements. The measurements of these elements are often an important option to get an idea on what is happening inside the Earth. During the process of melting, chemical elements either prefer to stay in the minerals lattice or prefer to go into the melt. Therefore, the process of melt percolation will lead to a redistribution of these elements, which are observed by geochemists. It is obvious that modeling these processes is of vast interest and there are still open questions:

How are trace elements transported with melt and what parameters lead to enrichment of incompatible elements in the upper Earth?

Incompatible elements prefer to go into the melt during melting and are then transported with the fluid to shallower regions inside the Earth. Trace element concentrations are often used to get information on what has happened to melts and it is therefore important to better understand the dynamics happening and what parameters lead to which degree of enrichment.

What are the mass transport capabilities of solitary porosity waves?

For a long time it was thought that solitary waves are not capable of transporting mass; that a wave just passes through material. But recently it was shown that 2D waves are capable of doing just this (Jordan et al., 2018). For some cases material gets encapsulated in the center of the wave and is transported together with it. What parameters define these cases and, if a solitary wave builds up, from where does the encapsulated material originate?

In this thesis four manuscripts are presented that answer the four points stated above, each manuscript tackling one of the group of questions asked. Before that, a small introduction into the general topics concerning this thesis are given. After that, all the equations describing these mechanisms and the methods used are presented. A conclusion and a German abstract form the end.

Chapter 2

Introduction

2.1 Partial Melting inside Earth and Melt Transport

The Earth is a giant heat emitting rock that travels through space. It emits approximately 46 TW of heat (e.g. Lay et al., 2008; Jaupart et al., 2015; Pollack et al., 1993) from which 8–28 TW comes from mantle cooling, prominently from the lower mantle, and about 5–15 TW are heat flow from the core. Some older estimates (e.g. Sleep, 1990; Stacey and Loper, 1983) predicted only 3–4 TW from the core. Approximately 20 TW are produced by radiogenic heat production. In the early beginning of the solar system a protoplanetary disk surrounded the newly formed sun (e.g. Armitage, 2011) and the dust, of which it consisted, aggregated with time (e.g. Koch et al., 2021; Wood et al., 2006) to build up chondrules, planetesimals and eventually the planets we know today. Energy of collisions happening during this accretion was transformed to heat energy and as Earth grew bigger, gravity pulled material down towards the center. This compression led to further increase of internal heat.

The cooling of Earth is the reason why mantle convection and plate tectonics take place, which are in turn the main processes that lead to partial melting of rocks. On Earth there are two types of volcanism: plate margin and intraplate volcanism. Most volcanoes are connected to plate margins and on a map showing the distribution of recently active volcanoes (Fig. 2.1) one can easily make out the margins (Schubert et al., 2001). However, there are exceptions that are not laying on or at margins, but in the inner regions of plates, and they are usually assumed to be connected to hot mantle plumes. Before one digs deeper into where volcanism takes place one needs to understand what are the processes and causes that lead to melting.

There are three main reasons for melting: decompression, heating and lowering solidus temperature. In Fig. 2.2 the three causes are visualized by vertical temperature profiles.

Decompression melting Roughly the mantle temperature can be approximated to decrease linearly with a certain slope the closer it comes to surface. But the solidus temperature for peridotite (Takahashi, 1986) decreases faster and hot material rising

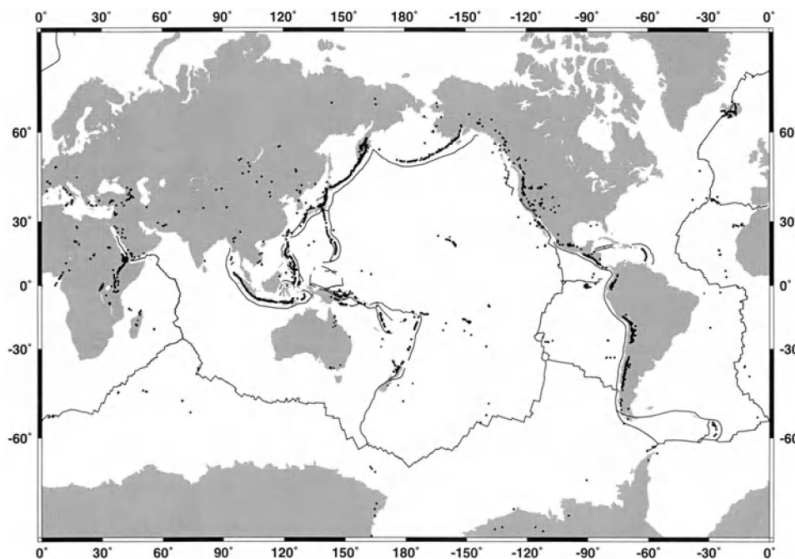


Figure 2.1: Global distribution of volcanoes active in Quaternary (Schubert et al., 2001).

from depth will at some point cross the solidus and partial melting starts. While this is true for relatively fast ascending material, slowly ascending material is cooled due to conduction from the top and never reaches the solidus (see Fig. 2.2a).

Heat-induced melting In several cases material is heated up, which may lead to temperatures exceeding the solidus (see Fig. 2.2b). One of these cases is the arrival of a mantle plume beneath the lithosphere. A mantle plume is the upwelling of hot material from the deep mantle up to the stiff lithosphere, where it spreads and heats up surrounding material, which is the source of melting for hot spot volcanism like the prominent locations of Hawaii or Iceland. Mantle plumes were first postulated by Wilson (1963) and later further developed by Morgan (1971, 1972).

Flux melting When a volatile component like water is added to a rock its solidus temperature can be greatly depressed. For example the solidus of a silicate melt in fertile lherzolite, can be, following Katz et al. (2003), depressed by 150°C for just a water content of 500 ppm. During subduction the oceanic crust carries water into the mantle. The water, which is stored mostly in hydrous minerals, is released into the overlying mantle wedge by metamorphic dewatering (see Alt et al., 1996). Here, magma is generated feeding the volcanic back arc behind the subduction zone.

All the melting that occurs inside the Earth can be related to these three causes. At mid-ocean ridges mantle material erupts that was transported there from the deeper mantle and builds the oceanic crust. On the way up the material becomes partially molten due to decompression melting. As already mentioned, this oceanic crust gets subducted at convergent zones, releasing the water previously incorporated into the minerals, which in turn leads to flux melting at the volcanic back arc. Hot-spot vol-

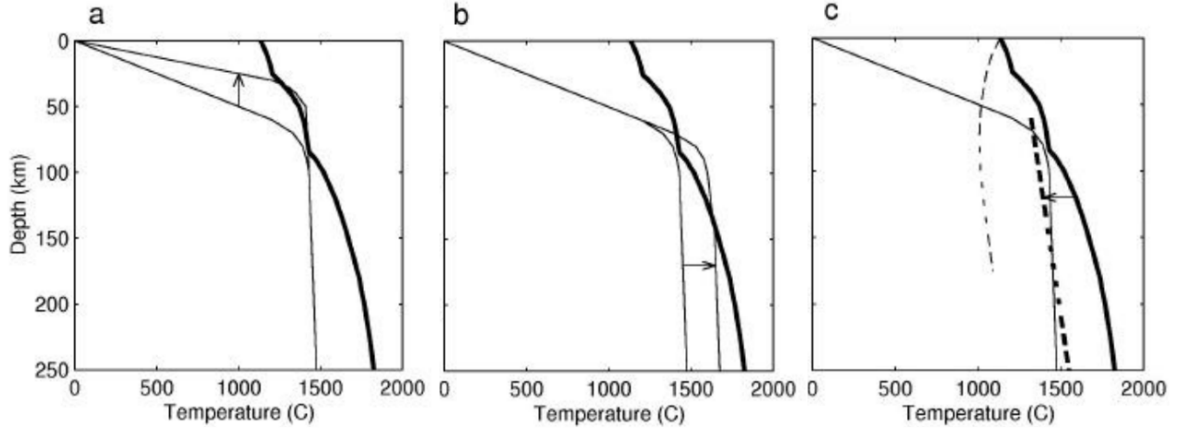


Figure 2.2: Visualization of causes for melting inside the upper 250 km of the Earth (Schmeling, 2000, taken from). Solidus temperatures are taken from Takahashi (1986). Subplots show melting due to a) decompression, b) heating and c) lowering the solidus temperature.

canism or intraplate volcanism like Hawaii or Iceland are the result of heat-induced melting, as a consequence of a hot upwelling mantle plume, heating the lithosphere above.

Above solidus usually a rock is not fully but partially molten. This is due to the fact that a rock consists of several minerals and many of those minerals contain more than one chemical component. This causes melting to start at a temperature called solidus and to end at the liquidus, where a rock is fully molten. In between those temperatures minerals coexist with melt (White, 2018). The Bowen’s reaction series (Bowen, 1922) describes this sequential behavior during freezing, where it is a major reason for differentiation.

Another effect of this partial melting is that the fluid melt has to percolate through the still solid residue of the rock, which can be described by the well known Darcy equation:

$$Q = -\frac{k_\varphi A}{\mu L} \Delta P, \quad (2.1)$$

where Q is the volumetric flow rate, k_φ is the permeability, A is the cross-sectional area, μ is the dynamic fluid viscosity and ΔP is the pressure difference between the distance L . In section 3 of this thesis it is shown how this equation can be used to provide the velocity of a fluid percolating through a moving matrix.

One has to keep in mind that this equation is only applicable in the case of a laminar flow, which means slow, viscous flow. The Reynolds number, Re , is suitable to see whether the law can be used:

$$Re = \frac{\rho_f v d}{\mu}. \quad (2.2)$$

Here, ρ_f is the fluid density, v is the flow speed and d is a characteristic grain diameter of the porous media. Low Re characterizes laminar flow, while high Re leads to turbulent flow. Tests have shown that cases with $Re < 10$ can be well described by a Darcy flow, even though the transition from laminar to turbulent flow takes place at

$Re \approx 2200$ (Turcotte and Schubert, 2014). In regions inside Earth, typical values for the viscosity of melt are of the order of 1 Pas, densities lie around 2800 kg/m^3 , grain sizes are in the order of 10^{-3} m and typical flow velocities are approximately 1 m/yr (from McKenzie, 1984). Even though these parameters can have very big variations they give $Re \approx 10^{-7}$ and are therefore way below the boundary of 10. So it should be save to use the Darcy equation in most scenarios concerning the movement of melt inside Earth.

The driving-force in the Darcy Law is the pressure difference due to gravity and for a static fluid the pressure can be written as $P = \rho_f g h$, where h is the height of the fluid. Therefore, an important parameter in the Darcy equation is the density of the fluid ρ_f , which depends on various conditions. Silicate melt densities usually vary between 2800 kg/m^3 for basaltic melts and 2200 kg/m^3 for rhyolitic melts (Best, 2003). Other than the composition of the melt, parameters like temperature, pressure and volatile content influence the density. When the density of a melt is measured at a certain T and P (e.g. Stolper and Walker, 1980) it can be corrected for different T and P using the thermal expansion and the compressibility (Sigurdsson et al., 2015). The density difference between the fluid and its surrounding solid is what drives the motion of melt through a porous matrix and in most cases the melt density is smaller than the matrix density, resulting in a melt percolating upwards. However, there are cases in which the density difference becomes very small or even changes its sign. This might be the case for melt rising from very deep regions (see Schmeling and Arndt, 2017).

A full set of equations that describe the percolation of a fluid through a moving viscous matrix can be taken from McKenzie (1984) (see also Bercovici et al., 2001; Schmeling, 2000) where the movement of the fluid is based on the Darcy law. More insights on these equations is given in section 3.

2.2 Diapirism and Solitary Porosity Waves

Diapirism and solitary porosity waves, both are possible end members for the transport of melt. While diapirism is not solely connected to melt, solitary porosity waves can only be observed when melt is able to move relatively to a compacting media. In this section a small introduction is given into these two mechanisms.

Diapirism Diapirism is described by Turcotte and Schubert (2014) as the upwelling of a rock due to its lower density or buoyancy into a high density overlying brittle rock. Etymologically, the word comes from the Greek "diaperein" meaning "to pierce through". In general, the term diapirism is usually used for any kind of upwelling that takes place inside Earth and can be of various scales in size.

Relatively small diapirism can be observed at salt deposits (Schultz-Ela et al., 1993; Daudr and Cloetingh, 1994), where the light salt is upwelling through the sedimentary rocks that have been deposited above it (see Fig. 2.3). A nice example for a Rayleigh-Taylor instability, which is a gravitational instability of a high density layer lying on top of a low density layer. A direct result of this instability is diapirism. In reality the building of salt domes is probably not solely the result of diapirism but more a combination of sedimentation on top of the salt and simultaneous upwelling of the

salt, which is called down-building (e.g. Fuchs et al., 2011).

Large scale diapirism takes place in the mantle starting from the core-mantle boundary,

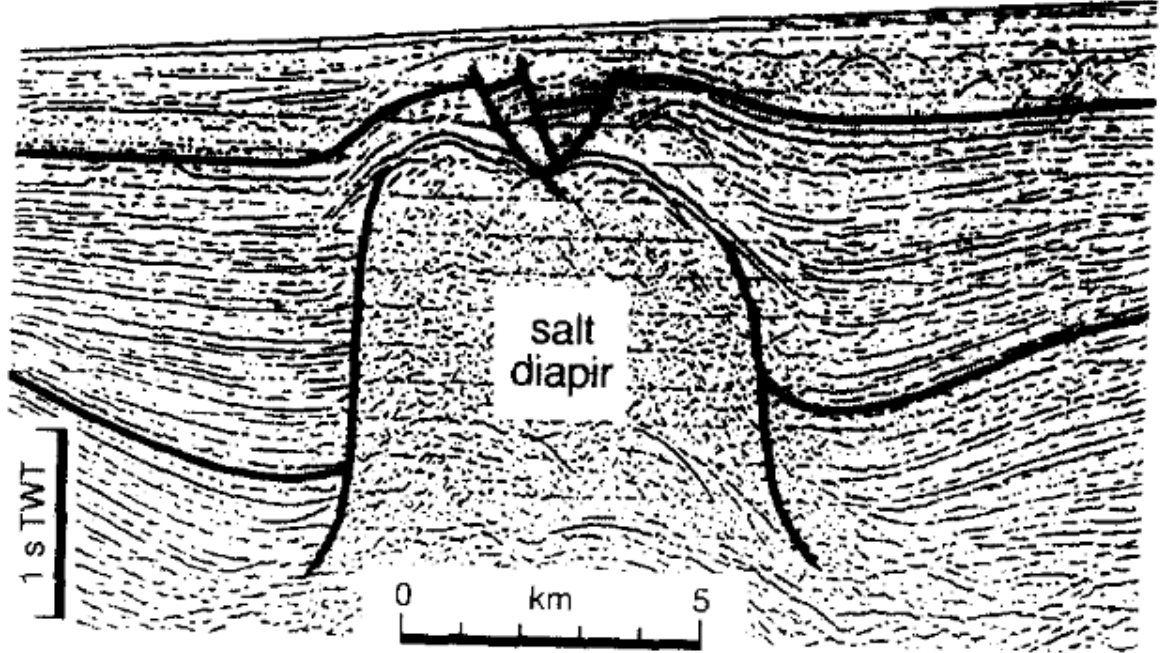


Figure 2.3: Seismic section of a salt diapir in Angola from Schultz-Ela et al. (1993).

or the D''-layer, up to the upper mantle, reaching the lithosphere. This diapirism is called a mantle plume and was proposed by Wilson (1963) and later further developed by Morgan (1971, 1972). These plumes are characterized by a thin tail and a bulky head in which internal convecting leads to mushroom like shapes (see Fig. 6.3).

While diapirs are not restricted in some way in size, however, there are characteristic or dominant wavelengths. In an isoviscous two-layer system with a layer thickness b and the densities ρ_1 and ρ_2 , where ρ_1 belongs to the upper layer and $\rho_1 > \rho_2$, the characteristic wavelength λ , following Turcotte and Schubert (2014), is equal to

$$\lambda = 2.568 b, \quad (2.3)$$

depending only on the thickness of the layer, whereby the prefactor depends also on boundary conditions among other things. However, the growth time is equal to

$$\tau = \frac{13.04 \eta}{(\rho_1 - \rho_2)gb}. \quad (2.4)$$

This states that the diapir needs a longer amount of time to build with higher viscosity and smaller density differences.

With different viscosities in the upper and lower layer the wave length of an initial diapir is

$$\lambda \sim b \left(\frac{\eta_1}{\eta_2} \right)^{1/3} \quad (2.5)$$

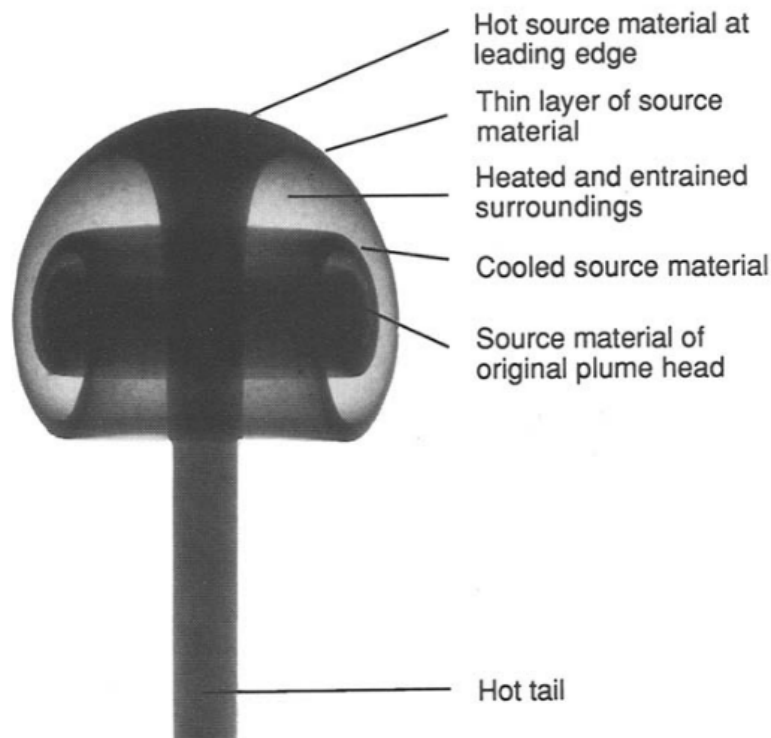


Figure 2.4: A photograph of a laboratory plume from Campbell and Griffiths (1990); Key features are labeled.

and, therefore, is directly depending on the viscosity contrast (Schubert et al., 2001), additionally to the initial layer thickness.

Another important factor for the dimension of diapirs are initial conditions or perturbations. It can be shown that the dominant and the characteristic wavelength of an instability are not always equal but may differ immensely in special cases shown by Schmeling (1987). For initial sinusoidal perturbations, high amplitudes may lead to final wavelengths equal to the initial perturbation and not the characteristic wavelength.

Solitary porosity waves In 1834 John Scot Russell, a Scottish civil engineer and naval architect, carried out tests to find the best design for canal ships. During these experiments he observed the occurrence of waves that traveled in front of the boats, drawn by horses, and proceeded to travel once the boat stopped. He could follow the wave keeping its shape and velocity for up to 2 – 3 km, until it eventually dispersed. He called this kind of wave *wave of translation*, but today is known by the name *solitary wave*.

Solitary waves are a special case of *solitons*, which in turn are self-reinforcing waves keeping their shape and velocity during movement. Drazin and Johnson (1989) gives a relatively easy definition of solitons with the following three points:

1. They are of permanent form.

2. They are localized within region.
3. They can interact with other solitons, and emerge from the collision unchanged, except for a phase shift.

While a soliton fulfills all of these criteria, a solitary wave fulfills only the first two, as it will change during the interaction with other solitary waves.

In geodynamics this type of waves is observed at partially molten regions inside Earth where pore-space distributions ascend. They are called *solitary porosity waves* or *Magmons*, based on Solitons, although this term is outdated because these waves are not solitons, as it was originally thought.

Porosity waves are features of two-phase flow and shortly after McKenzie (1984) published his description of two-phase flow Scott and Stevenson (1984) could show that they are a possible solution for this mathematical description. Thereby, the shape of a solitary wave is preserved by the cancellation of decompaction in front and the compaction behind the wave. Due to the buoyancy of the fluid the pore-space wants to diverge and the accompanied underpressure attracts the surrounding fluid, leading to the apparent movement of melt with the ascending wave. What is actually traveling in wave form is not the fluid but the pore-space, which is filled with the fluid melt. Scott and Stevenson (1984) thought that these waves fulfill the criteria for a Soliton, but it later could be shown by Barcion and Richter (1986) that they do not. The shape is not conserved perfectly and in higher dimension models this will become more obvious. Scott and Stevenson (1986) showed that a fast wave overtaking a small one will totally disturb the smaller one, but it still keeps its identity. The bigger one stays mostly undisturbed.

Interestingly, 1-D waves in a higher dimensional model, meaning an infinitely extended layer of melt, is not stable and will inevitably decay into several higher dimension waves. In Fig. 2.5 this property is shown by a model of Scott and Stevenson (1986). The same is valid for 3-D waves (Wiggins and Spiegelman, 1995), where the waves are spherical objects of high porosity, decreasing with distance to the center. Until to this

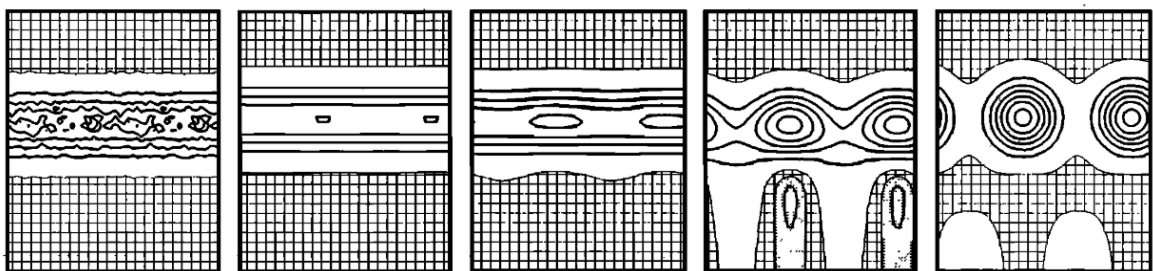


Figure 2.5: Decay of a 1-D solitary wave into several 2-D waves, modeled by Scott and Stevenson (1986). Plots show the contour lines for five different steps of the melt fraction. Out of the noised up 1-D wave two 2-D waves emerged.

point solitary waves were only modeled under the assumption that the solid matrix is not able to circulate, i.e. the divergence free part of the velocity is zero. Scott (1988) could show, that without this assumption solitary waves are still able to build

up and furthermore, that this has interesting consequences for the matrix. While for some cases the upward flow of the fluid is preserved by an equally large downward flow of solid matrix, it was shown that for some cases, namely small ratios of shear to compaction viscosity, this circulation becomes dominant, leading to an upward flowing matrix in the center of the wave, which is preserved by a large scale downward flow at the flanks of the wave. This corresponds to an increasing influence of diapirism.

In recent years it was established that for surface near regions plastic yielding around pores may lead to decompaction weakening (Yarushina and Podladchikov, 2015). This is of importance for solitary waves as fluid overpressure in front of the wave results in effective weakening and pores open faster. As a result, waves are no longer perfectly spherical but elongated on the back side, the compacting part of the wave (e.g. Yarushina et al., 2015; Omlin et al., 2018). Fig. 2.6 shows a solution from Omlin et al. (2018) of a swarm of these elongated waves that emerged naturally from an initially lens like porosity perturbation.

A lot of additional work was carried out on solitary waves (e.g. Yarushina et al., 2020;

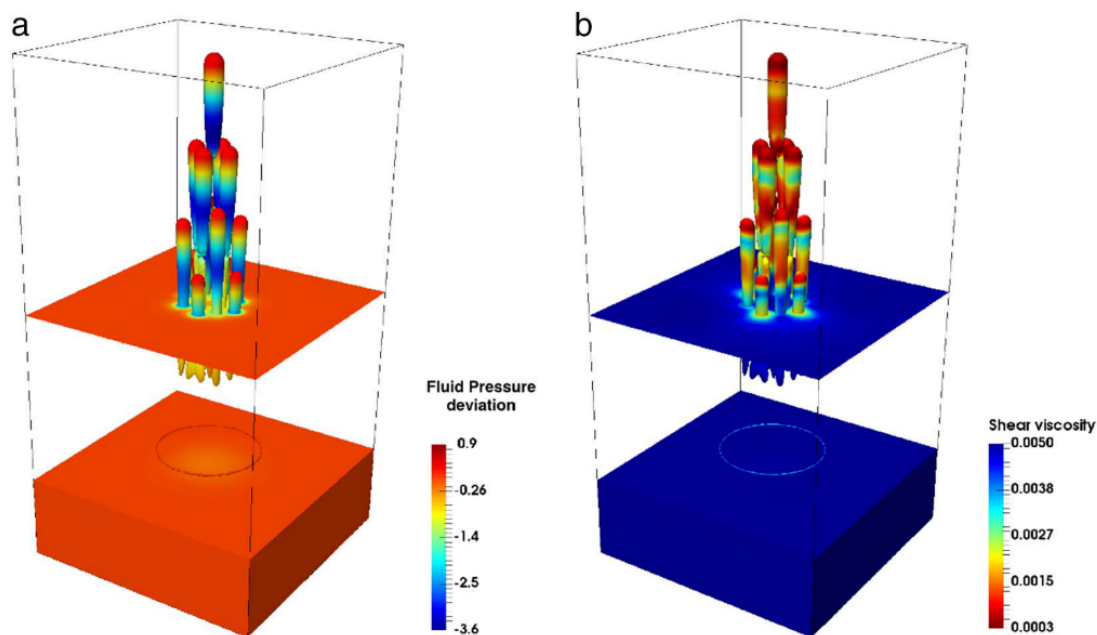


Figure 2.6: A swarm of elongated solitary waves, due to decompaction weakening, emerging from an initially lens like perturbation from Omlin et al. (2018)

Connolly and Podladchikov, 2007; Simpson and Spiegelman, 2011; Richard et al., 2012) and even though they all used different assumptions, model setups or boundary conditions, the size of a solitary wave is always of the order of 3–5 times the compaction length, which is a typical length scale over which compaction takes place. Different to diapirs these solitary waves cannot be found in all scales but are always restricted to the compaction length. It depends on the solid matrix; inside Earth it is usually in the order of 100–10000 m and, therefore, solitary waves will be always in this scale. Since the discovery of porosity waves, being the solution of two-phase flow, it was

thought that they are not able to transport mass, that material gets sucked into the center of the wave but then is ejected after passing. Just recently Jordan et al. (2018) could show that porosity waves are in fact able to transport material. In special cases a recirculating area in the center of the wave builds up during emergence of the wave. The material in this area is completely separated from its surroundings by a circular dividing streamline. Whether a solitary wave is able to transport material or not depends on the non-dimensional wave velocity. After Jordan et al. (2018), slow waves with velocities smaller than 3 times the background fluid velocity are not able to transport mass, while faster ones are capable.

2.3 Trace Elements and their Behavior during Melting

A trace element is mostly defined as a chemical element that makes less than 0.1 wt% or 1000 ppm of a rock. These trace elements usually substitute major elements in a minerals lattice with similar sizes and equal charge.

In some cases there is no possible gap in a mineral and the element will leave as soon as there is an option to do so. If so, they are called incompatible and prefer to go into melt when melting occurs. Elements preferring to stay in the lattice are called compatible. This behavior is strongly depending on melt compositions. For example P is incompatible in mantle mineralogy but becomes compatible in granites where it can be accommodated in apatite (Rollinson, 1993).

Trace elements can be divided into groups based on their position in the periodic table of the chemical elements. Rare-earth elements (REE) are of interest for electronics and consist of the elements with atomic numbers 57–71. Another group, the platinum group elements (PGE) have the atomic numbers 44–46 and 76–79. The elements in these groups usually have similar geochemical properties and therefore it is helpful to look at these groups as a whole. However, in special cases geological processes lead to different behavior within them.

As the radius and charge of an element have major influences on whether they can be accommodated into a lattice it may be helpful to plot ion radius and charge into a diagram (Fig. 2.7). Based on this, trace elements can be divided into small highly charged cations, called high field strength elements (HFS), and large low charged cations, called low field strength elements (LFS) or, more often, large ion lithophile elements (LIL). Small, relatively low charge cations are usually more compatible, like most major elements in rocks are.

The distribution of trace elements between phases can be given by so called distribution coefficients (McIntire, 1963) and the most used is the so called Nernst distribution coefficient, K_d . It is defined as

$$K_d = \frac{c_{\text{element}}^{\text{mineral}}}{c_{\text{element}}^{\text{melt}}}, \quad (2.6)$$

where c is the equilibrium concentration distribution of a trace element in a mineral and a melt. If $K_d = 1$ then the element is equally distributed. For $K_d > 1$ the element is compatible in the mineral and prefers to stay there during a melting event. $K_d < 1$

refers to an incompatible element.

While the Nernst distribution coefficient is given for single minerals, for rocks the bulk partition coefficient D can be calculated using K_d :

$$D_i = x_1 K_{d,1}^i + x_2 K_{d,2}^i + x_3 K_{d,3}^i + \dots = \sum_{j=1}^N x_j K_{d,j}^i. \quad (2.7)$$

D_i is the partition coefficient for element i in a rock, calculated based on the Nernst partition coefficient $K_{d,j}^i$ of each mineral j in the rock. x_j is the percentage proportion of the mineral j .

K_d can either be measured in natural systems or in synthetic materials in experiments in laboratories. In natural systems, minerals and their glassy matrix from a rapidly cooled volcanic rock can be measured giving the trace element concentrations in both parts (Schnetzler and Philpotts, 1970). These measurements are usually quite reliable, but to get partition coefficients for certain pressures and temperatures, synthetic material can be enriched with an element of interest, which then can be melted providing exact concentrations (Irving, 1978). Henry's law can be used to give partition coefficients for other temperature and pressure conditions. The law states that at equilibrium the activity of a trace element is directly proportional to its composition. If mixing is ideal, which is often the case for trace elements in a host mineral, the trace element activity is equal to its concentration, following Raoult's law (Rollinson, 1993).

Several parameters influence the partition coefficients and by far the biggest influence has the composition of the melt. Partition coefficients in studies are usually given for a certain melt composition. For example, while K_d of REEs in a hornblende lies around the order of 1 for basaltic melt, they are of the order of 10 for rhyolitic melt (Rollinson, 1993).

The effect of temperature and pressure is also important but is hard to unravel because solidus temperature strongly depends on pressure as well. In general it can be shown that partition coefficients decrease with increasing temperature, while they increase with increasing pressure. That has the consequence that both effects cancel out each other to some extent (Green and Pearson, 1983; Irving, 1978).

The oxygen activity is only important for Eu. While this element's partition coefficient can be affected by one order of magnitude, other REEs are not affected at all (Drake and Weill, 1975).

The water content in the melt has only minor influence on the partition coefficients, even for high water contents of up to 10 wt%, and usually can be neglected (Green and Pearson, 1986).

The correct choice of partition coefficients is very important for modeling partial melting of rocks, which usually is carried out on two end-members of melting: batch and fractional melting.

Batch melting corresponds to equilibrium melting and describes the process of melting during which the solid and melt are constantly reacting to keep the system in equilibrium until the melt gets extracted as a *batch* in once.

Fractional melting, or Rayleigh melting, describes the process of melting during which each produced *fraction* of melt is instantly isolated from its source. Therefore, only

each fraction is in equilibrium with the source at that time, but the whole bunch of melt is not in equilibrium with the source rock.

The evolving trace element concentrations as a function of melt degree of both end members can be described mathematically by simple equations (Rollinson, 1993). The fluid concentration c_f in the case of batch melting is given by

$$\frac{c_f}{c_0} = \frac{1}{D + F(1 - D)}, \quad (2.8)$$

where c_0 is the concentration of the source material and F is the degree of melting. As solid and fluid are in equilibrium, the concentration of the solid can be given as

$$\frac{c_s}{c_0} = D \cdot c_f = \frac{D}{D + F(1 - D)}. \quad (2.9)$$

It should be noted that the bulk partition coefficient in these equations is from the source material before the melt was produced. Composition of residue and melt change during the process of melting and more complex equations can be used to catch these effects, but for relatively small degrees of melting the upper equations are valid.

In the case of fractional melting there are two equations for the fluid concentration: One for the concentration of a melt increment produced at a certain melt degree, and one for the accumulation of all these melt increments. The concentration of a melt increment is given by

$$\frac{c_f}{c_0} = \frac{1}{D}(1 - F)^{(1/D)-1} \quad (2.10)$$

and the remaining solid is in equilibrium to this melt increment, resulting in

$$\frac{c_s}{c_0} = D \cdot c_f = (1 - F)^{(1/D)-1}. \quad (2.11)$$

The concentration of the accumulated melt \bar{c}_f is given by

$$\frac{\bar{c}_f}{c_0} = \frac{1}{F} \left[1 - (1 - F)^{1/D} \right]. \quad (2.12)$$

Again, these equations are valid for modal melting and can be extended for the case of non-modal melting.

Which model is applicable for a certain case depends on the ability of a melt to separate from its source. Fractional melting might be applicable for basaltic melts where small fractions of melts can be rapidly extracted to the surface, while batch melting should be applicable to higher viscous, felsic melts.

Similar to the processes described before during melting, processes appear during freezing or crystallization.

During equilibrium crystallization all phases are in equilibrium, which is not very likable but might be applicable to some special cases. The fluid concentration can be calculated using the same equation as for equilibrium melting (Eq. (2.8)), but F now is the remaining melt fraction and c_0 is the trace element concentration of the initial melt.

Usually, it is assumed that crystals are removed from the melt after crystallization and they are not in equilibrium with the remaining melt. Therefore, most scenarios can be described by Rayleigh fractionation or fractional crystallization. Here the fluid concentration is given by

$$\frac{c_f}{c_0} = F^{D-1} \quad (2.13)$$

and the concentration of an incremental crystal produced can be achieved by

$$\frac{c_s}{c_0} = DF^{D-1}. \quad (2.14)$$

Again, the mean concentration of the accumulated crystals can be given by another equation:

$$\frac{\bar{c}_s}{c_0} = \frac{1 - F^D}{1 - F}. \quad (2.15)$$

As both these end-members are not that strongly applicable to crystallization taking place in nature, Langmuir (1989) derived equations for *in situ* crystallization, where crystallization takes place in a magma chamber and solidified crystals form solidification zones at the chambers walls and crystals do not just settle due to gravity at the chambers bottom. Several further effects like zone refining and contamination can be added to the equations.

In Fig. 2.8 the equilibrium and non-equilibrium cases of melting and crystallization are shown. In general it can be seen that the fractional, non-equilibrium cases tend to stronger depletion of the source material and change the concentrations over many orders of magnitudes, while the equilibrium cases give concentration variations in the order of the partition coefficient.

It might be counter-intuitive that more melting leads to smaller incompatible (i.e. $D < 1$) trace element concentrations, but it becomes clear when the process is looked at step-wise for example for fractional melting. The first melt increment produced has a concentration that is in equilibrium to the solid giving $c_f = c_s/D$. The solid becomes depleted in this element and the concentration decreases. The next melt increment again is in equilibrium but now to the already depleted source material. This leads to slightly lower concentrations for the fluid. The same applies to the equilibrium case but the concentrations do not decrease as strongly. If all the material is molten ($F = 1$) the fluid has the same concentration as the original source material, in the equilibrium case, as well as in the accumulated melt in the fractional melting case, which also explains why the concentrations have to decrease.

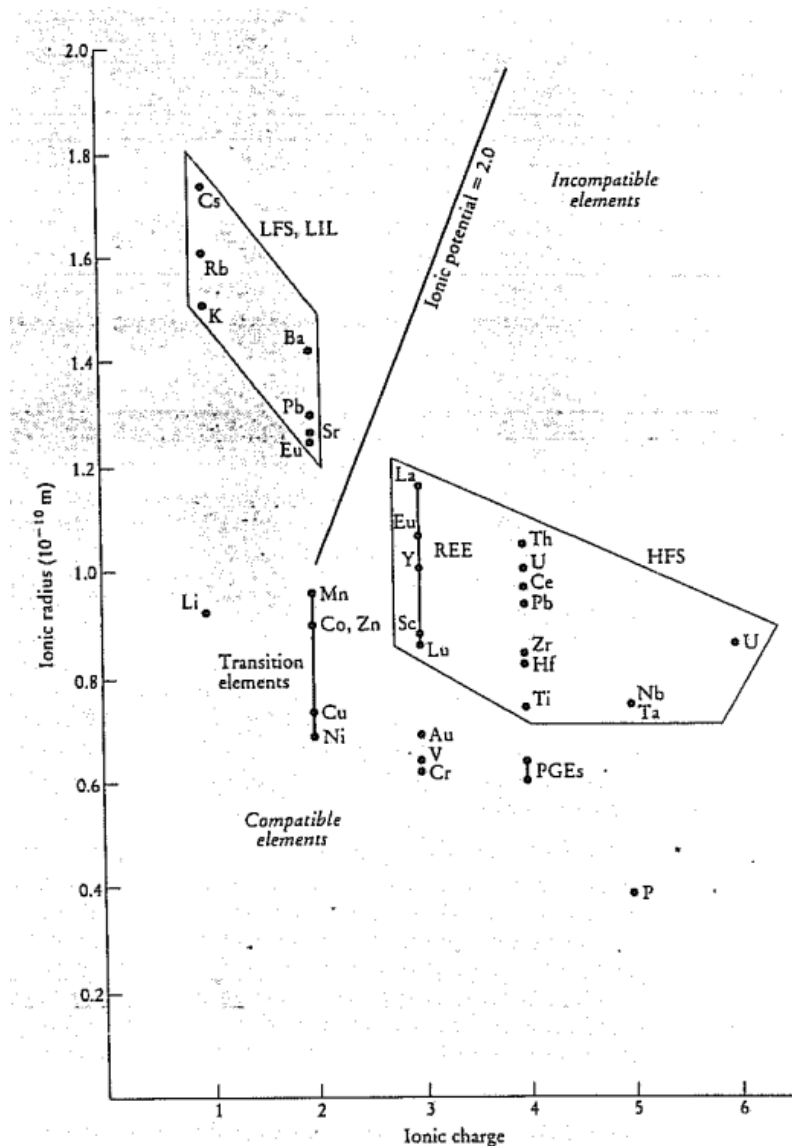


Figure 2.7: Ionic radius versus ionic charge for some important trace elements. The ion charge of 2 divides elements into high field strength elements (HFS) and low field strength elements (LFS), also called large ion lithophile elements (LIL). Picture is taken from Rollinson (1993).

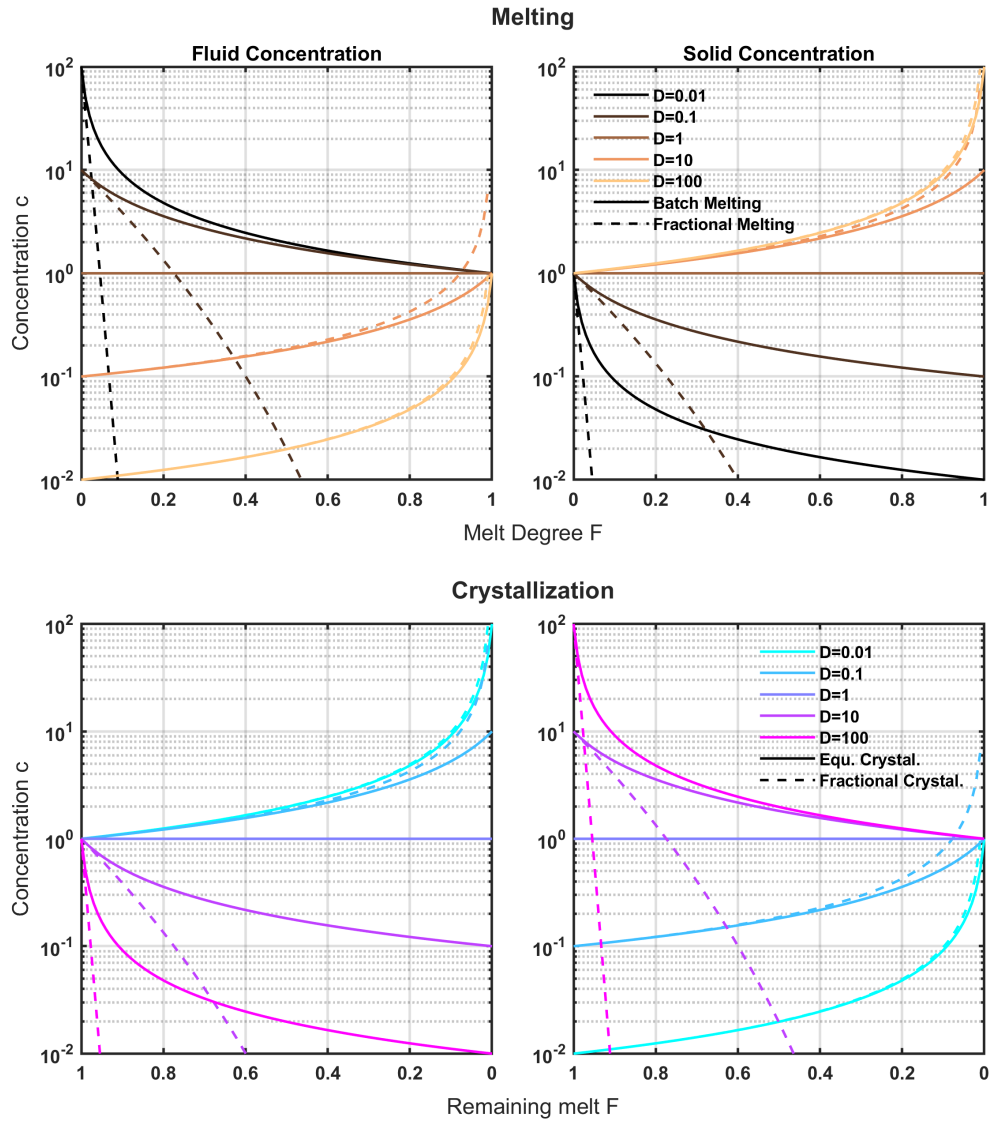


Figure 2.8: Trace Element concentrations of fluid (left) and solid (right) during melting (top) and crystallization (bottom). In the case of melting, batch (solid lines) and fractional melting (dashed lines) cases are shown as a function of melt degree for different bulk partition coefficients D . Crystallization is divided into equilibrium (solid lines) and fractional (dashed lines) crystallization and is shown for various D as well, but now as a function of remaining melt. Please note that F decreases from left to right.

References

- Alt, J. C., Laverne, C., Vanko, D. A., Tartarotti, P., Teagle, D. A. H., Bach, W., Zuleger, E., Erzinger, J., Honnorez, J., Pezard, P. A., Becker, K., Salisbury, M. H., and Wilkens, R. H. (1996). 34. Hydrothermal alteration of a section of upper oceanic crust in the eastern equatorial pacific: a synthesis of results from site 504 (DSDP Legs 69, 70, and 83, and ODP Legs 111, 137, 140, and 148). *Proceedings of the Ocean Drilling Program*, 148.
- Armitage, P. J. (2011). Dynamics of protoplanetary disks. *Annual Review of Astronomy and Astrophysics*, 49:195–236.
- Barcilon, V. and Lovera, O. M. (1989). Solitary waves in magma dynamics. *Journal of Fluid Mechanics*, 204(1989):121–133.
- Barcilon, V. and Richter, F. M. (1986). Nonlinear waves in compacting media. *Journal of Fluid Mechanics*, 164(1986):429–448.
- Bercovici, D., Ricard, Y., and Schubert, G. (2001). A two-phase model for compaction and damage: 1. General Theory. *Journal of Geophysical Research*, 106(B5):8887.
- Best, M. G. (2003). *Igneous and metamorphic petrology*. Blackwell Science Ltd, New Jersey, 2 edition.
- Bittner, D. and Schmeling, H. (1995). Numerical Modelling of Melting Processes and Induced Diapirism In the Lower Crust. *Geophysical Journal International*, 123(1):59–70.
- Bowen, N. L. (1922). The reaction principle in petrogenesis. *The Journal of Geology*, 30.
- Campbell, I. H. and Griffiths, R. W. (1990). Implications of mantle plume structure for the evolution of flood basalts. *Earth and Planetary Science Letters*, 99:79–93.
- Connolly, J. A. and Podladchikov, Y. Y. (2007). Decompaction weakening and channeling instability in ductile porous media: Implications for asthenospheric melt segregation. *Journal of Geophysical Research: Solid Earth*, 112(10):1–15.
- Daudr, B. I. and Cloetingh, S. (1994). Numerical modelling of salt diapirism : influence of the tectonic regime. *Tectonophysics*, 240:59–79.
- Drake, M. J. and Weill, D. F. (1975). Partition of Sr, Ba, Ca, Y, Eu²⁺, Eu³⁺, and other REE between plagioclase feldspar and magmatic liquid: an experimental study. *Geochimica et Cosmochimica Acta*, 39(5):689–712.
- Drazin, P. G. and Johnson, R. S. (1989). *Solitons: An Introduction*. Cambridge University Press.
- Fuchs, L., Schmeling, H., and Koyi, H. (2011). Numerical models of salt diapir formation by down-building: the role of sedimentation rate, viscosity contrast, initial amplitude and wavelength. *Geophysical Journal International*, 186:390–400.

- Green, T. H. and Pearson, N. J. (1983). Effect of pressure on rare earth element partition coefficients in common magmas. *Nature*, 305(5933):414–416.
- Green, T. H. and Pearson, N. J. (1986). Rare-earth element partitioning between sphene and coexisting silicate liquid at high pressure and temperature. *Chemical Geology*, 55(1-2):105–119.
- Irving, A. J. (1978). A review of experimental studies of crystal/liquid trace element partitioning. *Geochimica et Cosmochimica Acta*, 42(6):743–770.
- Jaupart, C., Labrosse, S., Lucazeau, F., and Mareschal, J. C. (2015). *Temperatures, Heat, and Energy in the Mantle of the Earth*, volume 7. Elsevier B.V.
- Jordan, J. S., Hesse, M. A., and Rudge, J. F. (2018). On mass transport in porosity waves. *Earth and Planetary Science Letters*, 485:65–78.
- Katz, R. F., Spiegelman, M., and Langmuir, C. H. (2003). A new parameterization of hydrous mantle melting. *Geochemistry, Geophysics, Geosystems*, 4(9):1–19.
- Koch, T. E., Spahr, D., Tkalcec, B. J., Lindner, M., Merges, D., Wilde, F., Winkler, B., and Brenker, F. E. (2021). Formation of chondrule analogs aboard the International Space Station. *Meteoritics and Planetary Science*, 56(9):1669–1684.
- Langmuir, C. H. (1989). Geochemical consequences of in situ differentiation. *Nature*, 340(July):199–205.
- Lay, T., Hernlund, J., and Buffett, B. A. (2008). Core – mantle boundary heat flow. *Nature Geoscience*, 1:25–32.
- McIntire, W. L. (1963). Trace element partition coefficients—a review of theory and applications to geology. *Geochimica et Cosmochimica Acta*, 27(12):1209–1264.
- McKenzie, D. (1984). The generation and compaction of partially molten rock. *Journal of Petrology*, 25(3):713–765.
- Morgan, W. J. (1971). Convection plumes in the lower mantle. *Nature*, 230(5288):42–43.
- Morgan, W. J. (1972). Deep Mantle Convection Plumes and Plate Motions. *The American Association of Petroleum Geologists Bulletin*, 56:203–213.
- Omlin, S., Räss, L., and Podladchikov, Y. Y. (2018). Simulation of three-dimensional viscoelastic deformation coupled to porous fluid flow. *Tectonophysics*, 746(August 2017):695–701.
- Pollack, H. N., Hurter, S. J., and Johnson, J. R. (1993). Heat flow from the Earth’s interior: Analysis of the global data set. *Reviews of Geophysics*, 31(3):267–280.
- Richard, G. C., Kanjilal, S., and Schmeling, H. (2012). Solitary-waves in geophysical two-phase viscous media: A semi-analytical solution. *Physics of the Earth and Planetary Interiors*, 198-199:61–66.

- Rollinson, H. R. (1993). *Using Geochemical Data: Evaluation, Presentation, Interpretation*. Pearson Education Limited, Essex, 1st edition.
- Schmeling, H. (1987). On the relation between initial conditions and late stages of Rayleigh-Taylor instabilities. *Tectonophysics*, 133:65–80.
- Schmeling, H. (2000). *Partial melting and melt segregation in a convecting mantle*. Springer.
- Schmeling, H. and Arndt, N. (2017). Modelling komatiitic melt accumulation and segregation in the transition zone. *Earth and Planetary Science Letters*, 472:95–106.
- Schmeling, H., Kruse, J. P., and Richard, G. C. (2012). Effective shear and bulk viscosity of partially molten rock based on elastic moduli theory of a fluid filled poroelastic medium. *Geophysical Journal International*, 190(3):1571–1578.
- Schnetzler, C. C. and Philpotts, J. A. (1970). Partition coefficients of rare-earth elements between igneous matrix material and rock-forming mineral phenocrysts-II. *Geochimica et Cosmochimica Acta*, 34(3):331–340.
- Schubert, G., Turcotte, D. L., and Olson, P. (2001). *Mantle Convection in the Earth and Planets*. Cambridge University Press.
- Schultz-Ela, D. D., Jackson, M. P. A., and Vendeville, B. C. (1993). Mechanics of Active Diapirism Mechanics of active salt diapirism. *Tectonophysics*, 228:275–312.
- Scott, D. R. (1988). The competition between percolation and circulation in a deformable porous medium. *Journal of Geophysical Research*, 93(B6):6451–6462.
- Scott, D. R. and Stevenson, D. J. (1984). Magma solitons. *Geophysical Research Letters*, 11(11):1161–1164.
- Scott, D. R. and Stevenson, D. J. (1986). Magma ascent by porous flow. *Journal of Geophysical Research B*, 91(B9):9283.
- Sigurdsson, H., Houghton, B., McNutt, S., Rymer, H., and Stix, J. (2015). *The encyclopedia of volcanoes*. Elsevier, Oxford, 2 edition.
- Simpson, G. and Spiegelman, M. (2011). Solitary wave benchmarks in magma dynamics. *Journal of Scientific Computing*, 49(3):268–290.
- Sleep, N. H. (1990). Hotspots and Mantle Plumes: Some Phenomenology. *Geology*, 95:6715–6736.
- Stacey, F. D. and Loper, D. E. (1983). The thermal boundary-layer interpretation of D” and its role as a plume source. *Physics of the Earth and Planetary Interiors*, 33(1):45–55.
- Stolper, E. and Walker, D. (1980). Melt Density and the Average Composition of Basalt. *Contributions to Mineralogy and Petrology*, 74:7–12.

- Takahashi, E. (1986). Melting of a dry peridotite KLB-1 up to 14 GPa: Implications on the Origin of peridotitic upper mantle. *Journal of Geophysical Research*, 91(B9):9367.
- Turcotte, D. L. and Schubert, G. (2014). *Geodynamics*. Cambridge University Press, 3. edition.
- White, W. M. (2018). *Encyclopedia of Geochemistry*. Springer Nature, Cham, Switzerland.
- Wiggins, C. and Spiegelman, M. (1995). Magma migration and magmatic solitary waves in 3D. *Geophysical Research Letters*, 22(10):1289–1292.
- Wilson, T. (1963). Hypothesis of earth’s behaviour. *Nature*, 198(4884):925–929.
- Wood, B. J., Walter, M. J., and Wade, J. (2006). Accretion of the Earth and segregation of its core. *Nature*, 441(7095):825–833.
- Yarushina, V. M. and Podladchikov, Y. Y. (2015). (De)compaction of porous viscoelastoplastic media: Model formulation. *Journal of Geophysical Research: Solid Earth*, pages 3782–3803.
- Yarushina, V. M., Podladchikov, Y. Y., and Connolly, J. A. (2015). (De)compaction of porous viscoelastoplastic media: Solitary porosity waves. *Journal of Geophysical Research : Solid Earth*, pages 1–20.
- Yarushina, V. M., Podladchikov, Y. Y., and Wang, H. (2020). Model for (de)compaction and porosity waves in porous rocks under shear stresses. *Journal of Geophysical Research: Solid Earth*, 125:1–30.

Chapter 3

Methods

This chapter gives an introduction into the equations describing two-phase flow and the transport of trace elements or isotopes within melt. Further, it is shown how the equations from the publications can be derived from the general formulation. To avoid repetitions during the reading of this thesis, the governing equations sections of the publications may be skipped. The comparison of segregation to Stokes velocity in publication 2 is not treated here.

3.1 General Equations of Two-Phase Flow

Two-phase flow usually means the movement of two viscous phases relative to each other. In our case these two phases are usually a deformable solid rock and its fluid melt, which separates from its residual solid rock by percolation or segregation through pores. The differential equations describing this physical process are shown in several publications (e.g. McKenzie, 1984; Schmeling, 2000; Bercovici et al., 2001).

Our formulation consists of equations conserving the mass and the momentum, both separately for the solid and the fluid, and one equation conserving the energy for the solid-liquid mixture. This is suitable as we assume equilibrium temperature between solid and fluid. All variables associated with the fluid have the subscript f and the variables associated with the solid the subscript s . The conservation of the mass of the fluid is given by

$$\frac{\partial \rho_f \varphi}{\partial t} + \vec{\nabla} \cdot (\rho_f \varphi \vec{v}_f) = \Gamma \quad (3.1)$$

and the conservation of the solid is

$$\frac{\partial \rho_s (1 - \varphi)}{\partial t} + \vec{\nabla} \cdot [\rho_s (1 - \varphi) \vec{v}_s] = -\Gamma. \quad (3.2)$$

φ is the melt fraction. ρ_s and ρ_f are the densities of the solid and the fluid, and may be variable, depending on temperature or composition. \vec{v}_s and \vec{v}_f are the velocities of solid and fluid. φ is the melt fraction. Γ is the melt generation rate, which couples these equations. It describes the amount of mass that is either melted ($\Gamma > 0$) or frozen ($\Gamma < 0$) per time. The equations show that the change of mass with time (1st term) is equal to the change due to advection (2nd term) and the exchange of mass

between solid and fluid (3rd term). It is often assumed that the densities in these equations (but not in the buoyancy term in the later equations) are constant and the same, which is known as the Compaction Boussinesq Approximation (see Schmeling, 2000). For this approximation the densities can be eliminated from the derivatives and adding up Eq. (3.1) and Eq. (3.2) leads to

$$\vec{\nabla} \cdot \vec{v} = 0. \quad (3.3)$$

\vec{v} is the mixture velocity equal to $\varphi \vec{v}_f + (1 - \varphi) \vec{v}_s$. The divergence of the solid velocity is not zero:

$$\vec{\nabla} \cdot \vec{v}_s = -\vec{\nabla} \cdot [\varphi (\vec{v}_f - \vec{v}_s)]. \quad (3.4)$$

This states that the divergence of the solid is equal to minus the divergence of the Darcy velocity with $\vec{v}_f - \vec{v}_s$ being the segregation velocity.

The momentum conservation of the fluid is achieved by using a generalized form of the Darcy equation

$$\vec{v}_f - \vec{v}_s = -\frac{k_\varphi}{\mu \varphi} \left(\vec{\nabla} P_f - \rho_f \vec{g} \right) \quad (3.5)$$

where μ is the fluid viscosity and P_f is the fluid pressure. k_φ can have various forms but for comparatively small melt fractions it is often suitable to use the Kozeny-Carman relation (e.g. Costa, 2006)

$$k_\varphi = k_0 \varphi^n. \quad (3.6)$$

k_0 and n are parameters depending on the geometry of the pores and grain size. n is usually chosen between 2 and 3. In the case of not moving solid ($v_s = 0$) Eq. (3.5) becomes the Darcy law

$$\vec{v}_f \varphi = -\frac{k_\varphi}{\mu} \left(\vec{\nabla} P_f - \rho_f \vec{g} \right), \quad (3.7)$$

where the parentheses is the hydraulic pressure, which is also called *hydraulic head* or *piezometric pressure*.

The conservation of momentum in the mixture requires a more complicated definition for the stresses

$$\bar{\rho} \vec{g} - \vec{\nabla} P_f + \vec{\nabla} \cdot \boldsymbol{\tau} = 0. \quad (3.8)$$

$\bar{\rho}$ is the density of the solid-melt mixture given by $\bar{\rho} = (1 - \varphi) \rho_s + \varphi \rho_f$. $\boldsymbol{\tau}$ is the effective viscous stress tensor of the matrix

$$\boldsymbol{\tau} = \eta \left(\frac{\partial v_{si}}{\partial x_j} + \frac{\partial v_{sj}}{\partial x_i} \right) + \left(\zeta - \frac{2}{3} \eta \right) \delta_{ij} \nabla \cdot \vec{v}_s. \quad (3.9)$$

η and ζ are the shear and volume viscosities, respectively. Eq. (3.9) includes the shear (1st term on the right) and the compaction components (2nd term on the right) of the matrix. In this equation it is assumed that the fluid viscosity is much smaller than the matrix viscosity. Therefore the stresses within the fluid can be neglected and only the solid velocities and viscosities appear.

It is notable that in both, Eq. (3.5) and Eq. (3.8) P_f is the pressure in the fluid and they can be merged to eliminate the pressure leading to

$$\vec{v}_f - \vec{v}_s = -\frac{k_0 \varphi^{n-1}}{\mu} \left[(\rho_s - \rho_f) \vec{g} (1 - \varphi) + \vec{\nabla} \cdot \boldsymbol{\tau} \right]. \quad (3.10)$$

From this equation it is obvious that the movement of the fluid is controlled by a combination of buoyancy of the fluid and the viscous stresses in the matrix. While the buoyancy term often dominates it is not always the case. In some cases the viscous stress term becomes dominant. Obviously, as stated before, the density differences here cannot be neglected with the Compaction Boussinesq Approximation, as they are a major driving force.

A nice observation can be made when the melt fraction and the viscosities are kept constant and the divergence of Eq. (3.10) is taken. It results in

$$-\varphi \vec{\nabla} \cdot (\vec{v}_f - \vec{v}_s) = \frac{\zeta + \frac{4}{3}\eta}{\mu} k_\varphi \nabla^2 (\vec{\nabla} \cdot \vec{v}_s). \quad (3.11)$$

Here the prefactor on the right side is called the compaction length δ_c

$$\delta_c = \sqrt{\frac{\zeta + \frac{4}{3}\eta}{\mu} k_\varphi}. \quad (3.12)$$

If Eq. (3.4) is used to eliminate $\varphi \vec{\nabla} \cdot (\vec{v}_f - \vec{v}_s)$ Eq. (3.11) becomes

$$\vec{\nabla} \cdot \vec{v}_s = \delta_c^2 \nabla^2 (\vec{\nabla} \cdot \vec{v}_s), \quad (3.13)$$

which can be solved for $\vec{\nabla} \cdot \vec{v}_s$ in 1D to give a solution of the form

$$\vec{\nabla} \cdot \vec{v}_s = C_1 e^{x/\delta_c} + C_2 e^{-x/\delta_c}. \quad (3.14)$$

This solution states that the compaction length δ_c is the characteristic length scale over which compaction takes place.

Further, a crucial point in this kind of equations is the understanding of the pressure. While P_f in the formulation is the pressure in the fluid, the pressure in the solid may be defined as well. Following McKenzie (1984) or Spiegelman et al. (2007) it may be defined as

$$P_s = -\frac{1}{3} \text{Tr}(\boldsymbol{\tau}) = P_f - \zeta \vec{\nabla} \cdot \vec{v}_s. \quad (3.15)$$

Rewriting it as $P_s - P_f = \zeta \vec{\nabla} \cdot \vec{v}_s$ implies that the difference of fluid to solid pressure drives the compaction or decompaction. If the pressure difference is positive (i.e. $P_f > P_s$) the divergence becomes positive and the matrix will expand or dilatate. If $P_f < P_s$ the matrix will contract or compact.

Usually it is convenient to reduce the number of unknown variables by expressing the matrix velocity \vec{v}_s as the sum of an incompressible, \vec{v}_1 , and a compressible part, \vec{v}_2 . \vec{v}_1 and \vec{v}_2 can be also stated as rotational and irrotational part, respectively. Following Sramek et al. (2012) the solid velocity can be written as

$$\vec{v}_s = \vec{v}_1 + \vec{v}_2 = \left(\begin{array}{c} \frac{\partial \Psi}{\partial z} \\ -\frac{\partial \Psi}{\partial x} \end{array} \right) + \left(\begin{array}{c} \frac{\partial \chi}{\partial x} \\ \frac{\partial \chi}{\partial z} \end{array} \right) \quad (3.16)$$

where Ψ is known as the stream function and χ is the irrotational velocity potential, which is defined by the Poisson equation

$$\vec{\nabla}^2 \chi = \vec{\nabla} \cdot \vec{v}_s. \quad (3.17)$$

The right side, the divergence term $\vec{\nabla} \cdot \vec{v}_s$ can be taken from Eq. (3.4). This definition for the solid velocity (Eq. (3.16)) can be put into the viscous stress tensor (Eq. (3.9)) and this into the Stokes equation (Eq. (3.8)). Eliminating the pressure by taking the curl results in

$$\left(\frac{\partial^2}{\partial x^2} - \frac{\partial^2}{\partial z^2} \right) \left[\eta \left(\frac{\partial^2 \Psi}{\partial x^2} - \frac{\partial^2 \Psi}{\partial z^2} \right) \right] + 4 \frac{\partial^2}{\partial x \partial z} \left(\eta \frac{\partial^2 \Psi}{\partial x \partial z} \right) = -g \frac{\partial \rho}{\partial x} + A(\chi) \quad (3.18)$$

with

$$A(\chi) = -2 \frac{\partial^2}{\partial x \partial z} \left[\eta \left(\frac{\partial^2 \chi}{\partial x^2} - \frac{\partial^2 \chi}{\partial z^2} \right) \right] + 2 \left(\frac{\partial^2}{\partial x^2} - \frac{\partial^2}{\partial z^2} \right) \left(\eta \frac{\partial^2 \chi}{\partial x \partial z} \right). \quad (3.19)$$

For the energy conservation equations, two separate equations could be written down, similar to the mass equations for solid and fluid (Eq. (3.1) and Eq. (3.2)). However, heat can diffuse between the matrix and the fluid and therefore the heat content is not conserved individually. Moreover, it is usually assumed that solid and fluid are in thermal equilibrium and that heat conductivities and capacities are the same. The assumption of thermal equilibrium is justified as the movement of fluid is usually much slower than the temperature diffusion. However, there are exceptions (see Schmeling et al., 2018). Under these assumptions, a single equation can be used for the solid-fluid mixture

$$\bar{\rho} c_P \left(\frac{\partial T}{\partial t} + \vec{v}_{bar} \cdot \vec{\nabla} T + \frac{\alpha g}{c_P} v_z T \right) = \vec{\nabla} \cdot (\lambda \vec{\nabla} T) + \bar{\rho} H + \psi - L \Gamma. \quad (3.20)$$

Here, c_P is the specific heat capacity, T is the temperature, α is the thermal expansion coefficient, λ is the thermal conductivity, H is the radiogenic heat generation rate per mass, ψ is the viscous dissipation and L is the latent heat per mass. Advection of the temperature is carried out using a barycentric velocity

$$\vec{v}_{bar} = \frac{\rho_f \varphi \vec{v}_f + \rho_s (1 - \varphi) \vec{v}_s}{\bar{\rho}}. \quad (3.21)$$

Each of the terms in Eq. (3.20) describe a heat source or sink. The first two terms on the left are associated with the change of heat due to temperature change and advection. The third term describes adiabatic heating, where the Boussinesq approximation is not assumed. On the right the first term gives conductive heat changes, the second term the additional heat due to radiogenic decay. The third term is the dissipated heat:

$$\psi = \frac{\mu \varphi^2}{k_\varphi} (\vec{v}_f - \vec{v}_s)^2 + \zeta \left(\vec{\nabla} \cdot \vec{v}_s \right)^2 + \frac{1}{2} \eta \left(\frac{\partial v_{si}}{\partial x_j} + \frac{\partial v_{sj}}{\partial x_i} - \frac{2}{3} \delta_{ij} \vec{\nabla} \cdot \vec{v}_s \right)^2. \quad (3.22)$$

The heat is produced due to relative movement between solid and fluid (term 1) and internal friction within the matrix, which consists of volumetric changes (term 2) and shear deformation (term 3). The last term in Eq. (3.20) is the latent heat, which is the energy released or absorbed due to phase changes.

The five equations that describe a two-phase flow system are Eqs. (3.1), (3.2), (3.5),

(3.8) and (3.20), but a few parameters need to be further addressed, because they additionally depend on other variables and change with time in a model, making it strongly non-linear. To address this problem, parameterizations for results of analogue experiments, like deformation tests, or simple laws (sometimes not so simple) are used. For example, the permeability of a rock depends on the porosity and the geometry of the pore space already shown in Eq. (3.6). Here k_φ is the result of a mathematical model describing the flow through a prescribed geometry (see Costa, 2006).

Viscosity Another big topic in modeling flows in geodynamics is the rheology of rocks. Rheology describes the flow capability of a certain material and can solely be a topic for numerous doctoral theses. In this thesis only a small percentage of this topic is addressed, namely the effect of melt fraction on the viscosity and a simple law for the temperature dependence on the viscosity.

The melt fraction has a big influence on the shear and volume viscosity and this effect is often described by a simple law of the form

$$\eta = \eta_0 (1 - \varphi) \quad (3.23)$$

$$\zeta = \eta_0 \frac{1 - \varphi}{\varphi}. \quad (3.24)$$

η_0 is the intrinsic shear viscosity of the matrix with zero porosity. With increasing melt fraction φ , the shear viscosity η decreases until it reaches 0 for $\varphi = 1$. The volume viscosity ζ comes from infinite and decreases to 0 with $\varphi = 1$ as well. This is a simple way to describe the viscosity, but experiments show that a typical material reaches a complete disaggregation for much smaller porosities. At this point single grains are no longer connected and the viscosity decreases strongly. Schmeling et al. (2012) proposed new viscosity laws that assume ellipsoidal melt inclusions, melt films or melt tubules embedded into a viscous matrix. Prescribing a geometry distribution, this formulation is able to self-consistently predict viscous weakening of a solid matrix. For a pore geometry consisting of solely films parameterized equations for the shear and volume viscosity can be given

$$\eta = \eta_0 \left(1 - \frac{\varphi}{c_1}\right)^{k_1} \quad \text{for } \varphi < c_1 \quad (3.25)$$

$$\zeta = \eta_0 c_2 \frac{(c_1 - \varphi)^{k_2}}{\varphi} \quad \text{for } \varphi < c_1 \quad (3.26)$$

with $k_1 = a_1(a_2 + \alpha(1 - a_2))$, $c_1 = \frac{b_1\alpha}{1 + b_2\alpha^{k_3}}$, $c_2 = \frac{4}{3}\alpha c_1^{-k_2} \cdot (c_3(1 - \alpha) + \alpha)$ where $a_1 = 0.97$, $a_2 = 0.8$, $b_1 = 2.2455$, $b_2 = 3.45$, $k_2 = 1.25$, $k_3 = 1.29$, $c_3 = 2$, and α is the aspect ratio of the ellipsoidal inclusions. This law predicts that the partially molten material completely disaggregates at a certain (low) melt fraction, found to be $\varphi = c_1$. Here both viscosities become zero.

For a geometry distribution of 50% tubes and 50% films the viscosities can be calculated using

$$\eta = \eta_0 \left(1 - \frac{\varphi}{\varphi_{max}}\right)^k \quad (3.27)$$

$$\zeta = \eta_0 a_2 \left(\frac{\varphi_{max} - \varphi}{\varphi} \right)^{b_2}. \quad (3.28)$$

With the parameters in Table 4.1 they can be calculated for different aspect ratios α . k is given by $k = a_1 \varphi + b_1$. In Fig. 4.1 all the viscosities described until here are shown. It can be seen that in contrast to the simple laws (Eqs. (3.23) and (3.24)), that achieve full disaggregation at a melt fraction of 100%, the more realistic laws achieve this at already very low melt fractions of about 20–40%. Melt network geometries combining tubes and films tend to have lower viscosity and disaggregation thresholds for a variety of aspect ratios of the films. Network geometries consisting solely of films give larger differences in viscosity for different α .

As already mentioned, there are many parameters that influence the viscosity. A major controlling parameter is the temperature. Usually the viscosity decreases with increasing temperature and this behavior can be described by a simple equation given by Turcotte and Schubert (2014):

$$\eta = \eta_{T_0} \cdot \exp \left[\frac{E_a}{RT_0} \left(\frac{T_0}{T} - 1 \right) \right]. \quad (3.29)$$

Here, η_{T_0} is the viscosity at $T = T_0$, E_a is the activation energy and R is the universal gas constant equal to $8.314 \text{ J mol}^{-1} \text{ K}^{-1}$. E_a is a physical parameter that can be taken from laboratory experiments for instance from Karato and Wu (1993) for olivine in the upper mantle. The resulting viscosity from Eq. (3.29) can then be used as the intrinsic shear viscosity η_0 in the equations for the porosity dependence of the viscosity to additionally take this effect into account.

The melting law The melting law usually used in our calculations is a simple representation of a two-component phase-diagram as it is shown in Fig. 3.1 after Schmeling et al. (2019), where melt and solid are always in thermodynamic equilibrium. A similar melting law already was introduced by Ribe (1985). A phase-diagram gives the melting temperature of a component A and a component B . A mixture of both of them results in a splitting of Solidus- and Liquidus-curve. With a temperature below the Solidus-temperature both components are solid. Increasing the temperature and passing the Solidus leads to a partially molten mixture, where both components melt simultaneously but with different melt fractions. Above the Liquidus both components are fully molten.

In reality Solidus and Liquidus are usually shaped like a cigar, but in our calculations we approximate these curves by two parallel lines with a constant difference between Solidus and Liquidus. This is a reasonable approximation as long as the concentrations are not too near to the edges of the diagram.

If a solid has a concentration of component B , c_s^B , and is heated above the Solidus the concentrations in the fluid, c_f^B , and the concentration in the solid, c_s^B , change following the diagram (Fig. 3.1). In equilibrium the melt fraction can be calculated following the lever rule

$$\varphi = \frac{c_s^B - c^B}{c_s^B - c_f^B}. \quad (3.30)$$

In a two-phase flow media, c_s^B and c_f^B are advected with different velocities and after one time increment solid and fluid might no longer be in thermodynamic equilibrium. The melt fraction then has to be adjusted to equilibrium, using a melting rate, given by

$$\frac{\Gamma}{\rho_0} = \frac{\varphi \frac{D^f c_f^B}{Dt} + (1 - \varphi) \frac{D^s c_s^B}{Dt}}{\Delta c}. \quad (3.31)$$

The operators $\frac{D^f}{Dt}$ and $\frac{D^s}{Dt}$ refer to the substantial time derivatives equal to $\frac{\partial}{\partial t} + \vec{v}_f \cdot \vec{\nabla}$ and $\frac{\partial}{\partial t} + \vec{v}_s \cdot \vec{\nabla}$ respectively. Δc is equal to the difference $c_s^B - c_f^B$.

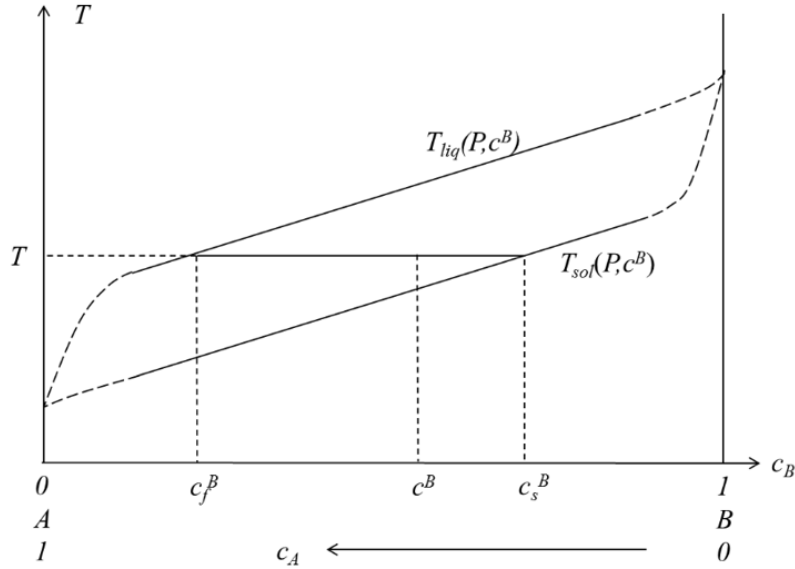


Figure 3.1: A simple phase-diagram for a two-component solid phase. On the abscissa the concentration of component B is given. The ordinate gives the temperature. The lower line in the diagram is the Solidus- and the upper one the Liquidus-temperature curve for a certain pressure as a function of concentration. After Schmeling et al. (2019).

3.2 Equations of Trace Element Transport with Melt

The transport of a trace element or a volatile can be described similar to Eqs. (3.1) and (3.2) and only the source term on the right side needs to be adapted to a different kind of behavior following the definition of the partition coefficient K_d . If a material is melted a trace element either prefers to stay in the solid or to go into the melt. This behavior is described by K_d which can be calculated with the concentration in the solid and fluid

$$K_d = \frac{c^s}{c^f}. \quad (3.32)$$

Here, c^s and c^f are the concentrations of the trace element in solid and fluid, respectively. A trace element that prefers to go into the melt is called *incompatible*, with

$K_d < 1$ and a trace element that prefers to stay in solid is called *compatible* with $K_d > 1$.

The following equations are stated in terms of trace element mass per volume and not concentration. The trace element mass per volume in solid is given by

$$m^s = c^s(1 - \varphi)\rho_s. \quad (3.33)$$

The trace element mass per volume in fluid by

$$m^f = c^f\varphi\rho_f. \quad (3.34)$$

As the behavior of partitioning between the phases is contrary for the case of melting and freezing, the exchange term needs to be changed for these cases. For melting ($\Gamma > 0$) we get after Spiegelman (1996)

$$\frac{\partial m^s}{\partial t} + \vec{\nabla} \cdot (\vec{v}_s m^s) = -\frac{\Gamma m^s}{K_d \rho_s (1 - \varphi)} + \frac{1}{t_r} \frac{K_d m^f (1 - \varphi) - m^s \varphi}{\varphi + K_d (1 - \varphi)} \quad (3.35)$$

and

$$\frac{\partial m^f}{\partial t} + \vec{\nabla} \cdot (\vec{v}_f m^f) = \frac{\Gamma m^s}{K_d \rho_s (1 - \varphi)} - \frac{1}{t_r} \frac{K_d m^f (1 - \varphi) - m^s \varphi}{\varphi + K_d (1 - \varphi)}. \quad (3.36)$$

In addition to the first term on the right, describing the exchange between solid and fluid due to melting, a re-equilibration term is introduced (2nd term on the right). This term describes the exchange between solid and fluid due to re-equilibration, which is not part of the equations in Spiegelman (1996). During melting and transport, trace elements are no longer in equilibrium, but they will incessantly try to achieve equilibrium by diffusion of elements through the solid-fluid boundary. t_r is the reaction time. To derive this term it is assumed that equilibrium can always be achieved by exchanging a certain amount of mass, Δm , between solid and fluid. Under this assumption one can state that

$$K_d = \frac{(m^s + \Delta m)\varphi}{(m^f - \Delta m)(1 - \varphi)} \quad (3.37)$$

is always true. Solving for Δm gives

$$\Delta m = \frac{K_d m^f (1 - \varphi) - m^s \varphi}{\varphi + K_d (1 - \varphi)}, \quad (3.38)$$

which can be together with t_r used as an exchange term in Eqs. (3.35) and (3.36). This term needs to be solved using time steps much smaller than t_r to achieve an exponential behavior. At $t = t_r$, $(1 - e^{-1})\Delta m$ is already transferred. The numerator of Eq. (3.38) is the difference between equilibrium and actual state. The denominator is a scaling factor. For $t_r = \infty$, equilibrium can never be achieved. $t_r = 0$ assumes instant equilibrium, which can be numerically achieved by setting $1/t_r$ to 1 and not iterating.

In the case of freezing ($\Gamma < 0$) incompatible elements prefer to stay in the melt and the 1st term on the right of Eqs. (3.35) and (3.36) need to be inverted. This results in

$$\frac{\partial m^s}{\partial t} + \vec{\nabla} \cdot (\vec{v}_s m^s) = -\frac{\Gamma K_d m^f}{\rho_f \varphi} + k_{equ} \frac{K_d m^f (1 - \varphi) - m^s \varphi}{\varphi + K_d (1 - \varphi)} \quad (3.39)$$

and

$$\frac{\partial m^f}{\partial t} + \vec{\nabla} \cdot (\vec{v}_f m^f) = \frac{\Gamma K_d m^f}{\rho_f \varphi} - k_{equ} \frac{K_d m^f (1 - \varphi) - m^s \varphi}{\varphi + K_d (1 - \varphi)}. \quad (3.40)$$

The change in the term can be better understood if we visualize what happens during melting and freezing using the definition of the partition coefficient (Eq. (3.32)). During melting a produced melt increment is in equilibrium with the solid, thus, following Eq. (3.32), c_f is equal to $\frac{c^s}{K_d}$. But during freezing a frozen solid increment is produced which is, again, in equilibrium with the fluid it originated from. Thus, the solid has a concentration of $c^s = c^f \cdot K_d$. This in terms of trace element mass with Eq. (3.34) gives $(K_d m^f) / (\varphi \rho_f)$, which is, together with Γ , the first exchange term in Eqs. (3.39) and (3.40).

In combination with the general equations for mass conservation (Eqs. (3.1) and (3.2)) one can eliminate the divergence of the velocities from the previous equations (Eqs. (3.35), (3.36), (3.39) and (3.40)) and write them in terms of concentration and no longer in terms of mass (see Spiegelman, 1996). The resulting equations for the case of melting are

$$\frac{\partial c^s}{\partial t} + \vec{v}_s \cdot \vec{\nabla} c^s = \frac{\Gamma c^s}{(1 - \varphi) \rho_s} \left(1 - \frac{1}{K_d}\right) + k_{equ} \frac{D \rho_f c^f - \rho_s c^s}{\varphi^2 (1 - \varphi) + D (1 - \varphi)^2 \varphi} \quad (3.41)$$

and

$$\frac{\partial c^f}{\partial t} + \vec{v}_f \cdot \vec{\nabla} c^f = \frac{\Gamma}{\varphi \rho_f} \left(\frac{c^s}{K_d} - c^f\right) - k_{equ} \frac{D \rho_f c^f - \rho_s c^s}{\varphi^2 (1 - \varphi) + D (1 - \varphi)^2 \varphi}. \quad (3.42)$$

In the case of freezing we get

$$\frac{\partial c^s}{\partial t} + \vec{v}_s \cdot \vec{\nabla} c^s = \frac{\Gamma}{(1 - \varphi) \rho_s} (c^s - c^f K_d) + k_{equ} \frac{D \rho_f c^f - \rho_s c^s}{\varphi^2 (1 - \varphi) + D (1 - \varphi)^2 \varphi} \quad (3.43)$$

and

$$\frac{\partial c^f}{\partial t} + \vec{v}_f \cdot \vec{\nabla} c^f = \frac{\Gamma c^f}{\varphi \rho_f} (K_d - 1) - k_{equ} \frac{D \rho_f c^f - \rho_s c^s}{\varphi^2 (1 - \varphi) + D (1 - \varphi)^2 \varphi}. \quad (3.44)$$

The advantage of these equations from a numerical point of view is that the divergence of the velocities have not to be calculated, but during freezing the concentrations go to infinity as φ goes to zero. The masses per volume go to zero, which is much easier to handle.

However, analytic equations can be calculated to analyze the behavior of trace elements in simple models. In a 0-D experiment where no re-equilibration takes place (i.e. $t_r = \infty$) Eqs. (3.41) to (3.44) can be reduced and the 2nd terms on the left and the right are dropped. If the melt fraction φ is assumed to be a function of time in the form of $\varphi(t) = \varphi_0 + \frac{\Gamma}{\rho_0} t$, where φ_0 is the initial melt fraction, the differential equations can be solved with $c^s(t=0) = c_0^s$ to give

$$c^s = c_0^s \left(\frac{1 - \varphi_0}{1 - \varphi(t)} \right)^{\left(1 - \frac{1}{K_d}\right)}, \quad (3.45)$$

which gives for $\varphi_0 = 0$ exactly the literature results (Eq. (2.11)) for fractional melting, but the equation is in a different form.

In the equation for the fluid c^f can be found, which has to be treated as function of time, what makes solving the differential equation rather unpleasant. If we only want the melt increment concentration, c_f can be calculated using $c_f(t) = c_s(t)/K_d$, which is done in the literature equations (Eq. (2.10)). If we want the concentration of the accumulated melt we can assume that c^s is constant, which is valid for rather small melt fractions. It gives

$$c^f = \frac{c_0^f \varphi_0}{\varphi(t)} + \frac{c^s}{D} \frac{\varphi(t) - \varphi_0}{\varphi(t)}. \quad (3.46)$$

This equation is only applicable for rather small melting degrees ($\varphi(t) - \varphi_0$). For bigger melting degrees c_f has to be solved semi-analytically.

For freezing, similar calculations can be carried out. Here, the equation for the fluid equation is not depending on solid equation and an exact solution can be calculated:

$$c^f = c_0^f \left(\frac{\varphi(t)}{\varphi_0} \right)^{K_d - 1}. \quad (3.47)$$

Again, this equation is exactly the literature equation for fractional crystallization (Eq. (2.13)), for $\varphi_0 = 1$. c^s can be calculated in a similar way while assuming c^f is constant:

$$c^s = -\frac{c_0^s (1 - \varphi_0)}{1 - \varphi(t)} - \frac{c^f K_d (\varphi(t) - \varphi_0)}{1 - \varphi(t)}. \quad (3.48)$$

3.3 Derivation of the Equations in the Publications

3.3.1 Publication 1

For the modeling of solitary porosity waves in publication 1, *The effect of effective rock viscosity on 2D magmatic porosity waves*, the energy equation for the mixture (Eq. (3.20)) is dropped and melting or freezing is forbidden (i.e. $\Gamma = 0$). The only change of porosity then is due to advection. With $\Gamma = 0$ the right side of the mass conservation equations (Eqs. (3.1) and (3.2)) are zero and the Compaction Boussinesq Approximation is applied (i.e. densities are constant in the mass equations), leading to

$$\frac{\partial \varphi}{\partial t} + \vec{\nabla} \cdot (\varphi \vec{v}_f) = 0 \quad (3.49)$$

and

$$\frac{\partial (1 - \varphi)}{\partial t} + \vec{\nabla} \cdot ((1 - \varphi) \vec{v}_s) = 0. \quad (3.50)$$

The momentum equations (Eqs. (3.10) and (3.18)) stay as they are and no further simplifications are carried out.

In this kind of solitary wave simulations the wave usually is placed into a partially molten background with porosity φ_0 . The compaction length, permeability and shear viscosity of this background is used to non-dimensionalize the general equations. For the viscosities the simplified relations Eqs. (3.23) and (3.24) or the fast declining

relations Eqs. (3.25) to (3.28), depending on the running model, is used. The viscosities for φ_0 are denoted η_{sc} and ζ_{sc} . The scaling permeability $k_{\varphi sc}$ is calculated using Eq. (3.6) for φ_0 . The scaling compaction length δ_{sc} then is defined as

$$\delta_{sc} = \sqrt{\frac{\eta_{sc} + \frac{4}{3}\zeta_{sc}}{\mu}} k_{\varphi sc}. \quad (3.51)$$

The velocity is non-dimensionalized by the background separation velocity given by

$$v_{sc} = \frac{k_{\varphi sc}}{\mu\varphi_0} (\rho_s - \rho_f) g. \quad (3.52)$$

With these scaling parameters the set of scaling law is defined as

$$\begin{aligned} \vec{x} &= \delta_{sc} \vec{x}' & \vec{v} &= v_{sc} \vec{v}' & t &= \frac{\delta_{sc}}{v_{sc}} t' & \tau_{ij} &= \eta_{sc} \frac{v_{sc}}{\delta_{sc}} \tau_{ij}' \\ \eta &= \eta_{s0} \eta' & \rho &= \rho_s \rho' & \varphi &= \varphi_0 \varphi' & (\psi, \chi) &= (\psi', \chi') \cdot \delta_{sc} v_{sc} \end{aligned} \quad (3.53)$$

where non-dimensional parameters are primed.

In the mass equations, variables can be replaced by their non-dimensional counterpart, giving

$$\frac{\partial \varphi'}{\partial t'} + \vec{\nabla}' \cdot (\varphi' \vec{v}'_f) = 0 \quad (3.54)$$

and

$$\frac{\partial (1 - \varphi')}{\partial t'} + \vec{\nabla}' \cdot ((1 - \varphi') \vec{v}'_s) = 0. \quad (3.55)$$

The momentum equations become

$$\begin{aligned} \left(\frac{\partial^2}{\partial x'^2} - \frac{\partial^2}{\partial z'^2} \right) \left[\eta' \left(\frac{\partial^2 \psi'}{\partial x'^2} - \frac{\partial^2 \psi'}{\partial z'^2} \right) \right] + 4 \frac{\partial^2}{\partial x' \partial z'} \left(\eta' \frac{\partial^2 \psi'}{\partial x' \partial z'} \right) \\ = \varphi_0^2 \frac{\zeta_{sc} + \frac{4}{3} \eta_{sc}}{\eta_{sc}} \frac{\partial \varphi'}{\partial x'} + A(\chi') \end{aligned} \quad (3.56)$$

with

$$A(\chi') = -2 \frac{\partial^2}{\partial x' \partial z'} \left[\eta' \left(\frac{\partial^2 \chi'}{\partial x'^2} - \frac{\partial^2 \chi'}{\partial z'^2} \right) \right] + 2 \left(\frac{\partial^2}{\partial x'^2} - \frac{\partial^2}{\partial z'^2} \right) \left(\eta' \frac{\partial^2 \chi'}{\partial x' \partial z'} \right) \quad (3.57)$$

and

$$\vec{v}'_f - \vec{v}'_s = \varphi'^{m-1} \left[(1 - \varphi_0 \varphi') \vec{e}_z - \frac{\eta_{sc}}{(\zeta_{sc} + \frac{4}{3} \eta_{sc}) \varphi_0} \frac{1}{\partial x_j'} \frac{\partial \tau_{ij}'}{\partial x_j'} \right]. \quad (3.58)$$

The whole equation system is described by Eqs. (3.54) to (3.58).

3.3.2 Publication 2

In publication 2, *Magma ascent mechanisms in the transition regime from solitary porosity waves to diapirism*, the transition between solitary waves and diapirism is investigated. While the non-dimensionalization of publication 1 is useful for solitary waves it can not be used for the diapirism end-member because the separation velocity will tend to go to zero. Therefore, instead of the compaction length the initial radius of the placed anomaly, r , is used. The background separation velocity is replaced by the Stokes sphere velocity, v_{St} , of the initial perturbation and the background porosity φ_0 is replaced by the initial maximum porosity of the perturbation, φ_{max} .

With this modification, the non-dimensionalization looks as follows:

$$\begin{aligned} (x, z) &= (x', z') \cdot r & \vec{v}_{s,f} &= \vec{v}'_{s,f} \cdot v_{St} & t &= t' \cdot \frac{r}{v_{St}} \\ (\boldsymbol{\tau}, P) &= (\boldsymbol{\tau}', P') \cdot \frac{\eta_0 v_{St}}{r} & (\eta, \zeta) &= (\eta', \zeta') \cdot \eta_0 & (\psi, \chi) &= (\psi', \chi') \cdot r v_{St} \end{aligned} \quad (3.59)$$

For the radius, r , the half-width of the initial perturbation, consisting of a 2D Gaussian bell, is chosen. The Stokes sphere velocity can be calculated using the literature equation (e.g. Turcotte and Schubert, 2014)

$$v_{St} = C_{st} \frac{\varphi_{max} \Delta \rho g r^2}{\eta_0}. \quad (3.60)$$

C_{St} can be achieved applying the analytic solution for an infinite Stokes cylinder within another large cylinder, which describes our model setup sufficiently. This is necessary as there is no analytic solution for a Stokes cylinder in an infinite medium. Following Popov and Sobolev (2008) with the drag force derived by Slezkin (1955) C_{St} can be calculated using $C_{St} = \ln(k) - \frac{k^2-1}{k^2+1}$, where k is the ratio of outer to inner cylinder radius. For our model setup we arrive at $C_{St} = 0.17$.

In non-dimensional form the momentum equation (Eq. (3.10)) becomes

$$\vec{v}'_f - \vec{v}'_s = -\frac{\delta_c^2}{r^2} \frac{1}{\tilde{\eta}' \varphi} \left(\vec{e}_z \frac{(1-\varphi)}{\varphi_{max}} + \vec{\nabla}' \cdot \boldsymbol{\tau}' \right) \quad (3.61)$$

where $\tilde{\eta}'$ is equal to $\zeta' + \frac{4}{3}\eta'$. The momentum equation of the mixture becomes

$$\left(\frac{\partial^2}{\partial x'^2} - \frac{\partial^2}{\partial z'^2} \right) \left[\eta' \left(\frac{\partial^2 \psi'}{\partial x'^2} - \frac{\partial^2 \psi'}{\partial z'^2} \right) \right] + 4 \frac{\partial^2}{\partial x' \partial z'} \left(\eta' \frac{\partial^2 \psi'}{\partial x' \partial z'} \right) = \frac{1}{\varphi_{max}} \frac{\partial \varphi}{\partial x'} + A'(\chi'). \quad (3.62)$$

All other equations can be taken from the previous section. The system is then described by Eqs. (3.54), (3.55), (3.57), (3.61) and (3.62).

In Eq. (3.61) δ_c^2/r^2 is the squared ratio of compaction length to initial perturbation radius and is the main parameter describing the system. In the methods section of publication 2, a comparison of segregation to Stoke velocity, based on this ratio, is carried out and therefore, not shown here.

3.3.3 Publication 3

Publication 3, *Modeling trace element transport in melt using two-phase flow: Investigation of element redistribution in the upper Earth*, concerns with modeling upper mantle convection, which requires the full set of equations for two-phase flow, consisting of two mass conservation equations for fluid and solid (Eqs. (3.1) and (3.2)), two momentum conservation equations, one for the fluid (Eq. (3.5)), one for the solid-fluid mixture (Eq. (3.8)), and one energy conservation equation for the mixture in thermal equilibrium (Eq. (3.20)). The equation of energy conservation has to be solved as the model is no longer isothermal. In this kind of convection model, thermal evolution and the resulting effect on density due to thermal expansion is a major driving force and has to be included.

Additionally, the transport of trace elements is modeled, using equations conserving the mass per volume of the elements in solid and fluid separately (Eqs. (3.35), (3.36), (3.39) and (3.40)). It should be noted again, that the source term of these equations has to be changed whether material is freezing ($\Gamma < 0$) or melting ($\Gamma > 0$).

To achieve fully self consistent material exchange between the two phases a simple two-component melting law is used (Eq. (3.31), Fig. 3.1).

Shear and volume viscosities are temperature and melt fraction dependent and their functions are defined by

$$\eta = \eta_0 \cdot \exp \left[\frac{E_a}{RT_0} \left(\frac{T}{T_0} - 1 \right) \right] \cdot \left(1 - \frac{\varphi}{c_1} \right)^{k_1}, \quad (3.63)$$

$$\zeta = \eta_0 \cdot \exp \left[\frac{E_a}{RT_0} \left(\frac{T}{T_0} - 1 \right) \right] \cdot c_2 (c_1 - \varphi)^{k_2/\varphi}. \quad (3.64)$$

The first part, with the exponential function, of both equations describes the dependence of the temperature (Turcotte and Schubert, 2014) on the viscosity and contains the activation energy E_a , the universal gas constant R and a reference temperature T_0 , which is the temperature where $\eta = \eta_0$.

The melt fraction dependence is described by the second part of the equations and originates in the viscosity laws of Schmeling et al. (2012). These are based on numerical calculations for the viscous weakening of a prescribed melt geometry, merely build of melt films (Eqs. (3.25) and (3.26)). The viscosity values can be calculated with $k_1 = a_1 (a_2 + \alpha (1 - a_2))$, $c_1 = \frac{b_1 \alpha}{1 + b_2 \alpha^{k_3}}$, $c_2 = \frac{4}{3} \alpha c_1^{-k_2} \cdot (c_3 (1 - \alpha) + \alpha)$ where $a_1 = 0.97$, $a_2 = 0.8$, $b_1 = 2.2455$, $b_2 = 3.45$, $k_2 = 1.25$, $k_3 = 1.29$, $c_3 = 2$. α is the aspect ratio of the ellipsoidal inclusions equal to 0.03.

A different scaling has to be used here, as neither Stokes spheres nor porosity waves are investigated. In convection models it is useful to use the thickness of the model box to scale distance, and thermal diffusivity κ for time and eventually velocity. Additionally, the model is no longer isothermal and temperature needs to be scaled. Concentrations are scaled by the initial concentration of the model c_0 . The scaling law now looks like

this:

$$\begin{aligned}
 (x, z) &= (x', z') \cdot h & \vec{v}_{s,f} &= \vec{v}'_{s,f} \cdot \frac{\kappa}{h} & t &= t' \cdot \frac{h^2}{\kappa} & T &= T' \cdot T_{sc} & \rho &= \rho' \cdot \rho_0 \\
 (\boldsymbol{\tau}, P) &= (\boldsymbol{\tau}', P') \cdot \frac{\eta_0 \kappa}{h^2} & (\eta, \zeta) &= (\eta', \zeta') \cdot \eta_0 & c_{s,f} &= c'_{s,f} \cdot c_0 & L &= L' \cdot c_P T_{sc}.
 \end{aligned} \tag{3.65}$$

To carry out parameter studies it is useful to introduce non-dimensional numbers, based on the scaling parameters in Eq. (3.65):

$$\begin{aligned}
 Ra &= \frac{\rho_0 g \alpha \Delta T h^3}{\eta_0 \kappa}, & Ra_m &= \frac{\Delta \rho_f g h^3}{\eta_0 \kappa} \\
 Ra_e &= \frac{\Delta \rho_e g h^3}{\eta_0 \kappa}, & Rt &= \frac{\eta_f h^2}{\eta_0 k_0}.
 \end{aligned} \tag{3.66}$$

Ra , Ra_m and Ra_e are the Rayleigh numbers that represent the buoyancy due to temperature, melt density and enrichment density, respectively. Rt is the retention number and describes the resistance of a fluid to percolate through a porous matrix. The densities that drive the buoyancy can be calculated using

$$\begin{aligned}
 \bar{\rho} &= \rho_0 - \rho_0 \alpha T - \Delta \rho_f \varphi - \Delta \rho_e f (1 - \varphi), \\
 \rho_s &= \rho_0 - \rho_0 \alpha T - \Delta \rho_e f (1 - \varphi), \\
 \rho_f &= \rho_0 - \rho_0 \alpha T - \Delta \rho_f.
 \end{aligned} \tag{3.67}$$

$\bar{\rho}$ is the mixture density, $\Delta \rho_f$ is the density contrast between the solid and its melt, and $\Delta \rho_e$ is the difference between the initial and the completely enriched material. f is the degree of depletion or enrichment, which is defined as the normalized concentration of the solid as

$$f = \frac{c_s^B}{c_s^B - c_f^B} - c_0^B. \tag{3.68}$$

Note that $c_s^B - c_f^B$ is constant in our simplified phase diagram. c_0^B is the initial concentration of component B . $f > 0$ relates to an enrichment of component B , while $f < 0$ relates to a depletion of component B .

Using the non-dimensional numbers and the scaling law in our two-phase flow formulation we arrive for the momentum equations of the fluid (Eq. (3.5)) at

$$\vec{v}'_f - \vec{v}'_s = -\frac{\varphi^{n-1}}{Rt} \left(\vec{\nabla}' P'_f - Rm \cdot \delta_{i3} \right), \tag{3.69}$$

where non-dimensional values are primed.

The non-dimensionalized momentum equation for the mixture (Eq. (3.8)) becomes

$$(Ra \cdot T' + Ra_m \cdot \varphi + Ra_e \cdot f (1 - \varphi)) \delta_{i3} - \vec{\nabla}' P'_f + \vec{\nabla}' \boldsymbol{\tau}' = 0. \tag{3.70}$$

The equation for conservation of energy can be non-dimensionalized, as well, to give

$$\frac{\partial T'}{\partial t'} + v_{bar}' \cdot \vec{\nabla}' T' = \vec{\nabla}' \cdot \left(\rho' \vec{\nabla}' T' \right) + \rho_0 L' \Gamma'. \tag{3.71}$$

3.3.4 Unpublished Manuscript

In this manuscript, *Transport of volatiles and trace elements in solitary porosity waves*, the mass transport capabilities of solitary waves are investigated. The usual two-phase flow equations for solitary waves, as applied in publication 1 and 2, are used. They consist of mass conservation equations for the fluid (Eq. (3.50)) and solid (Eq. (3.49)), both with the source term equal to zero, and a momentum conservation equation for the mixture (Eq. (3.56)) and fluid (Eq. (3.58)). The model is assumed to be isothermal again as melting and freezing is not allowed, and thermal expansion is neglected.

To observe the transport of mass, equations for the conservation of trace elements are introduced

$$\frac{\partial c^s}{\partial t} + \vec{v}_s \cdot \vec{\nabla} c^s = 0 \quad (3.72)$$

and

$$\frac{\partial c^f}{\partial t} + \vec{v}_f \cdot \vec{\nabla} c^f = 0. \quad (3.73)$$

Those equations are solved using an explicit upwind scheme. c^s and c^f are concentrations, but as melting and freezing is not allowed, no exchange is taking place between solid and fluid, and the values are rather used to depict the origin of the markers. Additionally, a marker field, following the fluid velocity, is introduced to allow for numerical diffusion free advection. The equation is the same as Eq. (3.73), but is solved using 4th order Runge-Kutta method.

References

- Bercovici, D., Ricard, Y., and Schubert, G. (2001). A two-phase model for compaction and damage: 1. General Theory. *Journal of Geophysical Research*, 106(B5):8887.
- Costa, A. (2006). Permeability-porosity relationship: A reexamination of the Kozeny-Carman equation based on a fractal pore-space geometry assumption. *Geophysical Research Letters*, 33(2):1–5.
- Karato, S.-I. and Wu, P. (1993). Rheology the Upper Mantle : Synthesis. *Science*, 260(May).
- McKenzie, D. (1984). The generation and compaction of partially molten rock. *Journal of Petrology*, 25(3):713–765.
- Popov, A. A. and Sobolev, S. V. (2008). SLIM3D: A tool for three-dimensional thermo-mechanical modeling of lithospheric deformation with elasto-visco-plastic rheology. *Physics of the Earth and Planetary Interiors*, 171(1-4):55–75.
- Ribe, N. M. (1985). The generation and composition of partial melts in the earth’s mantle. *Earth and Planetary Science Letters*.
- Schmeling, H. (2000). *Partial melting and melt segregation in a convecting mantle*. Springer.
- Schmeling, H., Kruse, J. P., and Richard, G. C. (2012). Effective shear and bulk viscosity of partially molten rock based on elastic moduli theory of a fluid filled poroelastic medium. *Geophysical Journal International*, 190(3):1571–1578.
- Schmeling, H., Marquart, G., and Grebe, M. (2018). A porous flow approach to model thermal non-equilibrium applicable to melt migration. *Geophysical Journal International*, 212:119–138.
- Schmeling, H., Marquart, G., Weinberg, R., and Wallner, H. (2019). Modelling melting and melt segregation by two-phase flow: New insights into the dynamics of magmatic systems in the continental crust. *Geophysical Journal International*, 217(1):422–450.
- Slezkin, A. (1955). Dynamics of viscous incompressible fluid. *Moscow (in Russian)*.
- Spiegelman, M. (1996). Geochemical consequences of melt transport in 2-D: The sensitivity of trace elements to mantle dynamics. *Earth and Planetary Science Letters*, 139:115–132.
- Spiegelman, M., Katz, R. F., and Simpson, G. (2007). An Introduction and Tutorial to the “McKenzie Equations” for magma migration. *Lecture Notes*, pages 1–14.
- Sramek, O., Milelli, L., Ricard, Y., and Labrosse, S. (2012). Thermal evolution and differentiation of planetesimals and planetary embryos. *Icarus*, 217(1):339–354.
- Turcotte, D. L. and Schubert, G. (2014). *Geodynamics*. Cambridge University Press, 3. edition.

Chapter 4

Publication 1

The Effect of effective Rock Viscosity on 2D Magmatic Porosity Waves

Solid Earth 10:2103-2113 (2019)

Janik Dohmen¹, Harro Schmeling¹ & Jan Philipp Kruse¹

¹Institute for Geoscience, Goethe University Frankfurt, Frankfurt, Germany

Abstract

In source regions of magmatic systems the temperature is above solidus and melt ascent is assumed to occur predominantly by two-phase flow which includes a fluid phase (melt) and a porous deformable matrix. Since McKenzie (1984) introduced his equations for two-phase flow, numerous solutions have been studied one of which predicts the emergence of solitary porosity waves. By now most analytical and numerical solutions for these waves used strongly simplified models for the shear- and bulk viscosity of the matrix, significantly overestimating the viscosity or completely neglecting the porosity-dependence of the bulk viscosity. Schmeling et al. (2012) suggested viscosity laws in which the viscosity decreases very rapidly for small melt fractions. They are incorporated into a 2D Finite Difference mantle convection code with two-phase flow (FDCON) to study the ascent of solitary porosity waves. The models show that, starting with a Gaussian shaped wave, they rapidly evolve into a solitary wave with similar shape and a certain amplitude. Despite the strongly weaker rheologies compared to previous viscosity laws the effect on dispersion curves and wave shape are only moderate as long as the background porosity is fairly small. The models are still in good agreement with semi-analytic solutions which neglect the shear stress term in the melt segregation equation. However, for higher background porosities and wave amplitudes associated with a viscosity decrease of 50% or more, the phase velocity and the width of the waves are significantly decreased. Our models show that melt ascent by solitary waves is still a viable mechanism even for more realistic matrix viscosities.

4.1 Introduction

Magmatic phenomena such as volcanic eruptions on the Earth's surface show, among others, that melt is able to ascend from partially molten regions in the Earth's mantle. The melt initially segregates through the partially molten source region and then ascends through the unmolten lithosphere until it eventually reaches the surface. Within supersolidus source regions at low melt fractions melt is assumed to slowly percolate by two-phase porous flow within a deforming matrix (McKenzie, 1984; Schmeling, 2000; Bercovici et al., 2001), followed by melt accumulation within rising high porosity waves (Scott and Stevenson, 1984; Spiegelman, 1993; Wiggins and Spiegelman, 1995; Richard et al., 2012) or focusing into channels which can possibly penetrate into subsolidus regions. Stevenson (1989) carried out a linear stability analysis and found conditions at which flow instabilities may arise, which may result in different 3D shapes like elongated pockets, channels or porosity waves (Richardson, 1998; Wiggins and Spiegelman, 1995). Formation of 3D channels within a deforming matrix have been demonstrated in Omlin et al. (2018) or Räss et al. (2014). Here we focus on the supersolidus source region, and in particular on the dynamics of porosity waves. An essential parameter controlling the width and phase velocity of porosity waves is the effective shear and bulk matrix viscosity (Simpson and Spiegelman, 2011; Richard et al., 2012). Most of the porosity wave model approaches used either equal bulk and shear viscosities, or simple laws in the form of

$$\eta_s = \eta_{s0} (1 - \varphi) \quad (4.1)$$

$$\eta_b = \eta_{s0} C \frac{(1 - \varphi)}{\varphi^m} \quad (4.2)$$

where η_s is the effective shear viscosity of the matrix, η_b the bulk viscosity, η_{s0} the intrinsic shear viscosity of the matrix, C a constant of order 1, φ the porosity, and $m = 0$ for equal shear and bulk viscosities or $m = 1$ otherwise. There are also recent models that use more complex pressure dependent weakening viscosities but they still use the simplified equations mentioned above for the porosity dependence of the viscosity (Omlin et al., 2018; Yarushina et al., 2015). Schmeling et al. (2012) developed an effective viscosity model depending on a simplified geometry of the fluid phase within a viscous matrix. Possible melt geometries include flat, ellipsoid-shaped melt inclusions with an aspect ratio α and melt tubes with circular or triangular cross sections with tapered edges. Comparison of the previous viscosity laws, Eqs. (4.1) and (4.2), with the ones by Schmeling et al. (2012) clearly shows that for aspect ratio 1 and particularly for smaller α the effective matrix viscosities are significantly weaker, and disaggregation of the solid occurs at melt fractions significantly smaller than 100% as predicted by laws (4.1) and (4.2). Recent viscosity models based on microscopic diffusion through grains, grain faces and the melt phase confirm the significance of weakening with respect to Eqs. (4.1) and (4.2) (Rudge, 2018). The aim of this study is to model 2D-porosity waves with the viscosity laws by Schmeling et al. (2012) and test the influence of the weaker rheology on their shape and ascent velocity in the absence of melting or freezing.

4.2 Theoretical Approach

4.2.1 Governing Equations

The mathematical formulation of differential movement between solid matrix and melt basically builds on that described in Schmeling (2000) and Schmeling et al. (2019) and is applied here to a porosity wave. We solve the equations for mass and momentum conservation for melt and solid. The formulation of the governing equations for the melt-in-solid two-phase flow dynamics is based on McKenzie (1984), Spiegelman and McKenzie (1987) and Schmeling (2000) and is valid for infinite Prandtl number (i.e. neglecting inertia terms in the momentum equations), and small fluid to matrix viscosity ratios. In the following all variables associated with the fluid (melt) have the subscript f and those associated with the solid have the subscript s. Without melting and freezing the equation for the conservation of the mass of the melt is

$$\frac{\partial \varphi}{\partial t} + \vec{\nabla} \cdot (\varphi \vec{v}_f) = 0 \quad (4.3)$$

and the mass conservation of the solid is

$$\frac{\partial (1 - \varphi)}{\partial t} + \vec{\nabla} \cdot [(1 - \varphi) \vec{v}_s] = 0. \quad (4.4)$$

\vec{v}_f and \vec{v}_s are the fluid and solid velocities, respectively. The velocities are derived from the momentum equations, which is a generalized Darcy equation for the fluid separation flow

$$\vec{v}_f - \vec{v}_s = -\frac{k_\varphi}{\eta_f \varphi} \left(\vec{\nabla} P - \rho_f \vec{g} \right), \quad (4.5)$$

and the Stokes equation for the solid-fluid mixture in the limit of zero fluid viscosity

$$\rho \vec{g} - \vec{\nabla} P + \frac{\partial \tau_{ij}}{\partial x_j} = 0. \quad (4.6)$$

k_φ is the permeability that depends on the rock porosity (i.e. melt fraction) with the power n

$$k_\varphi = k_0 \varphi^n, \quad (4.7)$$

η_f is the dynamic melt viscosity, \vec{g} is the gravitational acceleration, ρ is the density of the melt – solid mixture, ρ_f is the density of the melt, P is the fluid pressure, whose gradient is driving the motion, and τ_{ij} is the effective viscous stress tensor of the matrix

$$\tau_{ij} = \eta_s \left(\frac{\partial v_{si}}{\partial x_j} + \frac{\partial v_{sj}}{\partial x_i} \right) + \left(\eta_b - \frac{2}{3} \eta_s \right) \delta_{ij} \vec{\nabla} \cdot \vec{v}_s \quad (4.8)$$

with the effective shear viscosity η_s and the effective volumetric or bulk viscosity η_b of the porous matrix. The term $(\eta_b - \frac{2}{3} \eta_s) \vec{\nabla} \cdot \vec{v}_s$ is often referred to as compaction pressure. The linearized equation of state for the mixture density is given as

$$\rho = \rho_f \varphi + \rho_s (1 - \varphi) \quad (4.9)$$

with the density of the matrix ρ_s . The fluid pressure in Eqs. (4.5) and (4.6) is the same and can be eliminated by merging the two equations. Inserting the density of the mixture, and using Eq. (4.7), Eq. (4.5) is recast into

$$\vec{v}_f - \vec{v}_s = -\frac{k_0\varphi^{n-1}}{\eta_f} \left(\vec{g}(\rho_s - \rho_f)(1 - \varphi) + \frac{\partial\tau_{ij}}{\partial x_j} \right). \quad (4.10)$$

This equation states that the velocity difference between fluid and solid phase (i.e. fluid separation flow, or the segregation velocity) is driven by the buoyancy of the fluid with respect to the solid, and the viscous stress in the matrix which includes the compaction pressure. Following Sramek et al. (2007) the matrix velocity, \vec{v}_s , can be written as the sum of the incompressible flow velocity, \vec{v}_1 , and the irrotational (compaction) flow velocity, \vec{v}_2 , as follows:

$$\vec{v}_s = \vec{v}_1 + \vec{v}_2 = \left(\frac{\partial\psi}{\partial z}, -\frac{\partial\psi}{\partial x} \right) + \left(\frac{\partial\chi}{\partial x}, \frac{\partial\chi}{\partial z} \right) \quad (4.11)$$

with the incompressible velocity potential or stream function ψ and the irrotational (compaction related) velocity potential, χ . From Eq. (4.11) it follows that the latter is given as the solution of the Poisson equation

$$\nabla^2\chi = \vec{\nabla} \cdot \vec{v}_s \quad (4.12)$$

The divergence term $\vec{\nabla} \cdot \vec{v}_s$ can be derived from summing up Eq. (4.3) and Eq. (4.4) to give

$$\vec{\nabla} \cdot \vec{v}_s = -\vec{\nabla} \cdot [\varphi(\vec{v}_f - \vec{v}_s)] \quad (4.13)$$

Eq. (4.12) represents a Poisson equation which can be solved for χ once the melt porosity and segregation velocity are known. As boundary condition the normal velocity of \vec{v}_2 , i.e. v_{2n} , can be prescribed which is equivalent to a normal derivative of χ , i.e. a Neuman boundary condition. If the normal velocity is constant along the boundary, it automatically fulfils free slip. For sake of simplicity $v_{2n} = 0$ was chosen. Taking the curl of the matrix momentum Eq. (4.6) eliminates the pressure. Inserting the viscous stress tensor (Eq. (4.8)), the density (Eq. (4.9)) and the matrix velocity (Eq. (4.11)) into the resulting equation gives the momentum equation in terms of the stream function ψ and the irrotational velocity potential χ

$$\begin{aligned} \left(\frac{\partial^2}{\partial x^2} - \frac{\partial^2}{\partial z^2} \right) \left[\eta_s \left(\frac{\partial^2\psi}{\partial x^2} - \frac{\partial^2\psi}{\partial z^2} \right) \right] + 4 \frac{\partial^2}{\partial x\partial z} \left[\eta_s \frac{\partial^2\psi}{\partial x\partial z} \right] \\ = (\rho_s - \rho_f) g \frac{\partial\varphi}{\partial x} + A(\chi) \end{aligned} \quad (4.14)$$

with

$$A(\chi) = -2 \frac{\partial^2}{\partial x\partial z} \left[\eta_s \left(\frac{\partial^2\chi}{\partial x^2} - \frac{\partial^2\chi}{\partial z^2} \right) \right] + 2 \left(\frac{\partial^2}{\partial x^2} - \frac{\partial^2}{\partial z^2} \right) \left[\eta_s \frac{\partial^2\chi}{\partial x\partial z} \right] \quad (4.15)$$

The governing equations are non-dimensionalized by the compaction length, δ_{c0} , (McKenzie, 1984) and a scaling separation velocity, v_{sc0} , both of which are taken at a reference

state which assumes a constant background porosity φ_0 . The corresponding scaling viscosities and the scaling permeability are denoted by η_{b0} , η_{s0} , and $k_{\varphi 0}$, respectively. The compaction length is given by

$$\delta_{c0} = \left(\frac{\eta_{b0} + \frac{4}{3}\eta_{s0}k_{\varphi 0}}{\eta_f} \right)^{\frac{1}{2}} \quad (4.16)$$

and is the length scale over which a variation in fluid flux gives a response on the compaction. The scaling separation velocity is given as

$$v_{sc0} = \frac{k_{\varphi 0}}{\eta_f \varphi_0} (\rho_s - \rho_f) g. \quad (4.17)$$

This defines the scaling law, where the primes denote non-dimensional values and the subscript 0 refers to the background porosity

$$\begin{aligned} \vec{x} &= \delta_{c0} \vec{x}' & \vec{v} &= v_{sc0} \vec{v}' & t &= \frac{\delta_{c0}}{v_{sc0}} t' & \tau_{ij} &= \eta_{s0} \frac{v_{sc0}}{\delta_{c0}} \tau'_{ij} \\ \eta &= \eta_{s0} \eta' & \rho &= \rho_s \rho' & \varphi &= \varphi_0 \varphi' \end{aligned} \quad (4.18)$$

The resulting governing equations for the mass are

$$\frac{\partial(1 - \varphi')}{\partial t'} + \vec{\nabla}' \cdot ((1 - \varphi') \vec{v}'_s) = 0 \quad (4.19)$$

$$\frac{\partial \varphi'}{\partial t'} + \vec{\nabla}' \cdot (\varphi' \vec{v}'_f) = 0 \quad (4.20)$$

and for the momentum equations we get

$$\begin{aligned} \left(\frac{\partial^2}{\partial x'^2} - \frac{\partial^2}{\partial z'^2} \right) \left[\eta'_s \left(\frac{\partial^2 \psi'}{\partial x'^2} - \frac{\partial^2 \psi'}{\partial z'^2} \right) \right] + 4 \frac{\partial^2}{\partial x' \partial z'} \left[\eta'_s \frac{\partial^2 \psi'}{\partial x' \partial z'} \right] \\ = \varphi_0^2 \frac{\eta_{b0} + \frac{4}{3}\eta_{s0}}{\eta_{s0}} \frac{\partial \varphi'}{\partial x'} + A(\chi') \end{aligned} \quad (4.21)$$

$$A(\chi') = -2 \frac{\partial^2}{\partial x' \partial z'} \left[\eta'_s \left(\frac{\partial^2 \chi'}{\partial x'^2} - \frac{\partial^2 \chi'}{\partial z'^2} \right) \right] + 2 \left(\frac{\partial^2}{\partial x'^2} - \frac{\partial^2}{\partial z'^2} \right) \left[\eta'_s \frac{\partial^2 \chi'}{\partial x' \partial z'} \right] \quad (4.22)$$

$$\vec{v}'_f - \vec{v}'_s = \varphi'^{m-1} \left[(1 - \varphi_0 \varphi') \vec{e}_z - \frac{\eta_{s0}}{(\eta_{b0} + \frac{4}{3}\eta_{s0}) \varphi_0} \frac{\partial \tau'_{ij}}{\partial x'_j} \right] \quad (4.23)$$

with \vec{e}_z as unit vector in z-direction (positive upward).

4.2.2 The effective Viscosity of a Porous Matrix

The effective viscosity laws proposed by Schmeling et al. (2012) assume ellipsoidal melt inclusions, or melt films if the inclusions are flat, or melt tubules embedded within an effective viscous medium. This self-consistent assumption is able to predict viscous weakening of a solid matrix with a disaggregation melt porosity of the order of

Table 4.1: Parameters to calculate the viscosities for a melt network consisting of 50% tubes and 50% films using Eqs. (4.26) and (4.27)

α	a_1	a_2	b_1	b_2	φ_{max}
0.2	0.8074	2.595	0.7009	1.276	0.2428
0.3	0.7435	2.622	0.7082	1.278	0.2629
0.4	0.6958	2.645	0.7145	1.281	0.2730
0.5	0.6692	2.664	0.7182	1.284	0.2785

50% or less depending on the assumed melt geometry. From their numerical models Schmeling et al. (2012) derive approximate formulas for the porosity dependence of the dimensional effective matrix shear and bulk viscosities for a melt network geometry consisting of 100% films

$$\eta_s = \eta_{s0} \left(1 - \frac{\varphi}{c_1}\right)^{k_1} \quad \text{for } \varphi < c_1 \quad (4.24)$$

$$\eta_b = \eta_{s0} c_2 \frac{(c_1 - \varphi)^{k_2}}{\varphi} \quad \text{for } \varphi < c_1 \quad (4.25)$$

with $k_1 = a_1(a_2 + \alpha(1 - a_2))$, $c_1 = \frac{b_1\alpha}{1 + b_2\alpha^{k_3}}$, $c_2 = \frac{4}{3}\alpha c_1^{-k_2} \cdot (c_3(1 - \alpha) + \alpha)$ where $a_1 = 0.97$, $a_2 = 0.8$, $b_1 = 2.2455$, $b_2 = 3.45$, $k_2 = 1.25$, $k_3 = 1.29$, $c_3 = 2$, and α is the aspect ratio of the ellipsoidal inclusions. At the disaggregation threshold found as $\varphi = c_1$ the partially molten material loses its cohesiveness and both viscosities approach zero. For a melt network consisting of 50% tubes and 50% films the following approximate equations have been derived from the model of Schmeling et al. (2012)

$$\eta_s = \eta_{s0} \cdot \left(1 - \frac{\varphi}{\varphi_{max}}\right)^k \quad (4.26)$$

$$\eta_b = \eta_{s0} a_2 \left(\frac{\varphi_{max} - \varphi}{\varphi}\right)^{b_2} \quad (4.27)$$

The parameters needed to calculate these viscosities for different aspect ratios between 0.2 and 0.5 are given in Tab. 4.1. k is given by $k = a_1\varphi + b_1$. Figure 4.1 shows the effective shear and bulk viscosities for different aspect ratios together with the simplified previous laws (Eqs. (4.1) and (4.2)). Takei and Holtzman (2009) and Rudge (2018) suggest that in the presence of an infinitesimal amount of connected melt the effective viscosity undergoes a finite drop of the order of a few 10% of the intrinsic matrix viscosity. In our approach we always have a finite melt porosity, thus we may identify the zero porosity viscosity η_{s0} in our formulation with the initially weakened value of Takei and Holtzman (2009) or Rudge (2018).

4.2.3 Methods and Model Setup

For the model we use a square box (1×1), which is initially partially molten to a certain degree, the background porosity. We place an initial porosity anomaly with

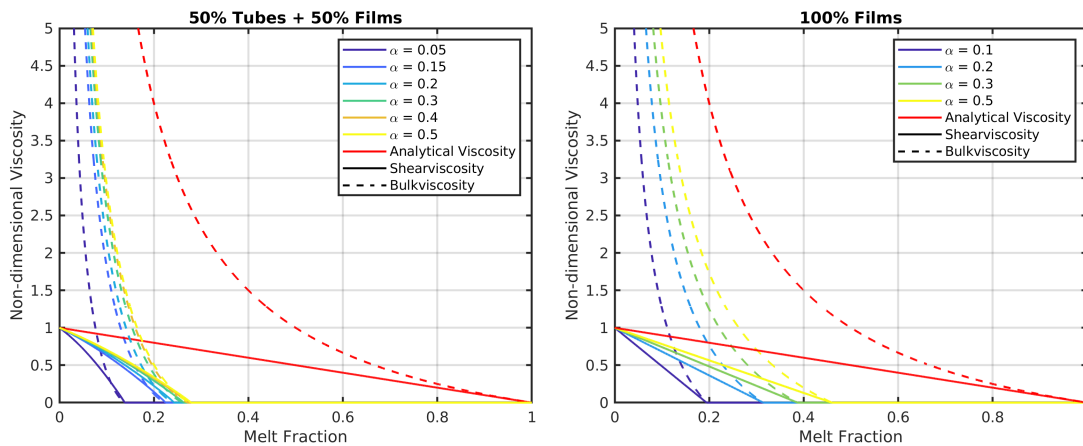


Figure 4.1: Shear (solid) and bulk (dashed) viscosity for several aspect ratios as a function of the melt fraction. Left: The viscosities are calculated for a melt network consisting of 50% tubes and 50% films. Right: The network consists of 100% films. The red lines show the simplified analytical viscosities (Eqs. (4.26) and (4.27)).

a higher porosity centered at $x_0 = 0.5$ and $z_0 = 0.2$ from which a porosity wave will develop. As the shape and width of a solitary wave with a certain rheology law and amplitude is not known a priori we use a Gaussian wave of the form

$$\varphi = A \cdot \exp \left[\left(\frac{x - x_0}{w} \right)^2 - \left(\frac{z - z_0}{w} \right)^2 \right] \quad (4.28)$$

for the perturbation and vary the initial width w of the wave. At the sides of the box symmetric boundaries and at the top and the bottom free slip boundaries are used. The in- and outflow velocities of matrix and melt at the top and bottom are prescribed in terms of the analytical solution of the background porosity.

The influence of the boundaries on the ascending wave was investigated and found to be fairly small. In Fig. 4.3 one can see the effect of the upper boundary on the phase velocity. At the end, as the waves approach the upper boundary, the dispersion curves slightly deviate from the supposed line. This error is smaller than 0.5% as long as the distance of the center of the wave to the upper boundary is greater than 1.5 times its 10%-radius. This radius is defined as the radius at which the porosity has decreased to 10% of the amplitude of the wave. For the side boundaries this distance has to be larger. For distances greater than 3 times the 10%-radius this error is smaller than 1%. In our models the waves have distances of 7–10 times the 10%-radius which corresponds to errors between 0.2 and 0.05%.

The equations are solved on a 201×201 grid by Finite Differences using the code FD-CON (e.g. Schmeling et al., 2019). Resolution tests have been made with grids varying from 101×101 to 401×401 . They show that after a short transient time the phase velocity and amplitude of the evolved porosity wave approach constant values for very high resolutions for all viscosity laws used. The subsequently observed slow variations of the phase velocity and amplitude of the wave along a quasi-steady state dispersion curve can be attributed to numerical diffusion at finite grid resolution. The resolution

test shows that 1) the quasi-steady state phase velocity and amplitude of the wave are of error order 1, and 2) the dispersion curves obtained on a 201×201 grid overestimate the extrapolated phase velocity values by about 10%. Time step resolution tests show that the long-term temporal behavior of the porosity waves is significantly improved if the time steps are chosen smaller than approximately 0.2 times the Courant criterion. The amplitude and phase velocity of the evolving porosity wave is obtained at every time step by quadratic interpolation of the porosity values on the FD grid and determining the value and velocity of the position of the maximum of the quadratic function. The resulting phase velocity shows small oscillations in time, which are probably due to the interaction of the 1st order error in time when solving Eqs. (4.3) and (4.4) and the 2nd order error of the interpolation. These oscillations are smoothed by applying a moving average including 50 neighboring points. The resulting time series of porosity amplitude and phase velocity can be plotted as a curve with time as curve parameter in an amplitude–phase velocity plot. This curve can be understood as a dispersion curve because the phase velocity depends on amplitude and thus implicitly on the width or wavelength of the porosity wave.

For the model series presented below the width and the amplitude of the initial wave, the background porosity and the rheology law have been varied. All models were carried out using $n = 2$ and $n = 3$ in the permeability–porosity law.

4.3 Results

4.3.1 Dispersion Curves for varied Widths and Amplitudes

As the shape of a two-dimensional porosity wave for a certain wave amplitude is not known, the initial width is varied. In Fig. 4.2a we show a porosity wave of amplitude 8 initially positioned at $x = 0.5$ and $z = 0.2$ (left) as it rises through the model box. In Fig. 4.2b a horizontal cross section through the maximum of an initial wave and the resulting solitary wave at a late stage is shown. During the early stage the wave gains some amplitude as the volume of an equivalent solitary wave with the same amplitude would be smaller for this example. Then the amplitude of the ascending wave slowly decreases again due to numerical diffusion and the evolving phase velocity – amplitude curve describes the quasi-steady state dispersion relation. At this point the wave is expected to be a solitary wave. The shape of this wave resembles a Gaussian bell curve quite well but does not fit exactly. The upper part of the wave in this example fits very well while the lower part is slightly wider.

To analyze the evolution of the ascending solitary wave the phase velocity and the amplitude is tracked over the full rising time and plotted into a dispersion diagram. In Fig. 4.3 the dispersion curves of a model with a starting wave width which is initially larger than the resulting solitary wave, a model with a similar width, and a model with a smaller initial width are shown. The curves start with high velocities for the Gaussian bell shaped wave and then rapidly slow down until they approach a specific point visible as a sharp kink from which they slowly follow a line. For the bigger and optimal width models, after this kink the wave is expected to have reached the solitary wave stage. For the bigger initial width this stage is reached at a higher amplitude than

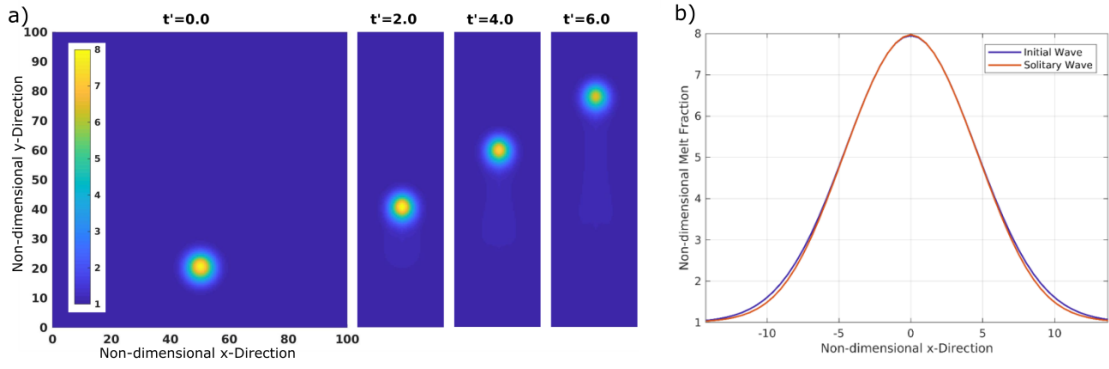


Figure 4.2: a) Non-dimensional melt fraction at 4 different time steps during the ascent of a solitary wave with an initial amplitude of 8. The model was carried out for a melt network geometry consisting of 100% films and an aspect ratio of 0.1. The background porosity is 0.005 and $n = 3$. b) Horizontal cross section through the center of the initial wave and the solitary wave at a later time.

initially assumed. It is important to note that, independent of the initial wave width, after reaching a solitary wave stage the velocities and shapes of waves of a certain amplitude are always equal, i.e. the three curves merge on one dispersion curve. For comparison with semi-analytic 2-D solitary porosity wave solutions the dashed curves in Fig. 3 and later Figures show dispersion curves with different power law n of the permeability-porosity relation and different bulk viscosity laws with $m = 0$ assuming a constant bulk viscosity, and $m = 1$ for a $1/\varphi$ proportionality (c.f. Eq. (4.2)) (Simpson and Spiegelman, 2011). In contrast to our models these solutions a) use a stiff rheology ("analytic viscosity" in Fig. 4.1), b) neglect solid shear (first term of the right hand side of Eq. (4.8)) which is responsible for \vec{v}_1 (c.f. Eq. (4.12)) in the matrix momentum equation, and for an important contribution in the separation flow (Eq. (4.11)), and c) apply the small porosity limit.

Based on this result one can carry out many models with different initial wave widths and different initial amplitudes and get one empirical steady state solitary wave dispersion curve for one viscosity law for a wide range of amplitudes.

Fig. 4.4 shows the time-dependent dispersion curves of models with 4 different initial amplitudes (4 to 10), and 11 different initial widths each. Depending on the initial widths they either gain amplitudes as they approach the solitary wave stage or they monotonously lose amplitude. Depending on the initial amplitude and width each case is characterized by a certain total melt volume, corresponding to a specific steady state solitary wave with a specific amplitude. Therefore the 44 models finally reach one steady state solitary wave dispersion curve at different amplitudes. As discussed in section 2, the amplitude of the waves slowly continue to decrease due to some small amount of numerical diffusion. Yet, they continue following the steady state solitary wave dispersion curve.

Although we use a different rheology law and do not apply the simplifications mentioned above, the steady state dispersion curve of our model is in general agreement with the $n = 3$, $m = 1$ dispersion curve determined semi-analytically by Simpson

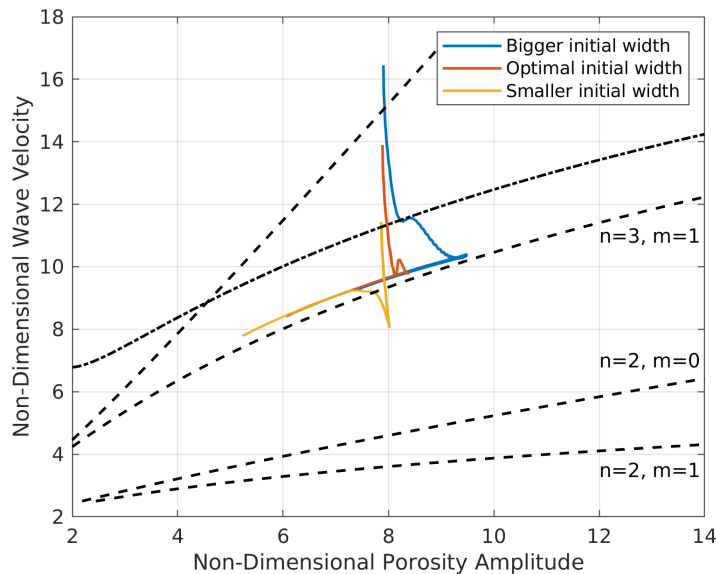


Figure 4.3: Dispersion curves for three models with an initial width bigger, smaller and approximately equal to the resulting solitary wave. Each model was carried out for a melt network geometry consisting of 100% films and an aspect ratio of 0.1. The background porosity is 0.005 and $n = 3$.

and Spiegelman (2011) (Fig. 4.4, dashed curve). However, given the 10% numerical overestimation of phase velocities of our models (c.f. Sec. 4.2.2), for high amplitudes our dispersion curve shows a significantly smaller slope and correspondingly smaller phase velocities than the semi-analytical curve by Simpson and Spiegelman (2011). Comparison of the simplified semi-analytical 1-D solution of Simpson and Spiegelman (2011) with the full analytical 1-D solution of Yarushina et al. (2015) shows that for low porosities these solutions fit very well together. For higher porosities the full solution becomes slower than the simplified one. Tentatively transferring this result to 2D our decrease in the slope can probably be explained by the low porosity limitation of the Simpson and Spiegelman (2011) solution which overestimates the velocity at high porosities.

4.3.2 Effect of different Viscosity Laws for $n=2$ and 3 on Dispersion Curves

To investigate the effect of different viscosity laws, two melt network geometries are chosen. The first one consists of 50% films/ellipsoidal melt pockets and 50% tubes, the second of 100% films/ellipsoidal melt pockets. Furthermore the aspect ratio α is varied, whereby a higher aspect ratio corresponds to compact melt pockets and leads to stronger viscosities and to a higher disaggregation threshold (c.f. Fig. 4.1).

Waves with these different viscosity laws give only minor differences in the dispersion curves (Fig. 4.5a, b). Especially with the films and tubes case the curves for different aspect ratios (Fig. 4.5a) are not distinguishable, both during the transient and final

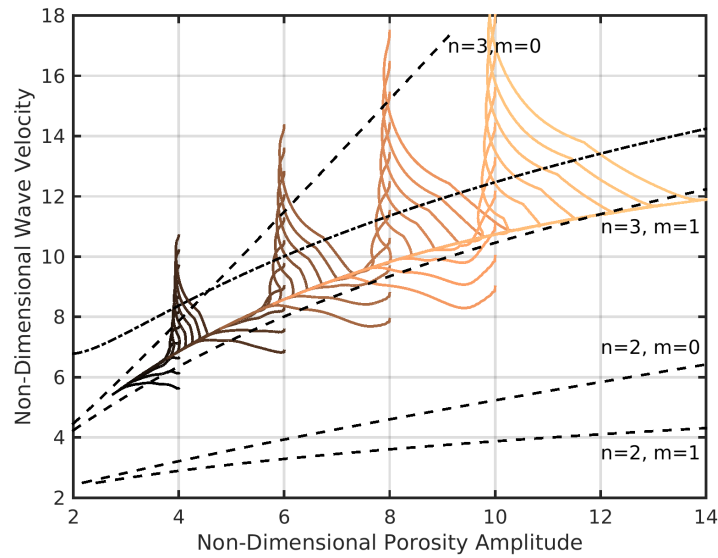


Figure 4.4: Dispersion curves for 44 models with 4 different initial amplitudes (4 to 10) and 11 different initial widths each. All models were carried out for a melt network geometry consisting of 100% films and an aspect ratio of 0.1. The background porosity is 0.005 and $n = 3$.

stage. In contrast, the analytical viscosity case (Eq. (4.1) and (4.2)) propagates along a different path and converges to a 4–6% higher final phase velocity curve. With 100% Films the differences among curves with the different viscosity laws in the final velocity are higher and lie in the order of 6%. These differences are surprisingly small if compared to the actual differences in effective shear viscosities of about 13% and bulk viscosity of about a factor 4 (at 4% melt corresponding to a porosity amplitude 8). It is also to be noted that the steady state part of our dispersion curve calculated with the analytical viscosity (Eq. (4.1) and (4.2)) excellently agrees with the semi-analytical solution (dashed) by Simpson and Spiegelman (2011) for the same viscosity law, if we account for the 10% numerical overestimation of our model phase velocity (c.f. section 4.2.2). Thus, their neglect of shear stresses and other simplifications have only a very minor effect compared to the effect of different viscosity laws. The overall effect of weakening of matrix viscosity due to decreasing aspect ratio is to slow down the phase velocity slightly.

Changing n of the permeability-porosity relation to 2 decreases the wave velocities significantly (Fig.4.5c, d). This drop is consistent with the simplified semi-analytical solitary wave solutions ($n = 2$, $m = 1$, dashed curves). In contrast to the $n = 3$ cases, the $n = 2$ velocities are above the Simpson and Spiegelman (2011) solutions even if the numerical 10% overestimation is considered. As for the $n = 3$ case, porosity waves with the stronger analytical viscosity case (Eq. (4.1) and Eq. (4.2)) are slightly faster than the new weaker viscosity cases.

While the ascending phase velocity of the wave is only slightly affected by the different viscosity laws, the width of the wave changes more strongly. In Figure 4.6 the half-widths of the solitary waves of amplitude of 8 are plotted against the corresponding

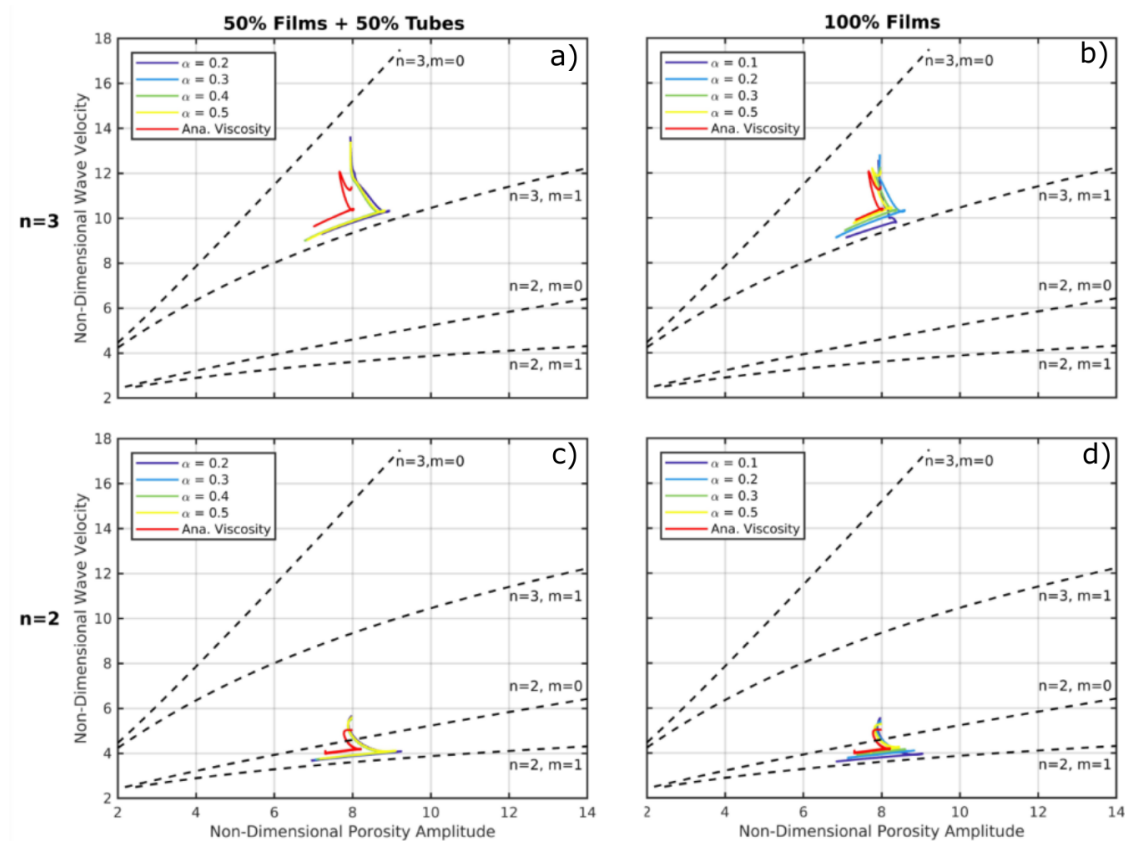


Figure 4.5: Dispersion curves of solitary waves with a) $n = 3$, films & tubes, b) $n = 3$, films, c) $n = 2$, films & tubes, d) $n = 2$, films for different aspect ratios.

wave velocities for the different viscosity laws. For $n = 2$ (Fig. 4.6a) and 100% films the wave gets wider for higher aspect ratios, while for the mixed geometry the widths stay more or less constant. The velocity increases only slightly with the aspect ratio. For $n = 3$ (Fig. 4.6b) and 100% films the width increases with aspect ratio but in contrast to $n = 2$ the phase velocity decreases with increasing aspect ratio. For the mixed geometry the velocity and half-width variations are minor again. These results show that as long as melt tubes represent a significant portion of the total melt volume (here 50%) they control the porosity wave dynamics and keep the porosity wave properties rather fixed. Only in the absence of tubes compact melt pockets with large aspect ratios significantly broaden the waves. For the stiff case of analytical viscosity (Eqs. (4.1) and (4.2)) the half width of the wave is comparable to the weaker 0.2 films, but the velocities are larger (Fig. 4.6a,b, light brown symbols).

Another interesting phenomenon to observe is the matrix velocity in the center of the wave, which increases for all geometries with aspect ratio (Fig. 4.7). While for 100% films this increase is stronger, for both geometries the velocities are approximately equal at an aspect ratio between 0.2 and 0.3. For $n = 2$ (Fig. 4.7a) the matrix velocities are always positive, meaning that despite a slow negative background velocity of the matrix, it rises in the center of the wave (together with the melt). Interestingly, for $n = 3$ (Fig. 4.7b) and small aspect ratios (0.1 and 0.2, i.e. weaker effective matrix

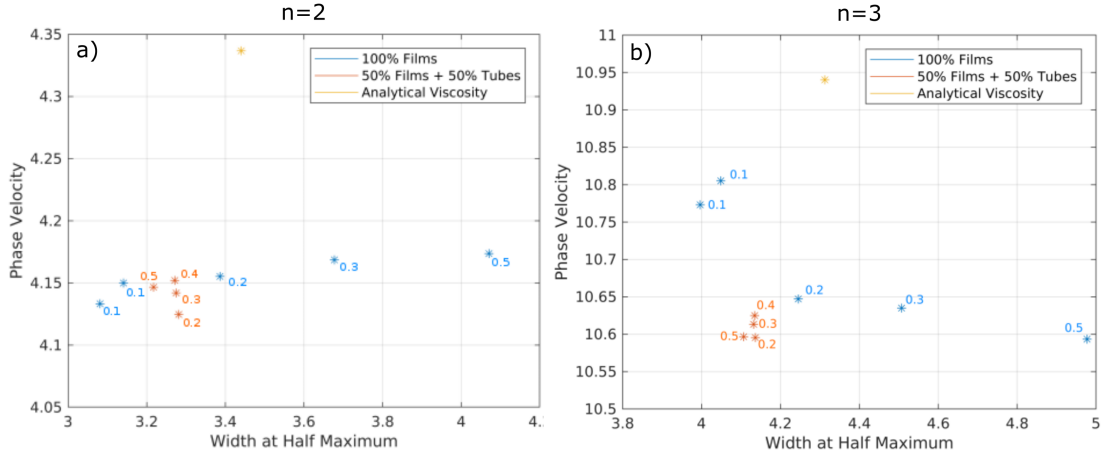


Figure 4.6: Non-dimensional half-width, plotted against non-dimensional phase velocity for a porosity wave of amplitude 8 for different viscosity laws. The numbers give the aspect ratios of the films/melt pockets. The background porosity is 0.5%. a) Permeability-porosity exponent $n = 2$, b) $n = 3$

viscosities) the direction of flow of the matrix is changed and matrix in the center flows downwards, i.e. against the direction of melt flow. Assuming constant matrix shear and bulk viscosities, Scott (1988) observed a similar switch from negative to positive matrix velocities in the center of a 2D solitary wave when the ratio of the bulk to shear viscosity was increased from 1 to 9 for $n = 3$. We see this switch around $\alpha = 0.25$ corresponding to a bulk to shear viscosity at the center of the porosity wave of about 16, and higher elsewhere. Such a switch can be explained by an increasing role of diapiric flow, which is \vec{v}_1 -related, incompressible, and upward in the center of the wave, with respect to the compaction flow, which is \vec{v}_2 -related, irrotational, and downward in the center of the wave (c.f. Eq. (4.12)). Weakening of the bulk viscosity within the porosity wave relative to the shear viscosity allows stronger decompaction and compaction rates which amplify the downward compaction flow with respect to the upward diapiric flow.

In the previous models the scaling background porosity of 0.005 and maximum wave amplitudes of 10 to 12 imply maximum melt fractions of 5 to 6%. Thus, the matrix shear viscosity decrease was only small, of order 10% for e.g. the aspect ratio 0.1 models and of order 5% for the stiffer analytical viscosity laws (Eqs. (4.1) and (4.2)). This explains the rather mild rheology effect when comparing the effect of the different viscosity laws. With the aim to reach higher maximum melt fractions associated with stronger rheological effects we carried out a model series with increased background porosities, both applying the analytical viscosity law ($m = 1$) and our weaker matrix viscosities with 100% films with an aspect ratio 0.1 (Fig. 4.8). The increase in the background porosity from 0.5% to 1.5% has only a minor influence on the behavior of the solitary wave for models which use the analytical viscosity law ($m = 1$): The half width of the wave is almost completely unaffected (by $\sim 1\%$), while the phase velocity is increased by only approximately 2.5%. Using a viscosity law based on a melt geometry consisting of 100% films and an aspect ratio of 0.1 the differences

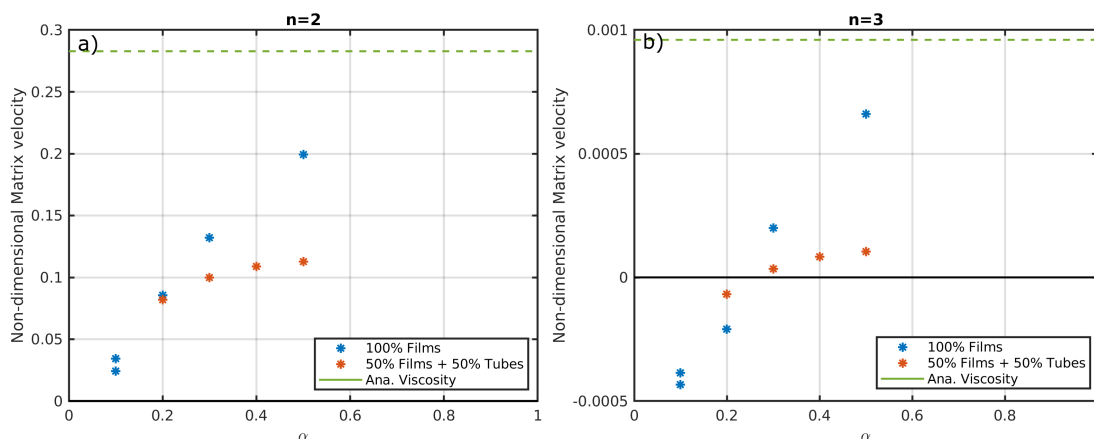


Figure 4.7: Matrix velocity in the center of a wave with an amplitude of 8 as a function of the aspect ratio of the films for a) $n = 2$, b) $n = 3$. The background porosity for all models was 0.005.

become significant. The half width decreases to $\sim 70\%$ of its initial value and the phase velocity decreases by up to 20% with increasing background porosity, i.e. with an increased maximum porosity within the wave. Thus, the half widths and phase velocities show a significant difference to the analytical viscosity law (Fig. 4.8). In fact, the phase velocities show the opposite behavior to the analytical viscosity law (see Fig. 4.8b). These models suggest that the high melt fractions within the waves which are associated with a significant local matrix weakening, both for shear and bulk viscosity, lead to effectively shortened compaction lengths within the wave, i.e. to a narrowing and focusing of the wave. Such narrower waves contain less melt than broader waves of same amplitude, i.e. less buoyancy, which slows down the rising phase velocity.

4.4 Discussion

It is interesting to note that although the semi-analytic solutions of Simpson and Spiegelman (2011) neglect the shear term in the matrix momentum equation and in the separation flow equation they are in good agreement with the low φ_0 models which include this term. To understand this we made a test with a model with 100% films and aspect ratio 0.1 and found that in the separation flow Eq. (4.11) the shear term has a significant amplitude of about 50% compared to the compaction term. We then switched off this term in the separation flow Eq. (4.11), which is equivalent to assuming zero shear viscosity. Surprisingly it turned out that separation velocity changed only insignificantly while the amplitudes of matrix divergence and convergence increases by about 25%, and the compaction related term driving the separation velocity in Eq. (4.11) increases by about 50%, i.e. by the same amount the shear term had before. Obviously, the buoyancy forces of the solitary wave are partitioned between the decompaction pressure controlled by the bulk viscosity and the shear stresses, namely

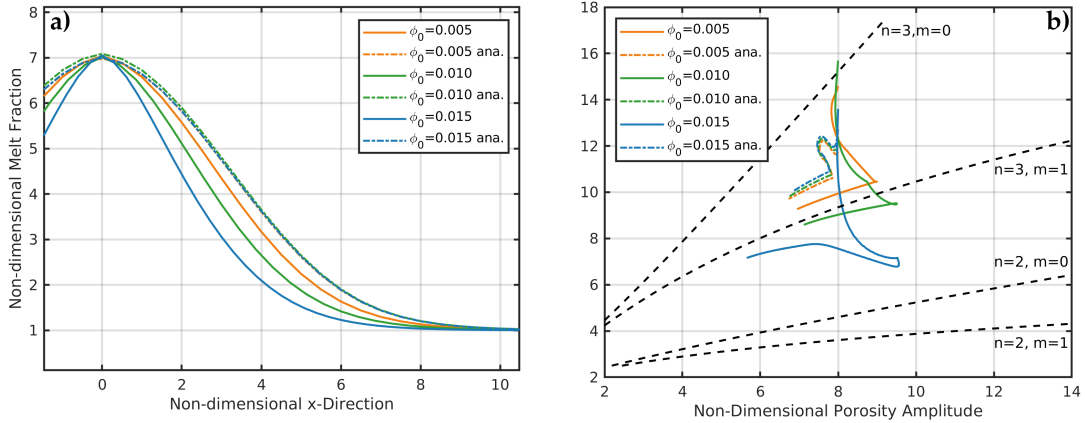


Figure 4.8: a) Horizontal profiles through ascending waves and b) dispersion curves with different background porosities but the same non-dimensional amplitude of 7. The dot-dashed curves were calculated with the simplified analytical viscosity law ($m=1$). The solid lines were calculated with a viscosity law based on 100% films and an aspect ratio of 0.1.

the vertical normal shear stresses. If these stresses are neglected by assuming a zero shear viscosity, the buoyancy forces are balanced by the compaction pressure alone, and the shear contribution of the downward segregation flow is taken over by the increased compaction contribution.

Recently, Rudge (2018) developed a diffusion creep model based on microscopic diffusion calculations in the presence of melt in textural equilibrium with truncated octahedrons. Assuming infinite diffusivity in the melt phase he obtains a somewhat stronger weakening of the shear viscosity at smaller melt fractions than in our model, but comparable disaggregation porosities as in Fig. 4.1. However, due to the infinite diffusivity assumption, the bulk viscosity remains finite ($= 5/3$ of the effective shear viscosity) even at very small melt porosities, while in our model it increases infinitely in the limit of zero porosity. We expect that our results with increased weakening effect (φ_0 increased to 1.5%) might be applicable also to the rheology based on Rudge's (2018) analyses.

It should be noted that in our study the viscosity law has been varied by assuming various melt geometries of melt films and films/melt pockets superimposed with tubes, while the permeability-porosity has been varied independently between $n = 2$ corresponding to the ideal case of only interconnected tubes and $n = 3$ corresponding to the ideal case of interconnected thin films. Three-dimensional melt distributions of partially molten mantle rocks have been studied e.g. by serial sectioning (Garapic et al., 2013) identifying a network of melt tubes and films, and by microtomography (Zhu et al., 2011) suggesting the predominance of melt tubes along grain edges. Yet, at higher melt fractions the latter distributions are characterized by tapered edges of the melt tubes partly or completely wetting grain faces between adjacent grains. From the latter experiments Miller et al. (2014) determined the permeability by 3D-fluid flow modeling and found an exponent of 2.6. Thus, our simplified melt viscosities

and permeabilities cover quite well observed partially molten olivine-basalt systems in textural equilibrium.

In Richard et al. (2012) it was observed that with increasing background porosities the waves will widen and the phase velocities will slow down. In our models we observe faster velocities with increasing background porosity if the analytical viscosity is used. This can be explained by the different scaling which was used by Richard et al. (2012). They used just the shear viscosity to calculate the compaction length and not the sum of shear and bulk viscosity. If the same scaling is used, we get the same behavior for the phase velocity. In contrast to Richard et al. (2012) we observe a narrowing effect of the waves for larger background porosities, which cannot be explained by scaling. As Richard et al. (2012) used a 1-D model, we suspect that 2-D effects such as including the incompressible flow velocity, \vec{v}_1 , are responsible for the different shapes of the wave at different background porosities.

4.5 Conclusion

As the shape of a solitary wave in our models cannot be described analytically, we start with a Gaussian wave, which develops quite rapidly into a solitary wave with a similar shape and a certain amplitude, depending on the initial width of the wave.

Even though the rheologies used are much weaker than the simplified analytical ones the effect on dispersion curves and wave shape are only moderate as long as the shear viscosity does not drop below about 80% of the intrinsic shear viscosity. This value corresponds to a melt fraction of 5%, equivalent to 20% of the disaggregation value. At this porosity the bulk viscosity is approximately 5–7 times the intrinsic shear viscosity. In this case the phase velocity changes just slightly for all cases, while the waves broaden in the absence of tubes with increasing aspect ratio.

In contrast, for higher melt fractions of about 12%, equivalent to 50% of the disaggregation values, the shear viscosity decreases to 50% of the intrinsic viscosity, and the bulk viscosity is of the order of the intrinsic shear viscosity. Then, our models predict significant narrowing of the porosity waves and slowing down of the phase velocities. For such conditions a strong discrepancy in solitary wave behavior between our viscosity law and the analytical ones is found.

For low melt fractions our models are in good agreement with semi-analytic solutions which neglect the shear stress term, because the matrix shear contribution of the downward segregation flow is taken over by the increase of the compaction contribution.

Acknowledgement

We would like to thank the reviewers Guillaume Richard and Viktoriya Yarushina for their detailed and thoughtful reviews, which helped to improve the manuscript.

References

- Bercovici, D., Ricard, Y., and Schubert, G. (2001). A two-phase model for compaction and damage: 1. General Theory. *Journal of Geophysical Research*, 106(B5):8887.
- Garapic, G., Faul, U. H., and Brisson, E. (2013). High-resolution imaging of the melt distribution in partially molten upper mantle rocks: Evidence for wetted two-grain boundaries. *Geochemistry, Geophysics, Geosystems*, 14(3):556–566.
- McKenzie, D. (1984). The generation and compaction of partially molten rock. *Journal of Petrology*, 25(3):713–765.
- Miller, K. J., lu Zhu, W., Montési, L. G., and Gaetani, G. A. (2014). Experimental quantification of permeability of partially molten mantle rock. *Earth and Planetary Science Letters*, 388:273–282.
- Omlin, S., Räss, L., and Podladchikov, Y. Y. (2018). Simulation of three-dimensional viscoelastic deformation coupled to porous fluid flow. *Tectonophysics*, 746(August 2017):695–701.
- Räss, L., Yarushina, V. M., Simon, N. S., and Podladchikov, Y. Y. (2014). Chimneys, channels, pathway flow or water conducting features - An explanation from numerical modelling and implications for CO₂ storage. *Energy Procedia*, 63:3761–3774.
- Richard, G. C., Kanjilal, S., and Schmeling, H. (2012). Solitary-waves in geophysical two-phase viscous media: A semi-analytical solution. *Physics of the Earth and Planetary Interiors*, 198-199:61–66.
- Richardson, C. N. (1998). Melt flow in a variable viscosity matrix. *Geophysical Research Letters*, 25(7):1099–1102.
- Rudge, J. F. (2018). The Viscosities of Partially Molten Materials Undergoing Diffusion Creep. *Journal of Geophysical Research : Solid Earth*, pages 534–562.
- Schmeling, H. (2000). *Partial melting and melt segregation in a convecting mantle*. Springer.
- Schmeling, H., Kruse, J. P., and Richard, G. C. (2012). Effective shear and bulk viscosity of partially molten rock based on elastic moduli theory of a fluid filled poroelastic medium. *Geophysical Journal International*, 190(3):1571–1578.
- Schmeling, H., Marquart, G., Weinberg, R., and Wallner, H. (2019). Modelling melting and melt segregation by two-phase flow: New insights into the dynamics of magmatic systems in the continental crust. *Geophysical Journal International*, 217(1):422–450.
- Scott, D. R. (1988). The competition between percolation and circulation in a deformable porous medium. *Journal of Geophysical Research*, 93(B6):6451–6462.
- Scott, D. R. and Stevenson, D. J. (1984). Magma solitons. *Geophysical Research Letters*, 11(11):1161–1164.

- Simpson, G. and Spiegelman, M. (2011). Solitary wave benchmarks in magma dynamics. *Journal of Scientific Computing*, 49(3):268–290.
- Spiegelman, M. (1993). Flow in deformable porous media. Part 2 Numerical analysis - the relationship between shock waves and solitary waves. *J. Fluid Mech.*, 247:39–63.
- Spiegelman, M. and McKenzie, D. (1987). Simple 2-D models for melt extraction at mid-ocean ridges and island arcs. *Earth and Planetary Science Letters*, 83(1-4):137–152.
- Sramek, O., Ricard, Y., and Bercovici, D. (2007). Simultaneous melting and compaction in deformable two-phase media. *Geophysical Journal International*, 168(3):964–982.
- Stevenson, D. J. (1989). Spontaneous small-scale melt segregation in partial melts undergoing deformation. *Geophysical Research Letters*, 16(9):1067–1070.
- Takei, Y. and Holtzman, B. K. (2009). Viscous constitutive relations of solid-liquid composites in terms of grain boundary contiguity: 1. Grain boundary diffusion control model. *Journal of Geophysical Research: Solid Earth*, 114(6):1–18.
- Wiggins, C. and Spiegelman, M. (1995). Magma migration and magmatic solitary waves in 3D. *Geophysical Research Letters*, 22(10):1289–1292.
- Yarushina, V. M., Podladchikov, Y. Y., and Connolly, J. A. (2015). (De)compaction of porous viscoelastoplastic media: Solitary porosity waves. *Journal of Geophysical Research : Solid Earth*, pages 1–20.
- Zhu, W., Gaetani, G. A., Fusses, F., Montési, L. G., and De Carlo, F. (2011). Microtomography of partially molten rocks: Three-dimensional melt distribution in mantle peridotite. *Science*, 332(6025):88–91.

Chapter 5

Publication 2

Magma ascent mechanisms in the transition regime from solitary porosity waves to diapirism

Solid Earth **12**:1549-1561 (2021)

Janik Dohmen¹ & Harro Schmeling¹

¹Institute for Geoscience, Goethe University Frankfurt, Frankfurt, Germany

Abstract

In partially molten regions inside the Earth melt buoyancy may trigger upwelling of both solid and fluid phases, i.e. diapirism. If the melt is allowed to move separately with respect to the matrix, melt perturbations may evolve into solitary porosity waves. While diapirs may form on a wide range of scales, porosity waves are restricted to sizes of a few times the compaction length. Thus, the size of a partially molten perturbation in terms of compaction length controls whether material is dominantly transported by porosity waves or by diapirism. We study the transition from diapiric rise to solitary porosity waves by solving the two-phase flow equations of conservation of mass and momentum in 2D with porosity dependent matrix viscosity. We systematically vary the initial size of a porosity perturbation from 1.8 to 48 times the compaction length. If the perturbation is of the order of a few compaction lengths, a single solitary wave will emerge, either with a positive or negative vertical matrix flux. If melt is not allowed to move separately to the matrix a diapir will emerge. In between these end members we observe a regime where the partially molten perturbation will split up into numerous solitary waves, whose phase velocity is so low compared to the Stokes velocity that the whole swarm of waves will ascend jointly as a diapir, just slowly elongating due to a higher amplitude main solitary wave.

Only if the melt is not allowed to move separately to the matrix no solitary waves will build up, but as soon as two-phase flow is enabled solitary waves will eventually emerge. The required time to build them up increases non-linearly with the perturbation radius in terms of compaction length and might be for many cases too long to allow for them in nature.

5.1 Introduction

In geodynamic settings such as mid-ocean ridges, hotspots, subduction zones or orogenic belts partial melts are generated within the asthenosphere or lower continental crust and ascend by fluid migration within deforming rocks (e.g. Sparks and Parmentier, 1991; Katz, 2008; Keller et al., 2017; Schmeling et al., 2019). Inherent tectonic or rock heterogeneities in such systems may result in spatially varying melt fractions on length scales varying over several orders of magnitudes. These length scales play an important role in determining whether melt anomalies may rise as porous waves (Jordan et al., 2018) or by other mechanisms such as diapirs (Rabinowicz et al., 1987), focused channel networks (Spiegelman et al., 2001) or dykes (Rivalta et al., 2015). Here we focus on the effect of the length scale on the formation and evolution of buoyancy driven porous waves or diapirs.

The physics of fluid moving relatively to a viscously deformable porous matrix were firstly described by McKenzie (1984) and it was later shown by several authors that these equations allow for the emergence of solitary porosity waves (Scott and Stevenson (1984); Barcilon and Lovera (1989); Wiggins and Spiegelman (1995)). Porosity waves are regions of localized excess fluid that ascend with permanent shape and constant velocity, controlled by compaction and decompaction of the surrounding matrix. They have extensively been studied as mechanisms transporting geochemical signatures or magma through the asthenosphere, lower and middle crust (e.g. Watson and Spiegelman, 1994; McKenzie, 1984; Connolly, 1997; Connolly and Podladchikov, 2013; Jordan et al., 2018; Richard et al., 2012). It has been shown that the dynamics of porous waves strongly depends on the porosity dependence of the matrix rheology (e.g. Connolly and Podladchikov, 1998; Yarushina et al., 2015; Connolly and Podladchikov, 2015; Omlin et al., 2017; Dohmen et al., 2019). Yet, one open question is how the length scale of solitary porosity waves relates to an arbitrary length scale of a possible porosity anomaly in given geodynamic settings.

The size of a solitary porosity wave is usually of the order of a few compaction lengths (McKenzie, 1984; Scott and Stevenson, 1984; Simpson and Spiegelman, 2011), but this length scale varies over a few orders of magnitude, depending on the shear and bulk viscosity of the matrix, fluid viscosity and permeability (see Eq. (5.20)) with typical values of 100-10000 meters (McKenzie, 1984; Spiegelman, 1993). However, partially molten regions in the lower crust or upper mantle are prone to gravitational instabilities such as Rayleigh-Taylor instabilities or diapirism (e.g. Griffiths, 1986; Bittner and Schmeling, 1995; Schmeling et al., 2019). Originating from the Greek “*diapirein*”, i.e. “to pierce through”, diapirism describes the “buoyant upwelling of relatively light rock” (Turcotte and Schubert, 1984) through and into a denser overburden. In the general definition the rheology of the diapir and ambient material is not specified, both can be ductile as in our case. Buoyancy may be of compositional or phase related origin, e.g., due to the presence of non-segregating partial melt (Wilson, 1989). In this model we describe a diapir as a partially molten perturbation, whose rising velocity, characterizable by the Stokes velocity, is lower than the corresponding solitary waves phase velocity.

As characteristic wavelengths of Rayleigh-Taylor instabilities may be similar, but also

of significantly different order of those of porosity waves, and the Stokes velocity is strongly affected by the spatial expansion, the question arises how these two mechanisms interact and how does the transition from a porosity wave to a rising partially molten diapir look like. Scott (1988) already investigated a similar scenario. He calculated porosity waves changing the compaction length by altering the constant shear to bulk viscosity ratio. In contrast, we vary the radius of a partially molten perturbation in terms of compaction lengths but keeping the porosity dependent viscosity law the same. While Scott (1988) was not able to reach the single-phase flow endmember due to his setup, we can reach this endmember with our description and can explore the transition.

In this work we will address the question of length scale of a partially molten region with respect to the length scale of a solitary porosity wave, by varying the sizes of initial porosity perturbations. We further focus on the numerical implications on modeling magma transport.

5.2 Methods

5.2.1 Governing Equations

The formulation of the governing equations for the melt-in-solid two-phase flow dynamics is based on McKenzie (1984), Spiegelman and McKenzie (1987) and Schmelting (2000) assuming an infinite Prandtl number, a low fluid viscosity w.r.t. the effective matrix viscosity, zero surface tension, and the Boussinesq approximation. In the present formulation the Boussinesq approximation assumes the same constant density for the solid and fluid except for the buoyancy terms of the momentum equations for the solid and fluid. In the following all variables associated with the pore fluid (melt) have the subscript f and those associated with the solid matrix have the subscript s . The equation for the conservation of the mass of the melt is

$$\frac{\partial \varphi}{\partial t} + \vec{\nabla} \cdot (\varphi \vec{v}_f) = 0, \quad (5.1)$$

and the mass conservation of the solid is

$$\frac{\partial (1 - \varphi)}{\partial t} + \vec{\nabla} \cdot ((1 - \varphi) \vec{v}_s) = 0. \quad (5.2)$$

φ is the volumetric rock porosity (often called melt fraction), \vec{v}_f and \vec{v}_s are the fluid and solid velocities, respectively. The momentum equations are given as a generalized Darcy equation for the fluid separation flow

$$\vec{v}_f - \vec{v}_s = -\frac{k_\varphi}{\mu\varphi} \left(\vec{\nabla} P_f - \rho_f \vec{g} \right), \quad (5.3)$$

where ρ_f is the fluid density and P_f is the fluid pressure (including the lithostatic pressure), whose gradient is driving the fluid segregation by porous flow, μ is the melt dynamic viscosity and \vec{g} is the gravitational acceleration. k_φ is the permeability that depends on the rock porosity

$$k_\varphi = k_0 \varphi^n, \quad (5.4)$$

with n being the power-law exponent constant, usually equal to 2 or 3. This relation is known as the Kozeny-Carman relation (e.g. Costa, 2006). The Stokes equation for the mixture is given as

$$\bar{\rho}\vec{g} - \vec{\nabla}P_f + \vec{\nabla} \cdot \boldsymbol{\tau} = 0. \quad (5.5)$$

$\bar{\rho}$ is the density of the melt – solid mixture and $\boldsymbol{\tau}$ is the effective viscous stress tensor of the matrix including both shear and compaction components

$$\boldsymbol{\tau} = \eta \left(\frac{\partial v_{si}}{\partial x_j} + \frac{\partial v_{sj}}{\partial x_i} \right) + \left(\zeta - \frac{2}{3}\eta \right) \delta_{ij} \nabla \cdot \vec{v}_s. \quad (5.6)$$

ζ is the volume viscosity. The linearized equation of state for the mixture density is given as

$$\bar{\rho} = \rho_0 (1 - c_f \varphi) \quad (5.7)$$

with ρ_0 as the solid density and $c_f = \frac{\rho_0 - \rho_f}{\rho_0}$. The shear and volume viscosity are given by the equations

$$\eta = \eta_0 (1 - \varphi) \quad (5.8)$$

and

$$\zeta = \eta_0 \frac{1 - \varphi}{\varphi} \quad (5.9)$$

where η_0 is the constant intrinsic shear viscosity of the matrix. As in both equations (5.3) and (5.5) P_f is the fluid pressure (e.g. McKenzie, 1984, Appendix A), these equations can be merged to eliminate the pressure resulting in

$$\vec{v}_f - \vec{v}_s = -\frac{k_0 \varphi^{n-1}}{\mu} \left(\rho_0 c_f \vec{g} (1 - \varphi) + \vec{\nabla} \cdot \boldsymbol{\tau} \right). \quad (5.10)$$

This equation states that the fluid separation flow (i.e. melt segregation velocity) is driven by the buoyancy of the fluid with respect to the solid and the viscous stress in the matrix including compaction and decompaction. Following Sramek et al. (2012), the Stokes equation (5.3) can be rewritten by expressing the matrix velocity, \vec{v}_s , as the sum of the incompressible flow velocity, \vec{v}_1 , and the irrotational (compaction) flow velocity, \vec{v}_2 , as:

$$\vec{v}_s = \vec{v}_1 + \vec{v}_2 = \left(\frac{\partial \psi}{\partial z} \right) + \left(\frac{\partial \chi}{\partial x} \right) \quad (5.11)$$

with ψ as stream function and χ as the irrotational velocity potential, given as the solution of the Poisson equation

$$\vec{\nabla}^2 \chi = \vec{\nabla} \cdot \vec{v}_s. \quad (5.12)$$

The divergence term $\vec{\nabla} \cdot \vec{v}_s$ can be derived from Eqs. (5.1) and (5.2) to give

$$\vec{\nabla} \cdot \vec{v}_s = -\vec{\nabla} \cdot [\varphi (\vec{v}_f - \vec{v}_s)]. \quad (5.13)$$

In the small fluid viscosity limit the viscous stresses within the fluid phase are neglected, resulting in a viscous stress tensor in the Stokes equation of the mixture (Eq. (5.5)), in which only the stresses in the solid phase are relevant. This is evident

from the definition of the viscous stress tensor, which only contains matrix and not fluid viscosities. Melt viscosities of carbonatitic, basaltic or silicic wet or dry melts span a range from <1 Pa s to extreme values up to 10^{14} Pa s (see the discussion in Schmeling et al., 2019), while effective viscosities of mafic or silicic partially molten rocks may range between 10^{16} Pa s and 10^{20} Pa s, depending on melt fraction, stress, and composition. Thus, in most circumstances the small fluid viscosity limit is justified.

In the limit of this small viscosity assumption, inserting the above solid velocity (Eq. (5.11)) into the viscous stress (Eq. (5.6)), this into the Stokes equation ((5.5)), and taking the curl of the x- and z equations the pressure is eliminated and one gets

$$\left(\frac{\partial^2}{\partial x^2} - \frac{\partial^2}{\partial z^2}\right) \left[\eta \left(\frac{\partial^2 \psi}{\partial x^2} - \frac{\partial^2 \psi}{\partial z^2} \right) \right] + 4 \frac{\partial^2}{\partial x \partial z} \left[\eta \frac{\partial^2 \psi}{\partial x \partial z} \right] = -g \frac{\partial \rho}{\partial x} + A(\chi) \quad (5.14)$$

with

$$A(\chi) = -2 \frac{\partial^2}{\partial x \partial z} \left[\eta \left(\frac{\partial^2 \chi}{\partial x^2} - \frac{\partial^2 \chi}{\partial z^2} \right) \right] + 2 \left(\frac{\partial^2}{\partial x^2} - \frac{\partial^2}{\partial z^2} \right) \left[\eta \frac{\partial^2 \chi}{\partial x \partial z} \right] \quad (5.15)$$

To describe the transition from solitary waves to diapirs it is useful to non-dimensionalize the equations. As scaling quantities we use the radius r of the anomaly, the reference viscosity η_0 , and the scaling Stokes sphere velocity (e.g. Turcotte and Schubert, 1984) based on the maximum porosity of the anomaly φ_{max}

$$v_{St} = C_{st} \frac{\varphi_{max} \Delta \rho g r^2}{\eta_0} \quad (5.16)$$

resulting to the following non-dimensionalization where non-dimensional quantities are primed:

$$\begin{aligned} (x, z) &= (x', z') \cdot r & \vec{v}_{s,f} &= \vec{v}'_{s,f} \cdot v_{St} & t &= t' \cdot \frac{r}{v_{St}} \\ (\boldsymbol{\tau}, P) &= (\boldsymbol{\tau}', P') \cdot \frac{\eta_0 v_{St}}{r} & (\eta, \zeta) &= (\eta', \zeta') \cdot \eta_0 & (\psi, \chi) &= (\psi', \chi') \cdot r v_{St} \end{aligned} \quad (5.17)$$

For r the half width of the prescribed initial perturbation, consisting of a 2D Gaussian bell, is chosen. This is reasonable as the rising velocity in our code is best described by the Stokes velocity, using this radius. The exact shape of the perturbation is given later in the model setup.

C_{St} is calculated by using the analytic solution of an infinite Stokes cylinder within another cylinder (Popov and Sobolev (2008), based on the drag force derived by Slezkin (1955)), because, due to boundary effects, the cylinder gets effectively slowed. C_{St} is calculated using $C_{St} = \ln(k) - \frac{k^2-1}{k^2+1}$, where k is the ratio of outer cylinder's to inner cylinder's radius. For our model setup C_{St} is equal to 0.17.

With these rules the Darcy equation (5.10) is given in non-dimensional form

$$\vec{v}'_f - \vec{v}'_s = -\frac{\delta_c^2}{r^2} \frac{1}{\tilde{\eta}' \varphi} \left(\vec{e}_z \frac{(1-\varphi)}{\varphi_{max}} + \vec{\nabla}' \cdot \boldsymbol{\tau}' \right) \quad (5.18)$$

where \vec{e}_z is the unit vector in z-direction and $\tilde{\eta}'$ is equal to $\zeta' + \frac{4}{3}\eta'$. The momentum equation of the mixture Eq. (5.12) is given by

$$\left(\frac{\partial^2}{\partial x'^2} - \frac{\partial^2}{\partial z'^2}\right) \left[\eta' \left(\frac{\partial^2 \psi'}{\partial x'^2} - \frac{\partial^2 \psi'}{\partial z'^2}\right)\right] + 4 \frac{\partial^2}{\partial x' \partial z'} \left[\eta' \frac{\partial^2 \psi'}{\partial x' \partial z'}\right] = \frac{1}{\varphi_{max}} \frac{\partial \varphi}{\partial x'} + A'(X'). \quad (5.19)$$

δ_c^2/r^2 in Eq. (5.18) is the squared ratio of compaction length δ_c to the system length scale r , which is the main parameter describing our system. The compaction length is a natural length scale emerging from the problem and of particular importance in our context, because 2D porosity waves have half width radii of the order of $3 \cdot \delta_c$ to $5 \cdot \delta_c$ (Simpson and Spiegelman, 2011). It is defined as:

$$\delta_c = \sqrt{\frac{\zeta + \frac{4}{3}\eta}{\mu} k_\varphi} \quad (5.20)$$

All quantities in the other equations are simply replaced by their non-dimensional primed equivalents (Eqs. (5.1), (5.2), (5.6), (5.11) to (5.13) and (5.15)).

We now compare the two limits, where segregation or two-phase flow dominates (solitary wave regime), and where fluid and solid rise together with the same velocity as partially molten bodies, which we identify with the diapir regime. We compare the characteristic segregation velocity within solitary waves, which scales as

$$v_{sgr} \approx \frac{k_0 \varphi_{max}^{n-1}}{\mu} \left(\Delta \rho g (1 - \varphi_{max}) - \vec{\nabla}' \cdot \boldsymbol{\tau} \right) = C_{sgr} \frac{k_0 \varphi_{max}^{n-1} \Delta \rho g (1 - \varphi_{max})}{\mu} \quad (5.21)$$

where C_{sgr} is of the order 1/2 for 2D solitary waves (Schmeling, 2000), with the characteristic Stokes sphere rising velocity given by Eq. (5.16). The ratio of these is given by

$$\frac{v_{sgr}}{v_{st}} = \frac{C_{sgr}}{C_{st}} \frac{\delta_{c0}^2}{r^2} \frac{\varphi_{max}^{n-2} (1 - \varphi_{max})}{\tilde{\eta}'_0 \varphi_0^n} \quad (5.22)$$

Here $\tilde{\eta}'_0$ refers to $\tilde{\eta}'$ for the background porosity φ_0 and δ_{c0} to the compaction length of the background porosity. In contrast to Scott (1988), who varies the volume viscosity in his model series, we vary the ratio of initial Stokes radius to compaction length.

Thus, in the solitary wave limit

$$\frac{C_{sgr}}{C_{st}} \frac{\delta_{c0}^2}{r^2} \frac{\varphi_{max}^{n-2} (1 - \varphi_{max})}{\tilde{\eta}'_0 \varphi_0^n} \gg 1 \quad (5.23)$$

Darcy's law Eq. (5.18) results in large segregation velocity, which scales as

$$v'_{sgr} = \frac{C_{sgr}}{C_{st}} \frac{\delta_{c0}^2}{r^2} \frac{\varphi_{max}^{n-2} (1 - \varphi_{max})}{\tilde{\eta}'_0 \varphi_0^n} \quad (5.24)$$

From Eq. (5.13) it follows that the irrotational part of the matrix velocity scales with

$$v_1 \approx -\varphi_{max} v_{sgr} \quad (5.25)$$

while the rotational part is given by Eq. (5.19): In that equation A' scales with χ' , which, via Eqs. (5.12) and (5.13), scale with v_{sgr} , i.e. with δ_{c0}^2/r^2 . In other words, the second term on the RHS of Eq. (5.19) dominates for small r^2/δ_{c0}^2 as the first term is of the order 1. Thus, the rotational matrix velocity has the same order as the irrotational compaction velocity and serves to accommodate the compaction flow. In this limit the buoyancy term in Eq. (5.19), $\frac{1}{\varphi_{max}} \frac{\partial \varphi}{\partial x'}$, is of vanishing importance for the matrix velocity and the matrix velocity, $\vec{v}_1 + \vec{v}_2$, is of the order of $\varphi_{max} v_{sgr}$. In the small porosity limit, matrix velocities are negligible with respect to fluid velocities. In the diapir limit,

$$\frac{C_{sgr}}{C_{st}} \frac{r^2}{\delta_c^2} \frac{\varphi_{max}^{n-2} (1 - \varphi_{max})}{\tilde{\eta}_0' \varphi_0^n} \ll 1 \quad (5.26)$$

and Eq. (5.18) predict vanishing segregation velocities. As A' and χ' scale with r^2/δ_{c0}^2 , both vanish in the diapir limit, no irrotational matrix velocity occurs and Eq. (5.19) reduces to the classical biharmonic equation (i.e. Stokes equation) driven by melt buoyancy and describing classical diapiric ascent. Segregation velocities are negligible with respect to matrix velocities.

In Fig. 5.1 the results of this simple analysis are shown, where we calculated the velocity

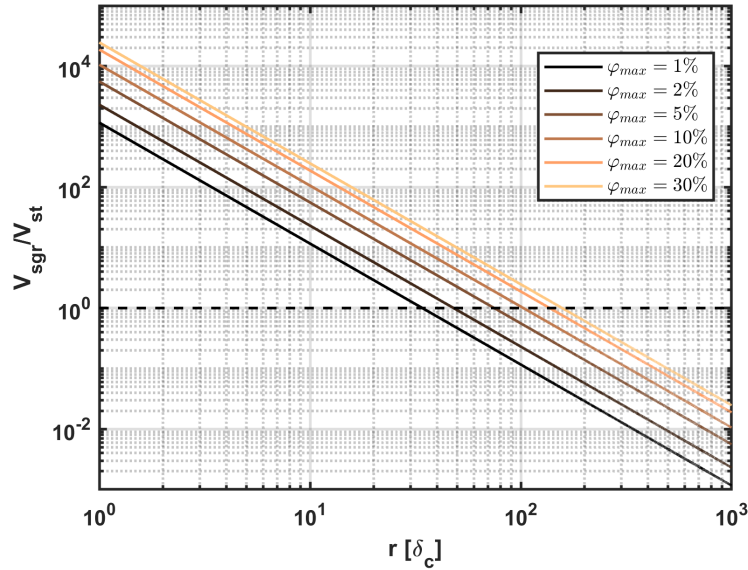


Figure 5.1: The segregation to Stokes velocity ratio, following Eq. (5.22), is given as a function of initial perturbation radius r in terms of compaction length δ_c . Each colored line refers to different values of perturbation amplitude φ_{max} , given in the legend.

ratios as a function of initial perturbation radius for several perturbation radii. In our models we use a φ_{max} of 2%, for which we get a switch from solitary wave to diapir dominant behavior at $r = 48 \cdot \delta_c$. Smaller amplitudes lead to a switch at a smaller radius and larger amplitudes to a switch at a larger radius.

5.2.2 Model Setup

The model consists of a $L' \times L'$ box with a background porosity, φ_0 , of 0.5%. L' is the non-dimensional side length of the box and equal to 6 times the initial radius of the perturbation. As initial condition a non-dimensional Gaussian bell-shaped porosity anomaly is placed in the middle of the model at $x'_0 = 3$ and $z'_0 = 3$. The Gaussian wave is given by

$$\varphi = \varphi_{max} \cdot \exp \left[- \left(\frac{x' - x'_0}{w'} \right)^2 - \left(\frac{z' - z'_0}{w'} \right)^2 \right], \quad (5.27)$$

where φ_{max} is the amplitude equal to 0.02 in our models and w' corresponds to the width where φ has reached φ_{max}/e . In our case w' is equal to 1.2.

In our model series we vary the ratio of Stokes radius to compaction length from 1.8 to 48 to explore the transition from solitary wave towards diapiric regime. The resolution of the models is chosen to be at least 201×201 grid points and was increased for higher ratios of Stokes radius to compaction length so that the compaction length is resolved by at least 3-4 grid points.

At the top and the bottom domain boundaries, we prescribe an out- and inflow for both melt and solid, respectively, to prevent melt accumulations at the top. The segregation velocity of the background porosity φ_0 is calculated using Eq. (5.18) without the viscous stress term. The corresponding matrix velocity is calculated using the conservation of mass.

At the sides we enforce no horizontal flux boundary conditions. The permeability-porosity relation exponent in our models is always $n = 3$.

To run models for a longer, practically infinite, amount of time we let the models coordinate system follow the maximum melt fraction.

5.2.3 Numerical Approach

We discretize the set of equations using Finite Differences on a staggered grid and solve the system using the code FDCON (Schmelting et al., 2019). Starting from the prescribed initial condition for φ , and assuming $A'(\chi') = 0$ at time 0, the time loop is entered and the biharmonic Eq. (5.20) is solved for ψ' by Cholesky decomposition, from which \vec{v}'_1 is derived. Together with \vec{v}'_2 the resulting solid velocity is used to determine the viscous stress term in the segregation velocity Eq. (5.18). This equation and the melt mass Eq. (5.1) are solved iteratively with strong underrelaxation for φ and $\vec{v}'_f - \vec{v}'_s$ for the new time step using upwind and an implicit formulation of Eq. (5.1). During this internal iteration these quantities are used, via Eq. (5.13), to give $\vec{\nabla} \cdot \vec{v}'_s$, the divergence of the matrix velocity, which is needed in the viscous stress term (Eq. (5.6)). After convergence $\vec{\nabla} \cdot \vec{v}'_s$ is used via Eq. (5.12) to determine χ by LU-decomposition and then to get \vec{v}'_2 . Now $A'(\chi')$ can be determined to be used on the RHS of Eq. (5.19). The procedure is then repeated upon entering the next time step.

Time steps are dynamically adjusted by the Courant criterion times 0.2 based on the fastest velocity, either melt or solid.

The model resolution is a critical parameter in this kind of numerical calculations and should always be kept in mind. With increasing length scale ratio, the compaction length in the model gets smaller and the resolution needs to be increased to keep it equally resolved.

According to several authors (e.g. Räss et al., 2019; Keller et al., 2013), the compaction length should be at least resolved by 4-8 grid points to solve for waves sufficiently accurately. For small length scale ratios this is no problem, where, with a model resolution of 201×201 , up to nearly 30 grid points per compaction length can be achieved. The highest resolution our code can run is 601×601 , which is enough to resolve the compaction length by three grid points for the model with a length scale ratio of 48. Everything above that cannot be sufficiently resolved with respect to studying solitary waves.

Fig. 5.2 shows the resulting models for a length scale ratio of 12 for six different

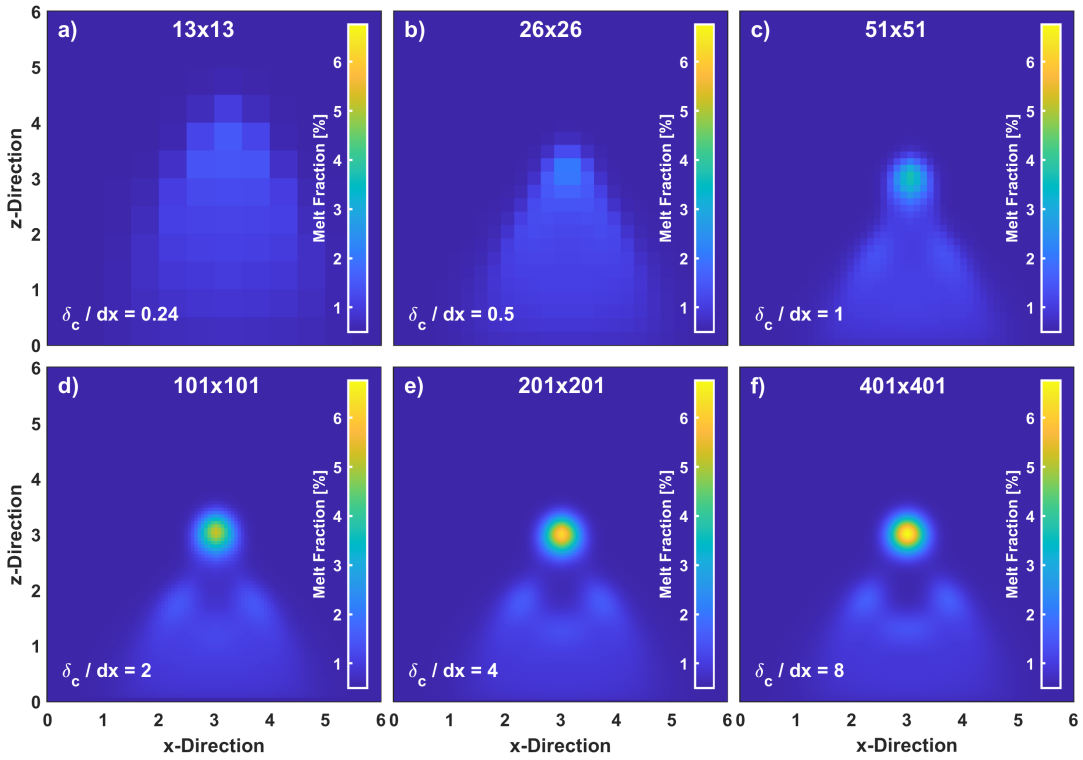


Figure 5.2: The six panels depict a model with an initial perturbation radius of 12 times the compaction length but with different numerical grid resolutions: a) 13×13 b) 26×26 c) 51×51 d) 101×101 , e) 201×201 , f) 401×401 . In the lower left corner in each figure the size of the compaction length in terms of grid length is given.

resolutions. The model states after φ_{max} has risen approximately 0.25 times the initial Stokes radius ($t' = 0.25$) are shown. With increasing resolution, the maximum melt fraction increases strongly from 101×101 to 401×401 by approximately 20% but the velocity of φ_{max} decreases by 7% (not shown in the figure). Both values converge for resolutions higher than 51×51 , corresponding to $\delta_c/dx = 1$. Even though the compaction length is not sufficiently resolved in Fig. 5.2d, one can still observe the main

features of the model: A main solitary wave has emerged from the original gaussian perturbation and secondary porosity waves are beginning to emerge within its wake. Even with $\delta_c/dx = 1$ these features can be observed but are clearly underresolved. With even lower resolutions accumulations at the top of the perturbation can be seen, which can be broadly interpreted as the attempt of a solitary wave to build up. With $\delta_c/dx = 0.24$, the model is too coarse and the results cannot be trusted anymore.

The solitary waves modeled with our code have been compared to the semi-analytical solution of Simpson and Spiegelman (2011), and more benchmarking was carried out in Dohmen et al. (2019).

In a single-phase flow case, where the melt is not allowed to move relatively to the solid, the initial perturbation ascends, shortly after beginning, with a velocity of 0.95 times the calculated Stokes velocity, and then slowly decreases as the original Gauss-shaped wave deforms and loses in amplitude.

5.3 Results

5.3.1 The Transition from Porosity Wave to Diapirism: Varying the initial Wave Radius

In this model series we vary the initial wave radius to cover the transition from porosity waves towards diapirism. As a reminder, due to our scaling the initial wave has always the same size w.r.t. the model box, and “increasing the initial wave radius” is equivalent to decreasing the compaction length or the size of the emerging solitary waves w.r.t. the model box. In Fig. 5.3 the models are shown at $t' = 0.2$. For small radii ($r \leq 12 \cdot \delta_c$) a single porosity wave emerges from the original perturbation. The melt that is not situated within the emerging wave is left behind and has, for the most part, already left the model region. For $r = 2.4 \cdot \delta_c$ the emerged solitary wave is about the size of the initial perturbation and even smaller radii would lead to too big waves that would not fit into the model. With increasing radius, the emerging solitary wave gets smaller. With $r = 12 \cdot \delta_c$, the resulting wave has just a size of 20% the initial perturbation size.

We compare the observed solitary wave velocities of Fig. 5.3b-e to equivalent Stokes velocities for a diapir based on Eq. (5.16). While the dimensional Stokes velocity of a porosity anomaly is proportional to the amplitude of porosity and the square of the radius, the non-dimensional Stokes velocity is always equal to 1. In Fig. 5.4 this non-dimensional Stokes velocity is indicated by the dashed line with the value 1. The colored lines give 2D solitary wave velocities with their appropriate radii, given by Simpson and Spiegelman (2011), normalized by the Stokes velocity corresponding to different initial perturbation radii. These semi analytical solutions are in good agreement to our solitary wave models and differ only by 3-5% percent in velocity, as already shown in Dohmen et al. (2019). The velocities in this figure correspond to ratios of solitary wave velocity to initial perturbation Stokes velocity. Inspection of Fig. 5.4 reveals that for the first four cases of Fig. 5.3b-e with radii smaller or equal $12 \cdot \delta_c$ the phase velocities are always larger than the Stokes velocity. For example, for $r = 12 \cdot \delta_c$, an emerging solitary wave with a typical radius of $4.5 \cdot \delta_c$ has a higher

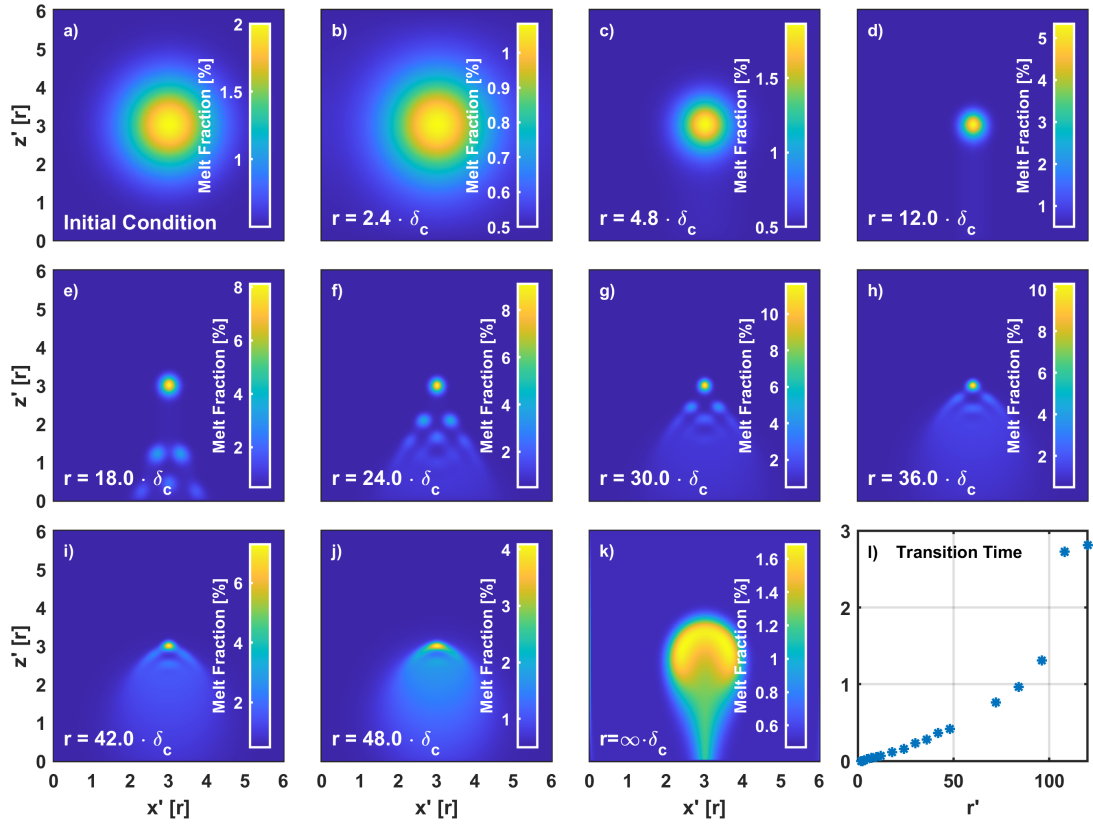


Figure 5.3: Melt ascent morphology as function of initial perturbation radius in terms of compaction length. a) Initial conditions of the model valid for all cases apart of the change in compaction length. b-j) Melt fraction distribution after $t' = 0.2$ for length scale ratios varying between 2.4 and 48. k) Diapiric rise resulting from a compaction length of zero at $t' = 9$. l) Models' transition time as function of length scale ratios varying between 1.8 and 120. The transition time gives the time after which the main wave has reached a solitary wave status.

phase velocity than a $r = 12 \cdot \delta_c$ melt anomaly rising by Stokes flow. Thus, the cases are always in the solitary wave regime.

For greater radii (e.g. $r = 18 \cdot \delta_c - 30 \cdot \delta_c$, Fig. 5.3e-g) the phase velocities of solitary waves are of the order of the Stokes velocity (see Fig. 5.4) and they therefore need more time to separate from the remaining melt of the initial perturbation, still rising with order of Stokes velocity. The amount of melt accommodated within the main solitary wave is just a small percentage of the original perturbation and secondary waves evolve in its remains. With further ascending, more and more solitary waves build up and the former perturbation will sooner or later consist of solitary waves in an ordered cluster or a formation. This formation elongates during ascent as the main wave has a larger amplitude than all the following waves, whose amplitudes are also decreasing with depth, as a higher proportion of melt accumulated at the top of the perturbation. Similar formations of strongly elongated fingers can be also observed in 3D as shown by Räss et al. (2019) who used decompaction weakening. In the models

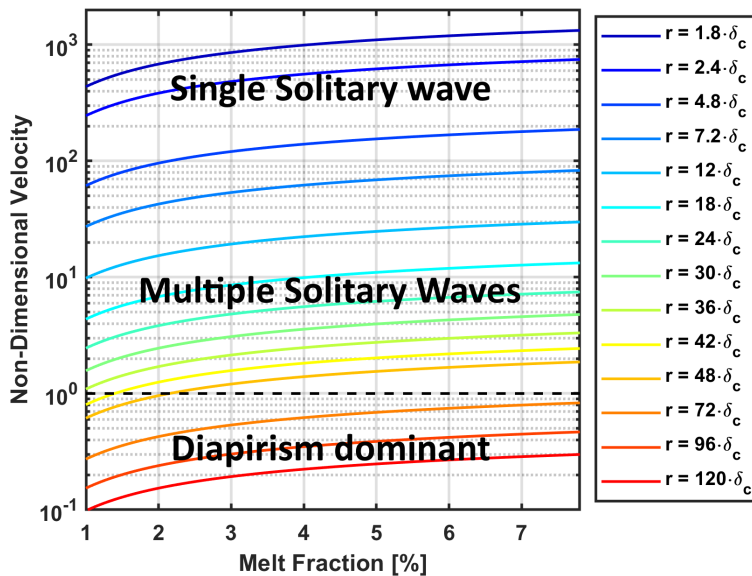


Figure 5.4: The dashed line marks the velocity of the Stokes sphere ($v' = 1$). The colored lines refer to the velocity of a 2D solitary wave, calculated semi-analytically by Simpson and Spiegelman (2011), in our non-dimensionalization, based on the radii shown in the legend.

with smaller radii, the main solitary wave consisted of the majority of melt originally situated within the perturbation and the emergence of secondary waves turns out zero or small, but with greater radii enough melt is left behind to observe the emergence of second and higher generations of solitary waves.

For greater radii (e.g. $r = 24 \cdot \delta_c - 48 \cdot \delta_c$, Fig. 5.3f – j) the phase velocities of solitary waves are almost equal to the Stokes velocity (See Fig. 5.4). This leads to almost no separation after $t' = 0.2$. While for $r = 36 \cdot \delta_c$ a solitary wave has already built up and is rising just ahead of the perturbation, for $r = 42 \cdot \delta_c$ and $r = 48 \cdot \delta_c$ just the accumulation of melt at the top of the perturbation can be observed, which will eventually lead to a solitary wave. Secondary waves also build up with higher runtimes, as can be already seen for $r = 36 \cdot \delta_c$.

For even greater radii the compaction length cannot be sufficiently resolved with our approach, but tests with not sufficiently resolved models have shown that solitary waves can be observed for $r \geq 48 \cdot \delta_c$. At some point they do no longer appear, probably due to lack of sufficient resolution, but our tests show that solitary waves should always emerge, even if its phase velocity is way below the Stokes velocity. As long as the ascending time is long enough and melt is able to move separately to the matrix, independently of segregation velocity, a diapir will evolve into a swarm of a certain number of solitary waves, based on the compaction length. Because the phase velocities of each small solitary wave is small compared to the Stokes velocity of the full swarm we consider such a rising formation of melt as a large scale diapir.

Fig. 5.3l shows the required time for the initial perturbation to build up a solitary wave. This status is achieved after the dispersion relation of the main wave reaches a

point from where it follows the solitary wave dispersion relation. This time increases nearly linearly for small radii ($r \leq 48 \cdot \delta_c$) but increases non-linearly for greater radii. This might be due to lack of proper resolution, but a non-linear trend can be already observed for small radii. The transition time for radii smaller than $30 \cdot \delta_c$ is smaller than 0.2, the time at which the models in Fig. 5.3b-j are shown. The other models already show solitary wave like blobs but did not yet reach their final form.

A classical diapir will evolve only in cases with zero compaction length ($r = \infty \cdot \delta_c$), i.e., melt is not able to move w.r.t. the matrix (Fig. 5.3k). Here, no focusing into solitary waves can be observed and transition time is infinity.

Summarizing Fig. 5.4, the comparison of Stokes and porosity wave velocities explains well our observations shown in Fig. 5.3: For small initial radii the solitary wave velocity is clearly higher and will therefore build up and separate from the melt left behind quickly. For cases with approximately equal perturbation to solitary wave radius only one solitary wave will build up, which includes most of the melt of the initial perturbation. With increasing perturbation radius, the velocity ratio decreases and multiple solitary waves, requiring more time, will emerge, each including only a fraction of the melt originally situated in the initial perturbation. But even with velocity ratios smaller than 1, solitary waves emerge and, not able to separate, rise just ahead of the remains, slowly elongating the initial perturbation.

5.3.2 Effects on the Mass Flux

It is important to study the partitioning between rising melt and solid mass fluxes in partially molten magmatic systems because melts and solids are carriers of different chemical components. Within our Boussinesq approximation we may neglect the density differences between solid and melt. Then our models allow to evaluate vertical mass fluxes of solid or fluid by quantifying the vertical velocity components multiplied with the melt or solid fractions, respectively:

$$q'_{sz} = (1 - \varphi) \cdot v'_{sz} q'_{fz} = \varphi \cdot v'_{fz}. \quad (5.28)$$

Horizontal profiles of the mass fluxes through rising melt bodies at the vertical positions of maximum melt fraction at timesteps where the main wave has just reached the status of a solitary wave are calculated (Fig. 5.5).

The mass fluxes of solid and fluid are strongly affected by the change of the initial radius from the solitary wave regime towards the diapiric regime. For $r = 2.4 \cdot \delta_c$, where we observe a solitary wave, the fluid has its peak mass flux in the middle of the wave and the solid is going downwards, against the phase velocity. In the center the fluid flux is about 10 times higher than the solid net flux. The upward flow in the center is balanced by the matrix dominated downward flow inside and outside the wave. For $r = 12 \cdot \delta_c$ the wave area is much smaller and the ratio between solid and fluid flux is still around the order of 10. At the boundary of the wave the solid is nearly not moving at all, but a minimum can be observed within the center of it. For $r' = 24 \cdot \delta_c$ the solid flux is just above zero in the center and increases to a maximum towards the flanks of the wave, that is still about ten times smaller than the maximum fluid flux. With $r' = 48 \cdot \delta_c$ the solid flux is just about three times smaller than the fluid flux, but

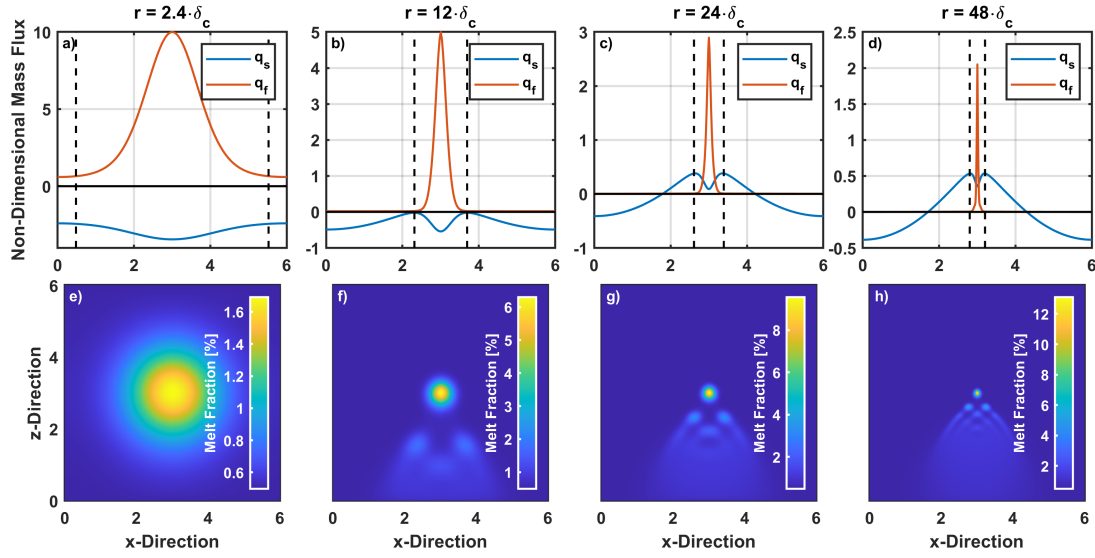


Figure 5.5: The upper row panels depict the solid and fluid mass fluxes of a horizontal line cutting through the maximum melt fraction at time steps where the main wave has just reached the status of a solitary wave. These timesteps are $t' = 0.02$; 0.068 ; 0.155 ; 0.416 from left to right, respectively. The bottom row panels depict the corresponding melt porosity fields. All quantities shown are non-dimensional.

most of the material ascent is accomplished by the solid. This suggests that diapiric rise begins to dominate.

The transition from solitary waves towards diapirism on qualitative model observations was so far only based on observations. We now invoke a more quantitative criterion. In a horizontal line passing through the anomaly's porosity maximum we define the total vertical mass flux of the rising magma body by $\int_{\varphi > \varphi_0} (q_f + q_s) dx$ where the integration is carried out only in the region of increased porosity $\varphi > \varphi_0$. This mass flux is partitioned between the fluid mass flux, $\int_{\varphi > \varphi_0} q_f dx$, and the solid mass flux, $\int_{\varphi > \varphi_0} q_s dx$. With these we define the partition coefficients

$$C_{soli} = \frac{\int_{\varphi > \varphi_0} q_f dx}{\int_{\varphi > \varphi_0} (q_f + q_s) dx} \quad (5.29)$$

and

$$C_{dia} = \frac{\int_{\varphi > \varphi_0} q_s dx}{\int_{\varphi > \varphi_0} (q_f + q_s) dx} \quad (5.30)$$

The sum $C_{soli} + C_{dia}$ is always 1 and if $C_{soli} > C_{dia}$ then the solitary wave proportion is dominant, while for $C_{soli} < C_{dia}$ diapirism is dominant. In Fig. 5.6a these partition coefficients for several initial radii are shown. In red are the diapir and in blue the solitary wave partition coefficients.

For $r = 1.8 \cdot \delta_c$, C_{soli} is equal to 5 and C_{dia} is equal to -4, i.e. we have a downward solid flux. With increasing radius C_{dia} increases until it changes its sign, and the matrix flows upward, at $r \approx 20 \cdot \delta_c$. It eventually becomes bigger than C_{soli} at $r = 36 \cdot \delta_c$ and

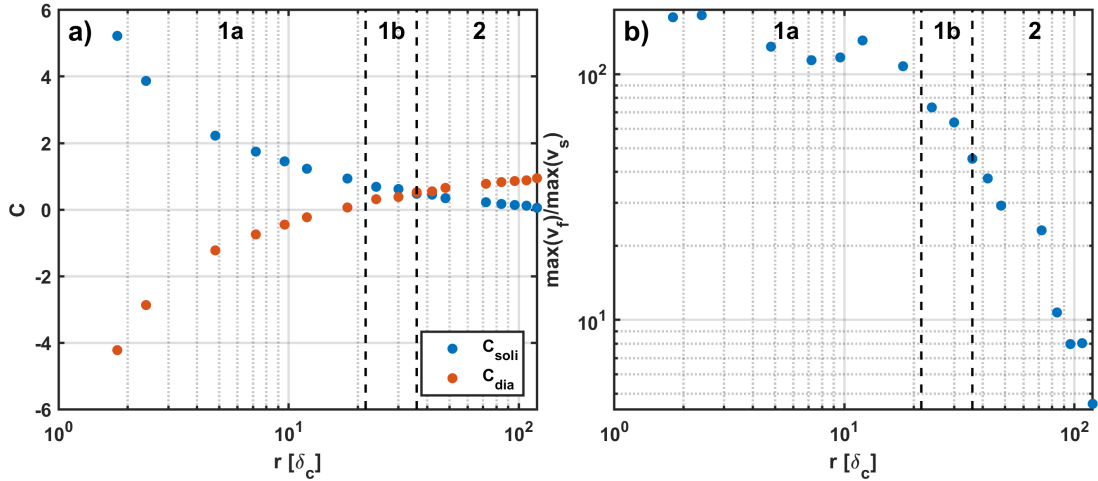


Figure 5.6: Quantitative parameters as function of initial perturbation radius in terms of compaction length. a) Solitary wave (blue) and diapir (red) partition coefficients for several initial perturbation radii. b) Ratio of maximum fluid velocity to maximum absolute solid velocity in the entire model.

then approaches 1 for bigger radii. C_{soli} changes so that the sum of both is always equal to 1. Even though diapirism is dominant for $r > 36 \cdot \delta_c$, we still observe solitary waves, yet their phase velocities are much smaller than the large-scale rising velocities of the full melt formation.

The ratio of maximum fluid velocity (i.e. \vec{v}_f) to absolute matrix velocity (Fig. 5.6b) shows, that for small radii, where $C_{soli} \gg C_{dia}$, this ratio is approximately constant with a high value of about 100. The absolute velocity maxima itself are not constant but decrease with the same rate until the switch of negative to positive matrix mass flux, where the absolute matrix velocity starts to increase, while the fluid velocity keeps decreasing. At this zero crossing we would expect a ratio of infinity, but while the zero crossing takes place within the center of the solitary wave, other regions near the wave still have finite vertical velocities. This switch from negative to positive mass flux was already observed by Scott (1988), but while they changed the viscosity ratio as an independent constant model parameter, we change the radius and keep the viscosity law the same, still evolving with φ . Both describe the transition from a two-phase limit towards the Stokes limit, but in our formulation, we are able to reach the Stokes limit while Scott's formulation (1988) is restricted to two-phase flow. With even greater radii the velocity ratio will eventually converge towards 1, where melt is no longer able to move relatively to the matrix (i.e. $\vec{v}_f = \vec{v}_s$) and material will be transported collectively as in single-phase flow. These last models are not sufficiently resolved to obtain leading and secondary solitary waves, but still show the expected behavior in terms of macroscopically rising partially molten diapir.

Based on these observations, the evolution of these models can be divided into two regimes: (i) In the solitary wave regime ($r \leq 36 \cdot \delta_c$) C_{soli} is larger than C_{dia} and the initial perturbation emerges into waves that have the properties of solitary waves and ascend with constant velocity and staying in shape. This regime can be fur-

ther divided into (ia) ($r < 20 \cdot \delta_c$), where the solid mass flux is negative, and (ib) ($20 \cdot \delta_c \leq r < 36 \cdot \delta_c$), where the solid moves upwards with the melt. Waves in these regimes are very similar but the further we are in regime (ia) the less solitary waves will emerge out of the initial perturbation. For radii smaller than about $4.8 \cdot \delta_c$ only one wave will merge. In regime (ib) the perturbation will always emerge into multiple solitary waves.

In the diapirism-dominated regime (ii) ($r \geq 36 \cdot \delta_c$), C_{dia} is larger than C_{soli} but, as the fluid melt is still able to move relatively to the solid matrix, solitary waves build up and the whole partially molten region will evolve into a swarm of them. The phase velocities of these waves are very small compared to the Stokes velocity of the perturbation and the whole swarm will rise as a diapir, whose buoyancy is still comparable to the buoyancy of the initial perturbation's.

The endmember of the second regime can be reached by prohibiting the relative movement of fluid ($r = \infty \cdot \delta_c$), for which the compaction length has not to be sufficiently resolved. In this regime the initial perturbation will not disintegrate into solitary waves but rise as a well-formed partially molten diapir. In every other case, in the present model, where fluid is able to move w.r.t. the solid, at some point all diapirs will evolve into a swarm of solitary waves which can be infinitely small compared to the initial perturbation. However, this is expected to happen only after a long distance of diapiric rise. In cases where the size of solitary waves is comparable to the perturbation (e.g. regime (i)) this will occur sooner and in cases, where solitary waves are much smaller, later. Their observation is mostly limited by resolution. For models that allow for the diapir to grow (e.g. Keller et al., 2013) they may not dissolve into solitary waves, as it approaches the single-phase limit.

5.4 Discussion

5.4.1 Application to Nature

While in our models the perturbation size in terms of compaction lengths was systematically varied but kept constant within in each model, our results might also be applicable to natural cases in which the compaction length varies vertically. In the case of compaction length decreasing with ascent a porosity anomaly might start rising as a solitary wave but then at some point might enter the second regime where diapiric rise is dominant. If this boundary is sharp, the solitary wave might disintegrate into several smaller solitary waves that rise as a diapiric swarm. If the boundary is a continuous transition the wave should slowly shrink and become slower. The melt left behind might also evolve into secondary solitary waves.

A decreasing compaction length could be accomplished by decreasing the matrix viscosity or the permeability, or by increasing the fluid viscosity. Decreasing matrix viscosity might be for example explainable by local heterogeneities, temperature anomalies for example due to secondary convective overturns in the asthenosphere or by a vertical gradient of water content, which may be the result of melt segregation aided volatile enrichment at shallow depths in magmatic systems. This could lead to the propagation of magma-filled cracks (Rubin, 1995) as already pointed out in Connolly

and Podladchikov (1998). The latter authors have looked at the effects of rheology on compaction-driven fluid flow and came to similar results for an upward weakening scenario. The decrease of permeability due to decrease in background porosity might be an alternative explanation. In the hypothetical case of a porosity wave reaching the top of partially molten region within the Earth's upper mantle or lower crust, the background porosity might decrease which would most certainly lead to focusing, because the compaction length will decrease, and eventually, when reaching melt free rocks, the solitary waves might be small enough and its amplitude might be high enough to trigger the initiation of dykes.

Even though most diapirs should, according to our models, disintegrate into numerous solitary waves, not all will inevitably. Within regime (i) solitary waves are possible and most probably expected but the deeper we are in regime (ii) the less expected is the disintegration because a long time is needed to build up. In nature, different from our models, they cannot rise for an infinite amount of time. The time needed to build up a solitary wave increases non-linearly with r (c.f. Fig. 5.31). For example, while for $r = 4.8 \cdot \delta_c$ a solitary wave is completely evolved after $t' = 0.02$, for $r = 48 \cdot \delta_c$ it needs until $t' = 0.4$, i.e., equivalent to the diapiric rise time necessary to ascend the distance approximately half the initial radii. Additionally, as already pointed out, if a model setup allows for the diapir to grow, it could approach the single-phase flow, prohibiting the emergence of solitary waves (cf. Keller et al., 2013).

5.4.2 Model Limitations

The introduced partition coefficients help to distinguish whether solitary wave or diapiric rise is dominant but cannot be solely consulted whether a solitary wave or a diapir can be expected. As the fluid velocity and flux is still very high in the waves center for diapiric dominant cases, small solitary waves will build up. However, the net mass flux is dominated by the large scale rising solid, and the formation time of small solitary waves might be long. Additionally, the internal circulation of diapirs can be faster than the phase velocity which would smear out the emergence of solitary waves and not allow for them to emerge. Due to limitations of our model, we are not able to reach regions where solitary waves are small enough and their phase velocity slow enough to observe this.

While the minimum size of solitary waves in nature might be in some way limited by the grain size, in numerical models the minimum size is limited by the model's resolution. We restrict our models in this study to cases where the compaction length is at least resolved by 3 grid lengths dx (i.e. $\delta_c \geq 3 \cdot dx$) to get fairly resolved solitary waves, but they can be also observed for much worse resolved compaction lengths. The resolution test (Fig. 5.2) shows that, even though they are not solved decently, probable solitary waves can be observed for cases with $\delta_c = dx$. Smaller resolutions can show indications of solitary waves but should not be trusted as other tests (not shown here) with similar resolutions result in spurious channeling. For very poorly resolved compaction lengths ($\delta_c < 0.25 \cdot dx$ for our models) no indications of solitary waves can be observed, and the partially molten perturbation ascends as a diapir. The deeper we are in regime (ii), the more dominant are the dynamics of diapirism on a length

scale of r compared to Darcy flow or solitary waves on the unresolved length scale of δ_c . Thus, two-phase flow, either Darcy flow or solitary waves, becomes negligible for $r \gg \delta_c$ and partially molten diapirs can be regarded as well resolved.

5.5 Conclusion

This work shows, that depending on the extent of a partially molten region within the Earth, the resulting ascent of melt may not only occur by solitary waves or by diapirs, but by a composed mechanism, where a diapir splits up into numerous solitary waves. Their phase velocities might become so slow that the whole swarm will ascend as a diapir, just slowly elongating due to the main solitary wave having a higher amplitude and therefore higher phase velocity than the following ones. Depending on the ratio of the melt anomalies size to the compaction length, or rather the models length scale to compaction length ratio, we can classify the ascent behavior into two different regimes using mass flux and velocity of matrix and melt: (i) Solitary wave a and b, and (ii) diapirism-dominated. In regime (i) the matrix sinks with respect to the rising melt, in (ii) also the matrix rises, but very slowly. The further we are in this regime the less solitary waves will emerge out of the initial perturbation until, eventually, only one solitary wave will emerge. On first order these regimes can be explained by comparing Stokes velocity of the rising perturbation with the solitary waves phase velocity. If the solitary wave velocity is higher than the Stokes velocity a solitary wave will evolve and, if lower, diapirism is dominant, but still solitary waves will build up if the ascending time is long enough. The deeper we are in regime (ii), the more time is needed to build up solitary waves and the less likely it is that they will appear in nature. The endmember of regime (ii), pure diapirism, can be reached if fluid is not allowed to move separately to the matrix.

Especially around the transition of the regimes numerical resolution plays an important role as the compaction length may be under-resolved to allow for the emergence of solitary waves. Hence it should be generally important for two-phase flow models to inspect whether solitary waves are expected and if so, do they have a major influence on the conclusions made.

Acknowledgment

The authors would like to thank Tobias Keller and an anonymous reviewer for their extensive and detailed reviews, which helped to greatly improve this publication.

References

- Barcilon, V. and Lovera, O. M. (1989). Solitary waves in magma dynamics. *Journal of Fluid Mechanics*, 204(1989):121–133.
- Bittner, D. and Schmeling, H. (1995). Numerical Modelling of Melting Processes

- and Induced Diapirism In the Lower Crust. *Geophysical Journal International*, 123(1):59–70.
- Connolly, J. A. (1997). Devolatilization-generated fluid pressure and deformation-propagated fluid flow during prograde regional metamorphism. *Journal of Geophysical Research B: Solid Earth*, 102(B8):18149–18173.
- Connolly, J. A. and Podladchikov, Y. Y. (1998). Compaction-driven fluid flow in viscoelastic rock. *Geodinamica Acta*, 11(2-3):55–84.
- Connolly, J. A. and Podladchikov, Y. Y. (2013). *A hydromechanical model for lower crustal fluid flow*. Springer Berlin Heidelberg.
- Connolly, J. A. D. and Podladchikov, Y. Y. (2015). An analytical solution for solitary porosity waves: Dynamic permeability and fluidization of nonlinear viscous and viscoplastic rock. *Geofluids*, 15(1-2):269–292.
- Costa, A. (2006). Permeability-porosity relationship: A reexamination of the Kozeny-Carman equation based on a fractal pore-space geometry assumption. *Geophysical Research Letters*, 33(2):1–5.
- Dohmen, J., Schmeling, H., and Kruse, J. P. (2019). The effect of effective rock viscosity on 2-D magmatic porosity waves. *Solid Earth*, 10(6):2103–2113.
- Griffiths, R. W. (1986). The differing effects of compositional and thermal buoyancies on the evolution of mantle diapirs. *Physics of the Earth and Planetary Interiors*, 43(4):261–273.
- Jordan, J. S., Hesse, M. A., and Rudge, J. F. (2018). On mass transport in porosity waves. *Earth and Planetary Science Letters*, 485:65–78.
- Katz, R. F. (2008). Magma dynamics with the enthalpy method: Benchmark solutions and magmatic focusing at mid-ocean ridges. *Journal of Petrology*, 49(12):2099–2121.
- Keller, T., Katz, R. F., and Hirschmann, M. M. (2017). Volatiles beneath mid-ocean ridges: Deep melting, channelised transport, focusing, and metasomatism. *Earth and Planetary Science Letters*.
- Keller, T., May, D. A., and Kaus, B. J. (2013). Numerical modelling of magma dynamics coupled to tectonic deformation of lithosphere and crust. *Geophysical Journal International*, 195(3):1406–1442.
- McKenzie, D. (1984). The generation and compaction of partially molten rock. *Journal of Petrology*, 25(3):713–765.
- Omlin, S., Malvoisin, B., and Podladchikov, Y. Y. (2017). Pore Fluid Extraction by Reactive Solitary Waves in 3-D. *Geophysical Research Letters*, 44(18):9267–9275.
- Popov, A. A. and Sobolev, S. V. (2008). SLIM3D: A tool for three-dimensional thermo-mechanical modeling of lithospheric deformation with elasto-visco-plastic rheology. *Physics of the Earth and Planetary Interiors*, 171(1-4):55–75.

- Rabinowicz, M., Ceuleneer, G., and Nicolas, A. (1987). Melt segregation and flow in mantle diapirs below spreading centers: Evidence from the Oman Ophiolite. *Journal of Geophysical Research*, 92(B5):3475–3486.
- Räss, L., Duretz, T., and Podladchikov, Y. Y. (2019). Resolving hydromechanical coupling in two and three dimensions: Spontaneous channelling of porous fluids owing to decompaction weakening. *Geophysical Journal International*, 218(3):1591–1616.
- Richard, G. C., Kanjilal, S., and Schmeling, H. (2012). Solitary-waves in geophysical two-phase viscous media: A semi-analytical solution. *Physics of the Earth and Planetary Interiors*, 198-199:61–66.
- Rivalta, E., Taisne, B., Bungler, A. P., and Katz, R. F. (2015). A review of mechanical models of dike propagation: Schools of thought, results and future directions. *Tectonophysics*, 638(C):1–42.
- Rubin, A. M. (1995). Propagation of magma-filled cracks. *Annual Review of Earth and Planetary Sciences*, pages 287–336.
- Schmeling, H. (2000). *Partial melting and melt segregation in a convecting mantle*. Springer.
- Schmeling, H., Marquart, G., Weinberg, R., and Wallner, H. (2019). Modelling melting and melt segregation by two-phase flow: New insights into the dynamics of magmatic systems in the continental crust. *Geophysical Journal International*, 217(1):422–450.
- Scott, D. R. (1988). The competition between percolation and circulation in a deformable porous medium. *Journal of Geophysical Research*, 93(B6):6451–6462.
- Scott, D. R. and Stevenson, D. J. (1984). Magma solitons. *Geophysical Research Letters*, 11(11):1161–1164.
- Simpson, G. and Spiegelman, M. (2011). Solitary wave benchmarks in magma dynamics. *Journal of Scientific Computing*, 49(3):268–290.
- Slezkin, A. (1955). Dynamics of viscous incompressible fluid. *Moscow (in Russian)*.
- Sparks, D. W. and Parmentier, E. M. (1991). Melt extraction from the mantle beneath spreading centers. *Earth and Planetary Science Letters*, 105(4):368–377.
- Spiegelman, M. (1993). Flow in deformable porous media. Part 2 Numerical analysis - the relationship between shock waves and solitary waves. *J. Fluid Mech.*, 247:39–63.
- Spiegelman, M., Kelemen, P. B., and Aharonov, E. (2001). Causes and consequences of flow organization during melt transport: The reaction infiltration instability in compactible media. *Journal of Geophysical Research*, 106:2061–2077.
- Spiegelman, M. and McKenzie, D. (1987). Simple 2-D models for melt extraction at mid-ocean ridges and island arcs. *Earth and Planetary Science Letters*, 83(1-4):137–152.

- Sramek, O., Milelli, L., Ricard, Y., and Labrosse, S. (2012). Thermal evolution and differentiation of planetesimals and planetary embryos. *Icarus*, 217(1):339–354.
- Turcotte, D. L. and Schubert, G. (1984). *Geodynamics*. Cambridge University Press.
- Watson, S. and Spiegelman, M. (1994). Geochemical Effects of Magmatic Solitary Waves—I. Numerical Results. *Geophysical Journal International*, 117(2):284–295.
- Wiggins, C. and Spiegelman, M. (1995). Magma migration and magmatic solitary waves in 3D. *Geophysical Research Letters*, 22(10):1289–1292.
- Wilson, M. (1989). *Igneous petrogenesis*. Unwin Hyman, London.
- Yarushina, V. M., Podladchikov, Y. Y., and Connolly, J. A. (2015). (De)compaction of porous viscoelastoplastic media: Solitary porosity waves. *Journal of Geophysical Research : Solid Earth*, pages 1–20.

Chapter 6

Publication 3

Modeling Trace Element Transport in Melt using Two-Phase Flow: Investigation of Isotope Enrichment in the Upper Earth

Geochemistry, Geophysics, Geosystems (submitted)

Janik Dohmen¹, Harro Schmeling¹ & Jan Philipp Kruse¹

¹Institute for Geoscience, Goethe University Frankfurt, Frankfurt, Germany

6.1 abstract

Measurements of trace elements in melts are an important tool to gain information about what is happening inside the Earth, regarding melt and melt transport. Many models have been introduced to explain concentrations at the surface as a function of melt degree, equilibration and dynamics.

In this publication, we introduce a fully consistent 2D model for major as well as trace element transport in melts, using a two-phase flow approach, including melting, freezing and re-equilibration. A set of equations is presented that cover mass conservation of major and trace elements in a solid and fluid separately, momentum conservation in a fluid and mixture, and energy conservation for the mixture in thermal equilibrium. Melting is accomplished using a binary melting law.

A possible application is a subduction-arc region; in a simple representation finite difference model, convection leads to a partially molten plume, eventually resulting in redistribution of trace elements. It can be shown that in a closed system, the solid trace element concentration in an emplacement zone approaches an asymptotic value that depends on multiple model parameters. The approach time depends only on the size ratio of the partially molten plume to the whole convection source region.

A numerical 0D model is introduced that can explain the 2D results, and a simple equation is found that can be used to fit the results.

The retention number, giving the resistance of a fluid to percolate through a porous matrix, has a major influence not only on the degree of enrichment but also on the

dynamics of the whole system, ultimately leading to different enrichment elevation depths.

6.2 Introduction

We are still unable to visually observe what is happening inside the Earth, and geoscientists are limited to observations that can be made near the surface to give predictions on deeper phenomena. One observation that can be made is measurements of trace element concentrations in volcano lavas (Rollinson, 1993). Using this data, forward models can be used to obtain an idea on the sources and the degree of melting. Batch and fractional melting models were introduced (Gast, 1968; Shaw, 1970) that represent two end-members in a variety of different melt processes. Later, more complicated models were established that assume more complex melt histories (e.g. Plank and Langmuir, 1992; Holness and Richter, 1989; Langmuir et al., 1977; McKenzie and O’nions, 1992; Kimura, 2017). However, these models still neglect the actual fluid dynamics of mass transport with melts. The relative movement of a melt to a solid is of utmost importance, and models were introduced to address this two-phase flow problem (McKenzie, 1984; Schmeling, 2000; Bercovici et al., 2001). Much research has been carried out since then, looking at the importance of relative movement of solids and melts in geodynamic processes (e.g. Ribe, 1985; Allen, 1985; Scott and Stevenson, 1986; Scott, 1988).

Fortunately, several studies coupled these fluid dynamical models with geochemical ones. Iwamori (1993) examined a one-dimensional upwelling mantle model and predicted trace element concentrations for various melting scenarios. Spiegelman (1996) gave a general overview on trace element transport in a two-dimensional model and evaluated the sensitivity of fluid dynamics on trace element concentrations. Much work has been carried out on the transport of volatiles in melts that can be described by the same set of equations (e.g. Iwamori, 1998, 2007; Keller and Katz, 2016; Keller et al., 2017). Recent work was carried out on the transport of trace elements in melts (e.g. Ikemoto and Iwamori, 2014; Baitsch-Ghirardello et al., 2014), but the focus was on pure geochemical modeling (e.g. Kimura, 2017).

All of these mentioned models either neglect the fluid dynamics of melt percolation or give no fully self-consistent description for the trace element exchange between the solid and fluid phases during melting and freezing, including re-equilibration.

Spiegelman (1996) derived full equations for the partition of trace elements between solid and fluid but did not implement the possibility of freezing and gave only equations for either pure equilibrium or non-equilibrium melting.

Ikemoto and Iwamori (2014) assumed instantaneous partitioning between all phases present and calculated the transport in fluid and solid respectively. Only equilibrium partitioning was possible.

Solano et al. (2014) was the first to present a model of both major and trace element transport in a mush while allowing for chemical reaction between the phases, but the model was applied only to 1D columns.

Bo et al. (2018) gave equations for trace element transport, including melting and re-equilibration, but neglected the possibility of freezing. A constant or variable (but

always positive) melt generation was applied in a 1D column model, whereby the melt generation rate was not a self-consistent result of the model.

The aim of the present work is to introduce a 2D model that allows for self-consistent transport and partitioning of major as well as trace elements, including melting and freezing, based on a two-component phase diagram. Re-equilibration of trace elements between the solid and fluid with time is considered as well. The model is applied to a volcanic subduction back arc.

In subduction arcs, water from the subducting plate percolates upwards (Wilson et al., 2014; Iwamori, 1998), where it interacts with the mantle to greatly depress the solidus and liquidus (Katz et al., 2003). Primitive arc melts are produced (Gaetani and Grove, 1998; Grove et al., 2006) that travel to the Earths surface to erupt in a volcanic arc. The dynamics of a mantle wedge between subducting and overlying lithosphere have been intensely researched (van Keken, 2003, and references therein).

In the present work, we use a simple 2D representation of a mantle wedge as a closed-box model, allowing for convection, melting and material transport with the melt. Ultimately, a 0D model is introduced to quantitatively explain the enrichment of trace elements in a layer above the convection cells, recreating results of the 2D model.

6.3 Methods

6.3.1 Governing Equations for Two-Phase Flow

To model the transport of trace elements in a melt, the fluid melt has to be able to move relative to the solid matrix. This is accomplished by using the general equations of two-phase flow, where mass and momentum conservation are calculated separately for the solid and fluid. The energy equation is expressed for the mixture of the solid and fluid, assuming that they are always in thermal equilibrium.

The equations used here are based on McKenzie (1984); Schmeling (2000); Bercovici et al. (2001), and in the following, the subscripts s and f denote variables associated with the solid and the fluid, respectively. Conservation of mass for the fluid is given by

$$\frac{\partial \rho_f \varphi}{\partial t} + \vec{\nabla} \cdot (\rho_f \varphi \vec{v}_f) = \Gamma \quad (6.1)$$

and conservation of mass for the solid by

$$\frac{\partial \rho_s (1 - \varphi)}{\partial t} + \vec{\nabla} \cdot (\rho_s (1 - \varphi) \vec{v}_s) = -\Gamma. \quad (6.2)$$

ρ_s and ρ_f are the densities, φ is the melt fraction, \vec{v}_s and \vec{v}_f are the velocities and Γ is the melt generation rate, describing the mass exchange between the solid and fluid. Γ is positive while melting and negative while freezing.

The momentum of the fluid is conserved by a generalized form of the Darcy equation

$$\vec{v}_f - \vec{v}_s = -\frac{k_\varphi}{\mu \varphi} \left(\vec{\nabla} P_f - \rho_f \vec{g} \right). \quad (6.3)$$

where μ is the fluid viscosity and P_f is the fluid pressure. The permeability k_φ is given by the Kozeny-Carman relation (e.g. Costa, 2006)

$$k_\varphi = k_0 \varphi^n. \quad (6.4)$$

k_0 and n are parameters depending on the geometry of the pores and grain size, where n is usually taken to be between 2 and 3.

The conservation of momentum for the solid-fluid mixture is given by

$$\bar{\rho} \vec{g} - \vec{\nabla} P_f + \vec{\nabla} \cdot \tau = 0. \quad (6.5)$$

Here, $\bar{\rho}$ is the mixture density given by $\bar{\rho} = (1 - \varphi) \rho_s + \varphi \rho_f$, and τ is the effective viscous stress tensor of the matrix

$$\tau = \eta \left(\frac{\partial v_{si}}{\partial x_j} + \frac{\partial v_{sj}}{\partial x_i} \right) + \left(\zeta - \frac{2}{3} \eta \right) \delta_{ij} \nabla \cdot \vec{v}_s. \quad (6.6)$$

where η and ζ are the shear and volume viscosity, respectively.

Note that in Eq. (6.3) and Eq. (6.5) P_f is the same. Therefore, both equations can be merged to eliminate the pressure:

$$\vec{v}_f - \vec{v}_s = -\frac{k_0 \varphi^{n-1}}{\mu} \left(\Delta \rho_f \vec{g} (1 - \varphi) + \vec{\nabla} \cdot \tau \right). \quad (6.7)$$

It is often useful to incorporate nondimensional numbers in this kind of equations:

$$\begin{aligned} Ra &= \frac{\rho_0 g \alpha \Delta T h^3}{\eta_0 \kappa}, & Ra_m &= \frac{\Delta \rho_f g h^3}{\eta_0 \kappa} \\ Ra_e &= \frac{\Delta \rho_e g h^3}{\eta_0 \kappa}, & Rt &= \frac{\mu h^2}{\eta_0 k_0} \end{aligned} \quad (6.8)$$

Ra , Ra_m and Ra_e are the Rayleigh numbers that represent the buoyancy due to temperature, melt density and enrichment density, respectively. Rt is the retention number, giving the resistance of the fluid to percolate through the matrix. The subscript 0 denotes variables at $\varphi = 0$. In addition, α is the temperature expansion coefficient, and κ is the thermal diffusivity. ΔT is the difference in temperature from the top to the bottom of the model domain. $\Delta \rho_f$ is the density difference between initial density and melt. $\Delta \rho_e$ is the density difference between initial density and the density of a material completely enriched in major elements. These densities can be used to calculate the mixture density

$$\bar{\rho} = \rho_0 - \rho_0 \alpha T - \Delta \rho_f \varphi - \Delta \rho_e f (1 - \varphi), \quad (6.9)$$

while the solid and fluid densities are

$$\begin{aligned} \rho_s &= \rho_0 - \rho_0 \alpha T - \Delta \rho_e f, \\ \rho_f &= \rho_0 - \rho_0 \alpha T - \Delta \rho_f. \end{aligned} \quad (6.10)$$

Here, f is the degree of enrichment or depletion in major elements and is further described later in this section.

Finally, a scaling law can be introduced to incorporate the nondimensional numbers Eq. (6.8):

$$\begin{aligned}
 (x, z) &= (x', z') \cdot h & \vec{v}_{s,f} &= \vec{v}'_{s,f} \cdot \frac{\kappa}{h} & t &= t' \cdot \frac{h^2}{\kappa} & T &= T' \cdot T_{sc} \\
 \rho &= \rho' \cdot \rho_0 & (\tau, P) &= (\tau', P') \cdot \frac{\eta_0 \kappa}{h^2} & (\eta, \zeta) &= (\eta', \zeta') \cdot \eta_0 \\
 c_{s,f} &= c'_{s,f} \cdot c_0 & L &= L' \cdot c_P T_{sc}.
 \end{aligned} \tag{6.11}$$

Primed values refer to nondimensional values.

Using Eq. (6.11) and Eq. (6.8) with Eq. (6.3) gives

$$\vec{v}'_f - \vec{v}'_s = -\frac{\varphi^{n-1}}{Rt} \left(\vec{\nabla} P'_f - Rm \cdot \delta_{i3} \right), \tag{6.12}$$

and with Eq. (6.5) gives

$$[Ra \cdot T' + Ra_m \cdot \varphi + Ra_e \cdot f(1 - \varphi)] \delta_{i3} - \vec{\nabla}' P'_f + \vec{\nabla}' \tau' = 0. \tag{6.13}$$

The pressure eliminated equation (Eq. (6.7)) becomes

$$\vec{v}'_f - \vec{v}'_s = \frac{\varphi^{n-1}}{Rt} \left[(Ra_m \cdot (1 - \varphi) - Ra_e \cdot f(1 - \varphi)) \delta_{i3} - \vec{\nabla}' \tau' \right]. \tag{6.14}$$

The energy conservation is given by an equation for the solid-fluid mixture

$$\bar{\rho} c_P \left(\frac{\partial T}{\partial t} + \vec{v}_{bar} \cdot \vec{\nabla} T \right) = \vec{\nabla} \cdot (\lambda \vec{\nabla} T) - L \Gamma. \tag{6.15}$$

Here, c_P is the specific heat capacity, T is the temperature, λ is the thermal conductivity L is the latent heat per mass, and \vec{v}_{bar} is the barycentric velocity

$$\vec{v}_{bar} = \frac{\rho_f \varphi \vec{v}'_f + \rho_s (1 - \varphi) \vec{v}'_s}{\bar{\rho}}. \tag{6.16}$$

Eq. (6.15) can be nondimensionalized using Eq. (6.11) to give

$$\frac{\partial T'}{\partial t'} + \vec{v}'_{bar} \cdot \vec{\nabla}' T' + \frac{\alpha g h}{c_P} v'_z T' = \vec{\nabla}' \cdot (\rho' \vec{\nabla}' T') + L' \Gamma'. \tag{6.17}$$

For the viscosities, a temperature and melt fraction dependent law is chosen:

$$\eta = \eta_0 \cdot \exp \left[\frac{E_a}{RT_0} \left(\frac{T}{T_0} - 1 \right) \right] \cdot \left(1 - \frac{\varphi}{c_1} \right)^{k_1}, \tag{6.18}$$

$$\zeta = \eta_0 \cdot \exp \left[\frac{E_a}{RT_0} \left(\frac{T}{T_0} - 1 \right) \right] \cdot c_2 (c_1 - \varphi)^{k_2/\varphi}. \tag{6.19}$$

A power law for the shear rate dependency is neglected. The exponential functions of Eq. (6.18) and Eq. (6.19) describe the temperature dependence taken from Turcotte and Schubert (2014), stating that the viscosity is equal to η_0 for $T = T_0$. The prefactor ($E_a/R/T_0$) of the linear temperature term describes the rate of decrease or increase with changing T and contains the activation energy E_a , the gas constant R

and a reference temperature T_0 . For simplification, this factor is chosen to be 10 in accordance to typical values for the upper mantle (e.g. Karato and Wu, 1993). T_0 is 800 °C. The second part of the viscosity laws gives the melt fraction dependence taken from Schmeling et al. (2012). This part is based on numerical models, predicting viscous weakening of a prescribed melt network geometry consisting of only films. The equation is parameterized to fit the numerical results and can be used with $k_1 = a_1(a_2 + \alpha(1 - a_2))$, $c_1 = \frac{b_1\alpha}{1+b_2\alpha^{k_3}}$, $c_2 = \frac{4}{3}\alpha c_1^{-k_2} \cdot (c_3(1 - \alpha) + \alpha)$ where $a_1 = 0.97$, $a_2 = 0.8$, $b_1 = 2.2455$, $b_2 = 3.45$, $k_2 = 1.25$, $k_3 = 1.29$, $c_3 = 2$. In addition, α is the aspect ratio of the ellipsoidal inclusions, equal to 0.03.

The melting in our models is accomplished by using a simple phase diagram for a two-component solid phase, where the solidus and liquidus are approximated by two parallel lines. A similar melting law was introduced by Ribe (1985) and was further explained in Schmeling et al. (2019). For a composition of matrix and melt the concentration of a component B is c^B and if the temperature rises above the solidus temperature, the concentration of B in the fluid, c_f^B , and in the solid, c_s^B , change according to the lever rule. If equilibrium is assumed, the adjusted melt fraction can be calculated with

$$\varphi = \frac{c_s^B - c^B}{c_s^B - c_f^B}. \quad (6.20)$$

In a two-phase flow model, it is assumed that c_s^B and c_f^B are advected separately with their according velocities. This might lead to thermodynamic disequilibrium; the melt fraction is then adjusted with the melting rate, given by

$$\frac{\Gamma}{\rho_0} = \frac{\varphi \frac{D^f c_f^B}{Dt} + (1 - \varphi) \frac{D^s c_s^B}{Dt}}{\Delta c}. \quad (6.21)$$

The operators $\frac{D^f}{Dt}$ and $\frac{D^s}{Dt}$ are the substantial time derivatives equal to $\frac{\partial}{\partial t} + \vec{v}_f \cdot \vec{\nabla}$ and $\frac{\partial}{\partial t} + \vec{v}_s \cdot \vec{\nabla}$, respectively. The concentration difference Δc is equal to $c_s^B - c_f^B$. Using the concentrations, one can calculate the degree of enrichment or depletion, which is defined as the normalized concentration of the solid as

$$f = \frac{c_s^B}{c_s^B - c_f^B} - c_0^B. \quad (6.22)$$

Please note that $c_s^B - c_f^B$ is constant in our simplified phase diagram. In addition, c_0^B is the initial concentration of component B , and $f > 0$ relates to an enrichment of component B , while $f < 0$ relates to a depletion of component B .

6.3.2 Equations for Trace Element Transport

The equations for the transport of trace elements are similar to Eq. (6.1) and Eq. (6.2), but the source term on the right side needs to be adapted to describe the behavior of compatible or incompatible elements during melting. Whether an element tends to stay in or to leave the solid is described by a partition coefficient K_d , which is the ratio of the solid to fluid concentration of a trace element in geochemical equilibrium:

$$K_d = \frac{c_s^T}{c_f^T}. \quad (6.23)$$

Here, c_s^T and c_f^T are the concentrations of a trace element T in solid and fluid, respectively. If K_d is greater than 1, the element tends to stay in the solid (compatible element) and if K_d is smaller than 1, it leaves the solid as soon as possible (incompatible element). For modeling, it is assumed that trace elements in a produced melt increment are in equilibrium with the solid they originated from and that the bulk partition coefficient, $D = \sum_{j=1}^N x_j K_{d,j}$, can be used to apply this behavior to the source term on the right of the equations. N is the number of minerals in a bulk rock and D , as well as K_D , are values for a certain trace element. This leads to

$$\frac{\partial m_s^T}{\partial t} + \vec{\nabla} \cdot (\vec{v}_s m_s^T) = -\frac{\Gamma m_s^T}{D \rho_s (1 - \varphi)} + \frac{1}{t_r} \frac{D m_f^T (1 - \varphi) - m_s^T \varphi}{\varphi + D (1 - \varphi)} \quad (6.24)$$

and

$$\frac{\partial m_f^T}{\partial t} + \vec{\nabla} \cdot (\vec{v}_f m_f^T) = \frac{\Gamma m_s^T}{D \rho_s (1 - \varphi)} - \frac{1}{t_r} \frac{D m_f^T (1 - \varphi) - m_s^T \varphi}{\varphi + D (1 - \varphi)}. \quad (6.25)$$

m_s^T and m_f^T are the trace element mass per volume of element T equal to $c_s^T (1 - \varphi) \rho_s$ and $c_f^T \varphi \rho_f$, respectively. The concentrations c_s^T and c_f^T are defined as the mass of the trace element per total phase mass. In addition to the first term on the right sides, which describe the element exchange due to melting, a second term is added that describes the re-equilibration with time. The control parameter is t_r , corresponding to the reaction time. The term is derived using the assumption that equilibrium can be achieved by exchanging mass between the solid and fluid. Under this assumption, the equation

$$\frac{(m_s^T + \Delta m) \varphi}{(m_f^T - \Delta m) (1 - \varphi)} = D \quad (6.26)$$

should be always fulfilled. Δm is the trace element mass per volume that is exchanged to achieve full geochemical equilibrium. Solving for Δm leads to

$$\Delta m = \frac{D m_f^T (1 - \varphi) - m_s^T \varphi}{\varphi + D (1 - \varphi)}, \quad (6.27)$$

which together with t_r can be used as a re-equilibration term. Solving this term numerically with time steps much smaller than t_r leads to an approach to equilibrium by a factor $1/e$ at $t = t_r$. With a sufficiently small time step, the solution of this term is done iteratively.

During freezing, the first terms on the right sides need to be changed as (for example) an incompatible element now tends to stay in the melt and is not segregated to the other phase. The resulting equations are

$$\frac{\partial m_s^T}{\partial t} + \vec{\nabla} \cdot (\vec{v}_s m_s^T) = -\frac{\Gamma D m_f^T}{\rho_f \varphi} + \frac{1}{t_r} \frac{D m_f^T (1 - \varphi) - m_s^T \varphi}{\varphi + D (1 - \varphi)} \quad (6.28)$$

and

$$\frac{\partial m_f^T}{\partial t} + \vec{\nabla} \cdot (\vec{v}_f m_f^T) = \frac{\Gamma D m_f^T}{\rho_f \varphi} - \frac{1}{t_r} \frac{D m_f^T (1 - \varphi) - m_s^T \varphi}{\varphi + D(1 - \varphi)}. \quad (6.29)$$

As the first terms in Eq. (6.24) and Eq. (6.25) are derived using equilibrium during melting, the same operation can be carried out for freezing. Using $D = c_s^T/c_f^T$, a produced solid trace element concentration in equilibrium, originating from a fluid, can be calculated with

$$c_s^T = \frac{D m_f^T}{\rho_f \varphi}. \quad (6.30)$$

Together with the mass production rate Γ , this equation can be used to give the first term on the right sides in Eq. (6.28) and Eq. (6.29). The terms in the melting equations are derived accordingly.

The equations shown here are based on Spiegelman (1996) but are extended for freezing and re-equilibration and stated in terms of the trace element mass per volume, as they are easier to handle during freezing this way.

To verify the validity of these equations, they can be solved for a simple 0D problem, where the advection term is neglected. A constant melt generation rate is assumed that leads to a melt fraction of 100% at $t = 1$. The resulting concentrations can be compared to literature equations. In general, two end-members are described for melting and freezing. During fractional melting or crystallization, the product is instantly removed from the residuum and is therefore not in geochemical equilibrium. In the equilibrium or batch melting/crystallization case, the solid and melt are assumed to always be in equilibrium. In Eqs. (6.24), (6.25) and (6.28) to (6.29), this behavior is controlled by the reaction time t_r . For $t_r = \infty$, the phase mixture is not able to achieve equilibrium, and the results are comparable to the fractional cases. The relation $t_r = 0$ is from a physical point of view not realistic but can be numerically used to represent full equilibrium. The numerical time step has to be much smaller than t_r ; this can be achieved by using Eq. (6.27). For intermediate cases, t_r is given in terms of the time over which melting/freezing takes place. The re-equilibration term needs to be iterated using much smaller time steps than t_r . The literature equations can be taken from, e.g., Rollinson (1993). The fluid and solid concentrations in the case of batch melting are given by

$$\frac{c_f}{c_0} = \frac{1}{D + F(1 - D)}, \quad (6.31)$$

$$\frac{c_s}{c_0} = \frac{D}{D + F(1 - D)}. \quad (6.32)$$

For the case of fractional melting, the fluid concentration of a melt increment and the accumulated melt can be calculated. The numerical results give the accumulated fluid concentration, the literature equation is given by

$$\frac{\bar{c}_f}{c_0} = \frac{1}{F} \left(1 - (1 - F)^{1/D} \right), \quad (6.33)$$

and the solid concentration is given by

$$\frac{c_s}{c_0} = (1 - F)^{1/D-1}. \quad (6.34)$$

Equilibrium crystallization is described by the same equations as the ones for batch melting. The accumulated solid concentration during fractional crystallization can be calculated using

$$\frac{\bar{c}_s}{c_0} = \frac{1 - F^D}{1 - F} \quad (6.35)$$

and the fluid concentration is given by

$$\frac{c_f}{c_0} = F^{D-1}. \quad (6.36)$$

Fig. 6.1 shows the comparison of numerical to literature equations for $D = 0.1$ and a variety of t_r values. As predicted, the $t_r = \infty$ case exactly follows the fractional lines, and the $t_r = 0$ case follows the equilibrium lines. In fact, the fractional melting and freezing literature equations can be directly derived analytically from Eqs. 6.24, 6.25, 6.28 and 6.29 with $t_r = 0$. The intermediate cases lie between the two end members. It can be seen that, especially for the solid concentrations, the degree of re-equilibration has a large influence. For larger melt fractions, concentrations vary by an order of magnitude for different reaction times. The influence on fluid concentration is not as large but still significant. During freezing, the differences become larger for low melt fractions.

6.3.3 Model Setup

The model consists of a nondimensional 1×1 box with constant nondimensional temperature at the top ($T' = 0$) and at the bottom ($T' = 1.5$) and a linear increase in between. A sinusoidal perturbation of the form $\Delta T = 0.01 \cdot \sin(z'\pi) \cdot \sin(x'\pi)$ is added to the linear temperature field in order to initialize a first plume in the center of the model. On the left and right, mirroring boundary conditions are applied. Free slip is assumed at all boundaries. The shear and volume viscosity depend on the temperature and melt fraction and are calculated using Eq. (6.18) and Eq. (6.19) with η_0 equal to 10^{21} Pa s. To use this law, the nondimensional temperature is scaled with $T_{sc} = 1000^\circ\text{C}$.

The initial density of the material is $\rho' = 1$. The melt and enrichment density are $\rho'_f = 0.8485$ and $\rho'_e = 0.9091$. Scaled with $\rho_0 = 3300 \frac{\text{kg}}{\text{m}^3}$, these are typical densities for peridotite (Boyd and McCallister, 1976), basaltic melt (Stolper and Walker, 1980) and basalt (Schubert et al., 2001).

The depth-dependent solidus curve is calculated using

$$T_{sol} = 1060^\circ\text{C} + 3.75 \cdot 10^{-3} \frac{^\circ\text{C}}{\text{m}} \cdot z, \quad (6.37)$$

where z is the depth. The liquidus is parallel to the solidus with $\Delta T_{li/so} = 400^\circ\text{C}$. These curves are taken from Katz et al. (2003) for 300 ppm H_2O . L' is equal to 0.64.

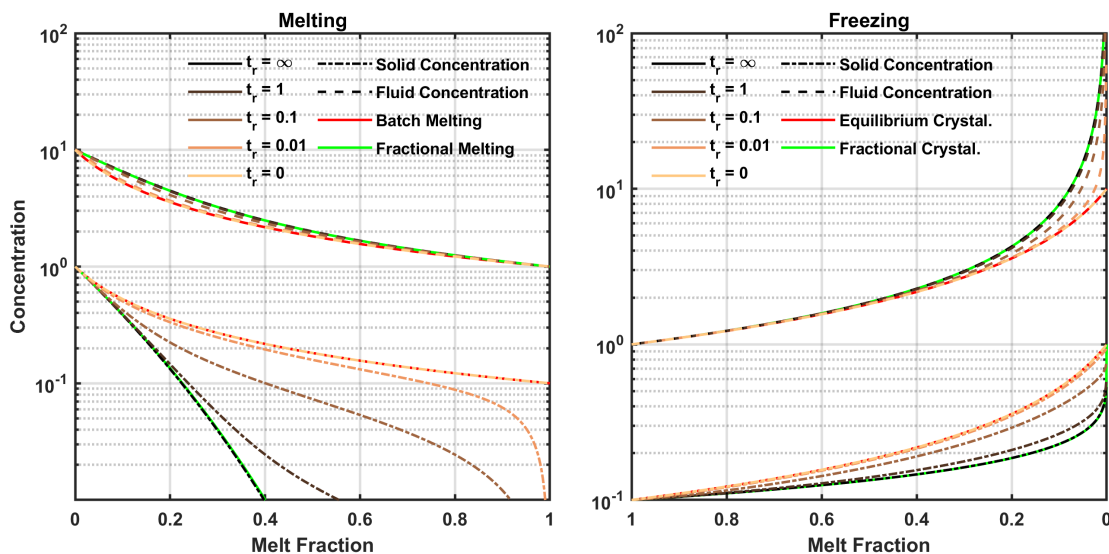


Figure 6.1: Comparison of numerical results to literature equations for fractional and equilibrium melting (left) and freezing (right). The brown lines give the concentrations of the numerical results for a certain reaction time t_r . The dashed-dotted lines give the solid and the dashed line the fluid concentration. The red lines are the literature equations for the equilibrium cases and the green lines give the fractional cases. All results were calculated using $D = 0.1$ and are given normalized to an initial concentration c_0 . Please note that the melt fraction on the right decreases from left to right.

For a possible application at a subduction arc with a height of the box of 120 km, those values represent Rayleigh numbers of $Ra = 2138$, $Ra_e = 5184$ and $Ra_m = 8640$. The retention number Rt is varied between 1 and 50. Each model is carried out with two trace elements with a constant partition coefficient of 0.1 and 0.01. The nondimensional reaction time is taken to be ∞ or between 0 and $1.2 \cdot 10^{-3}$.

The equations are solved using finite differences on a 201×201 grid, and the numerical strategy for the two-phase flow part is described in Schmeling et al. (2019). For the trace element transport, the advection and source terms are solved separately. Advection is evaluated using a semi-Lagrange approach with 4th-order Runge-Kutta solution on a four-times-finer grid. The Courant criteria is no longer fulfilled, but instabilities with the semi-Lagrange approach are no problem. Such a fine grid violates the Courant criteria but minimizes numerical diffusion. The source term is solved explicitly on a broader grid and then interpolated to the fine grid, leading to numerical diffusion in regions where the source term is not zero (i.e. inside the partially molten plume). As this region is just a relatively small part within the model, the advantages of a finer grid predominate over the disadvantages of the necessity to interpolate between the grids.

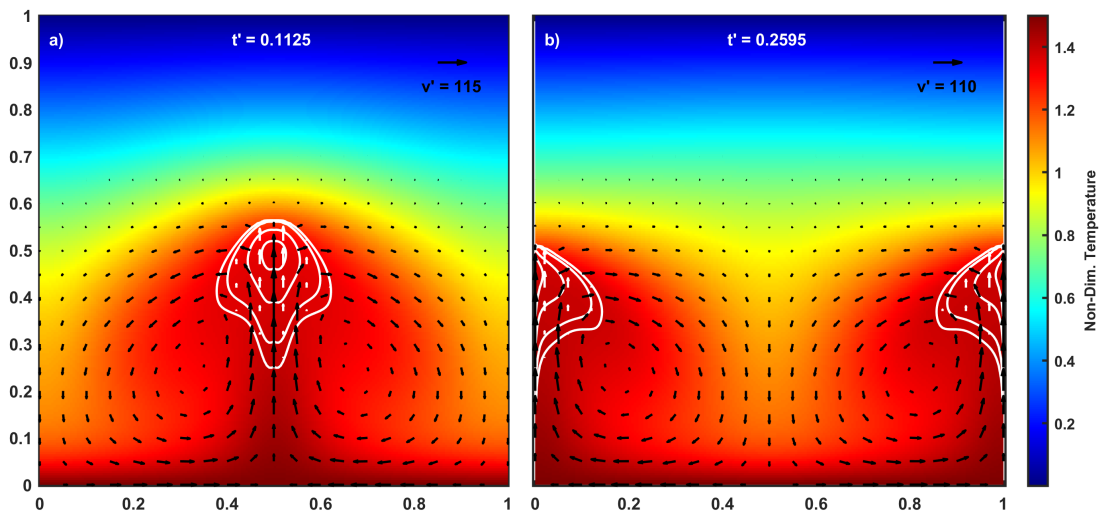


Figure 6.2: Typical model states of an uprising partially molten plume in a model with $Rt = 1$ at a) $t' = 0.1125$ and b) $t' = 0.2595$. The background gives the nondimensional temperature. White contour lines give melt fractions of 0.01, 0.03, 0.06, 0.08, from outside to inside. Black and white vector fields show solid and segregation velocity, respectively. In the upper right corner, a reference arrow is shown.

6.4 Results

After the model is initiated, hot material ascends in the box's center (Fig. 6.2a) and melts partially as the temperature crosses the solidus curve. Two convection cells build up with cool, descending plumes at the model box's sides. The viscosity in the upper 30% of the model is too high to allow for visible movement, but as the partially molten plume rises, it is able to pierce into this highly viscous layer because the shear and volume viscosity decrease strongly with increasing melt fraction. However, the plume is not able to reach the very top of the model, and the partially molten plume decelerates until it finally disappears completely and the melt is no longer present. During this process, the melt, which is enriched in the major element B , percolates and freezes, leading to an enriched solid above the decelerating plume. As this enriched material has a lower density, it stratifies to some degree in the high viscous layer at the top. Due to strong convection caused by the highly buoyant melt, however, some of that material is subducted again. As the melt fraction and melt's buoyancy decreases, convection weakens, and the buoyancy of enriched, less dense material at the flanks of the model counteracts the buoyancy in the center, which is now mainly due to thermal expansion. The direction of convection changes to the opposite direction. Hot material ascends at the box's sides and descends in the center of the model (Fig. 6.2b). This behavior is also called lava-lamp mode convection (e.g. McNutt, 1999; Davaille, 1999). In the model shown in Fig. 6.2 with $Rt = 1$, a reversal takes place every 5–6 overturns and is accompanied by one melting event with melt fractions of up to 12%. Each of these events leads to an enrichment in major and trace elements in the upper, highly viscous layer.

In Fig. 6.3a-c, a rising plume and the accumulation of trace elements at the top

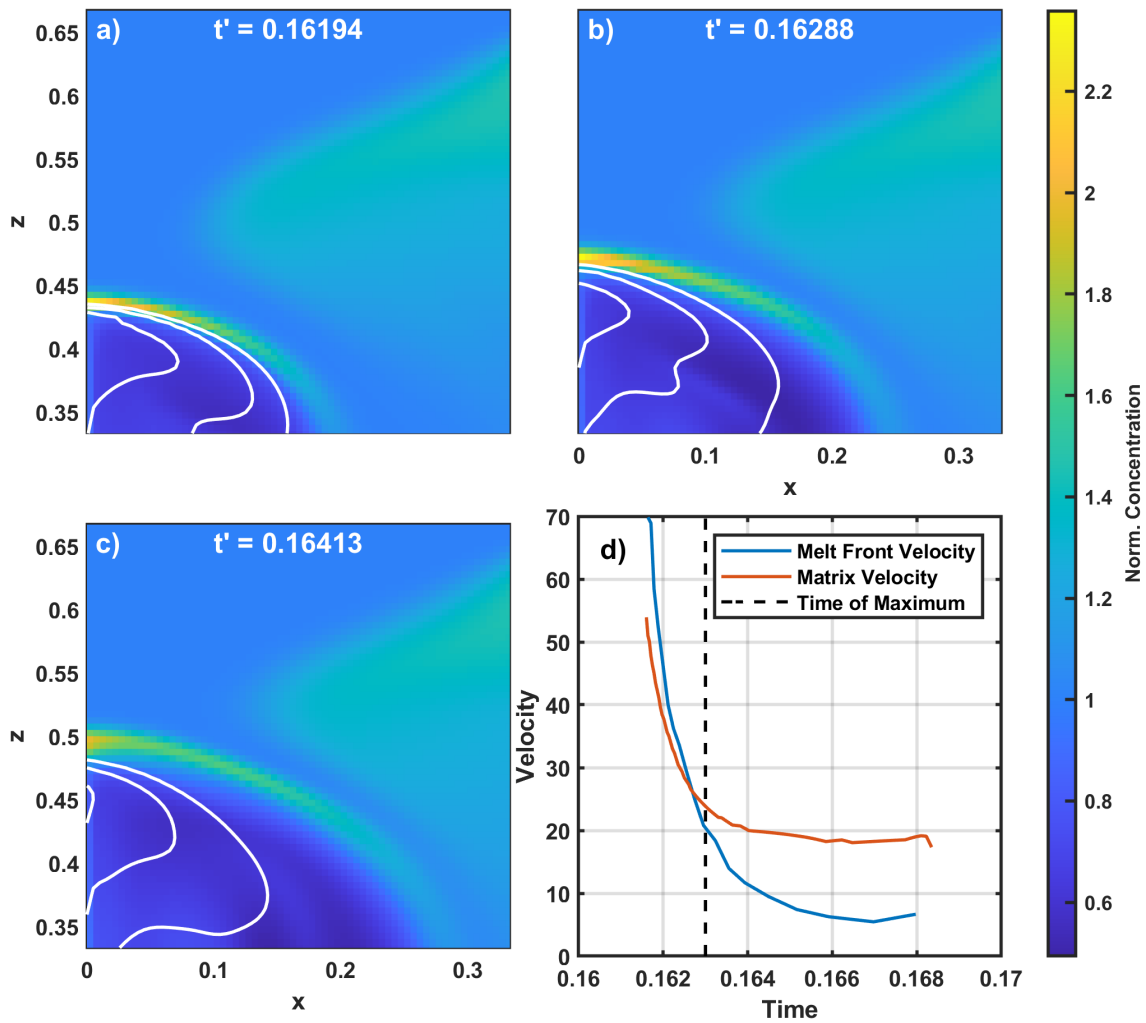


Figure 6.3: Three time steps of the trace element concentration (background color) in a rising plume. The time steps are a) shortly before the matrix overtakes the melt front, b) approximately at the time of overtake, and c) after the overtake. The white contour lines give melt fraction at 0.04, 0.08 and 0.12. d) gives the melt front velocity (blue) at the boundary of the model and the matrix velocity (red) at the same point. The dashed line shows the time at which the maximum concentration is reached. Pictures are from a model with $Rt = 1$ and $t_r = \infty$.

is shown. To understand how enriched material accumulates in the upper part of a partially molten plume and how it eventually freezes, leading to enriched solid material, it might be helpful to look at how fast the solid matrix moves compared to the front of the partially molten plume. Fig. 6.3d shows the velocity of the melt front and the matrix velocity exactly at that front. As long as the front ascends faster than the matrix (Fig. 6.3a-b), new untouched material remains molten, incompatible trace elements are accumulated at the top of the plume, and the enrichment increases. At some point ($t' \approx 0.163$), the matrix becomes faster than the melt front (Fig. 6.3b-c)

and the enriched layer still rises, while the partially molten plume is left behind, still slowly ascending. At this point, the enrichment does not increase any further, and the maximum value is reached. Even though the fluid is still moving faster than the matrix, the constant competition between freezing and decompaction leads to a decelerating melt front. In a nonfreezing model, the partially molten region typically ascends until it reaches an impermeable overburden, constantly driven by decompaction and compaction. In the model, unmolten material is typically completely impermeable, but to allow for the melt to penetrate into this material, we apply a very small background permeability. In some special cases, such a partially molten region can create a solitary wave (e.g. Scott and Stevenson, 1984; Dohmen and Schmeling, 2021), but due to the decreasing temperature to the top, freezing becomes stronger, and the viscosity increases, leading to less intense decompaction. The enriched, now solid, layer ascends upwards until the viscosity becomes too high to allow continued movement. In this model the maximum enrichment decreases due to numerical diffusion, but the enriched layer stays intact and remains in place.

The white lines in Fig. 6.3a-c are melt fraction contour lines that exhibit deformation due to the change in the solidus and liquidus following enrichment and depletion of major elements. The pictures shown here are taken from a second melting event; the material is already depleted and has re-entered the convection cell, leading to regions of higher and lower melt fraction within the rising plume.

In Fig. 6.4 trace element concentrations of a typical model with $Rt = 1$ is shown. Each panel gives the total concentration redistribution of a trace element with $D = 0.01$, each after a melting event. Shortly after model initiation, the first partially molten plume ascends in the center of the model (Fig. 6.4a). Once the plume has reached its maximum ascension height of approximately 0.725 and the material is enriched in trace elements to a value of 8 times the initial concentration, the molten plume retreats, impaired by the reversal of the convection cells. For $D = 0.1$ (not shown here) the enrichment is approximately 5 times the initial concentration. While most of the enriched material remains stagnant at the top, some of the material is reintroduced into the convection cell, reducing the total degree of enrichment in the horizontal layer. During one melting event, meaning the time between first and last occurrence of the melt, the convection layer in the lower part of the model undergoes approximately 5 to 6 overturns, which constantly reintroduces already-depleted or -enriched material back into the molten plume. One result of this behavior can be observed in the center of the enriched layer, where the concentration is slightly lower than to the left and right. During convection, some of the enriched material is traveling down and is then brought to the center of the model, where it ascends again. At this stagnation point, the local enrichment, surrounded by depleted material, raises the solidus, leading to lower melt fractions and eventually to lower enrichment.

As already mentioned, the convection cell changes its direction of rotation, leading to a period of time with no melt at all in the model. Plumes then rise at the left and right boundary of the model, resulting in an enriched layer, slightly lower than the previous one. After this melting event, the convection cell changes its direction of rotation again, and a partially molten plume enriches the already enriched area in the center. The plume again rises slightly lower than the previous ones, and a second

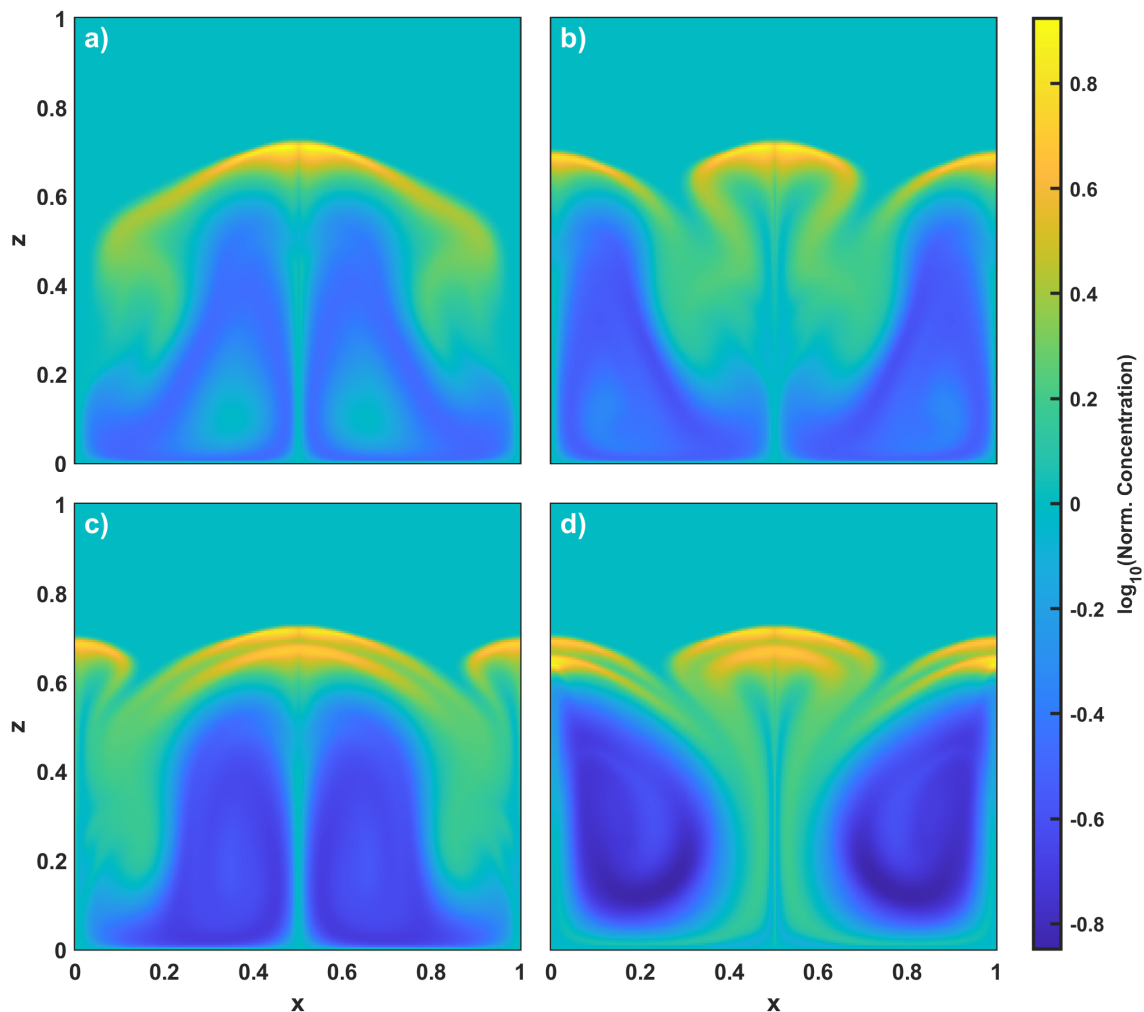


Figure 6.4: Logarithmic total concentrations of a model with $Rt = 1$ and $t_r = \infty$ after four (a-d) different melting events; no melt is present at those times. The initial concentration of the whole model is 1. All pictures are from shortly after a melting event.

enriched layer arises just below the first one. While this does not further increase the maximum enrichment, it enriches the vertical mean concentration (Fig. 6.6a) and therefore the total redistribution of trace elements into a narrow enriched horizontal layer, resulting in a larger depleted convection layer below. After the fourth melting event, additional enriched layers below the first ones at the boundaries of the model are added.

The general behavior of the 2D model can be described by a 0D model, whose general idea is sketched in Fig. 6.5. It is divided into two regions where two different processes take place. Region I is the convection source region where melting takes place up to a certain melt fraction φ_{max} . It is subdivided into a solid (Ia) and a partially molten part (Ib), the rising plume. The whole region I is constantly convection and remixing

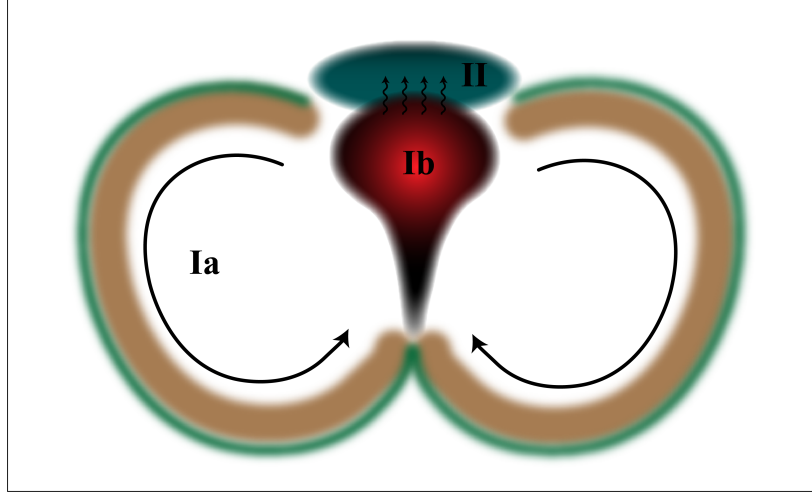


Figure 6.5: Conceptual sketch of a 0D model representing trace element redistribution in a closed convection system. The model is divided into a convection source region (I) and an emplacement zone (II). The source region is further divided into a solid (Ia) and partially molten plume part (Ib). Green depicts enriched material, while brown depicts depleted material.

the material, assuming homogeneous distribution of trace elements. The processes in Ib are described by Eq. (6.24) and Eq. (6.25) in 0D, which become

$$\frac{\partial m_s^T}{\partial t} = -\frac{\Gamma m_s^T}{D\rho_s(1-\varphi)} + \frac{1}{t_r} \frac{Dm_f^T(1-\varphi) - m_s^T\varphi}{\varphi + D(1-\varphi)} \quad (6.38)$$

for the solid. And

$$\frac{\partial m_f^T}{\partial t} = \frac{\Gamma m_s^T}{D\rho_s(1-\varphi)} - \frac{1}{t_r} \frac{Dm_f^T(1-\varphi) - m_s^T\varphi}{\varphi + D(1-\varphi)}. \quad (6.39)$$

for the fluid.

In region II, the emplacement zone, the melt freezes to $\varphi = 0$, leading to enrichment in incompatible trace elements. Here, Eq. (6.28) and Eq. (6.29) in 0D become

$$\frac{\partial m_s^T}{\partial t} = -\frac{\Gamma Dm_f^T}{\rho_f\varphi} + \frac{1}{t_r} \frac{Dm_f^T(1-\varphi) - m_s^T\varphi}{\varphi + D(1-\varphi)} \quad (6.40)$$

and

$$\frac{\partial m_f^T}{\partial t} = \frac{\Gamma Dm_f^T}{\rho_f\varphi} - \frac{1}{t_r} \frac{Dm_f^T(1-\varphi) - m_s^T\varphi}{\varphi + D(1-\varphi)}. \quad (6.41)$$

For simplification reasons, the processes in I and II do not take place simultaneously but one after another. That is, the melt is produced in I and is then transported, as a single unit, to II, where it freezes again. During both these processes, re-equilibration takes place according to t_r . Additionally, three further parameters, namely, the melt fraction φ_{max} and the geochemical parameters D and t_r , are introduced to cover the

dynamics of the system:

Melt area ratio If material in region I is molten, the concentrations calculated with the equations represent only region Ib and not the whole source region I. Therefore, after the first melt event has taken place, the concentration of the source region is not equal to the concentration calculated in Ib but to the concentrations of Ia and Ib combined. For simplification, it is assumed that Ib becomes fully depleted after each melting event, which is reasonable for small D and relatively large φ_{max} . The initial concentration for the melting is then calculated using $c_0 = R_{MA}^{k-1}$, where k is the number of the melting event and R_{MA} is the *melt area ratio*, which represents the ratio of the area of Ia to I.

Transport ratio The melt that is produced in the source region is not fully transported to the emplacement zone. Some of it freezes at depths that are too deep to allow storage. This material is then transported with the convection, subducted and eventually reintroduced back into the melting region (green material in region Ia of Fig. 6.5). Therefore, the trace element mass that arrives in the emplacement zone (II) is not equal to the one calculated during melting in Ib, but to $R_{TP} \cdot m_f^T$, where m_f^T is the trace element mass per volume in the fluid calculated in Ib and R_{TP} is the *transport ratio*, which is the ratio of the melt amount that is transported to II to the melt amount produced in Ib.

Emplacement volume ratio The melt from the source region that arrives in the emplacement zone is stored in just a very small area above the plume, compared to the whole plume. Therefore, trace elements are accumulated, leading to local higher concentrations, while the trace element mass is kept constant. The concentration of the fluid is multiplied with the emplacement volume ratio, R_{EV} , to account for this compression. R_{EV} is the ratio of the area of Ib to that of II.

The whole model can be summarized in the following steps:

1. Melting in region I
 - (a) Calculate the initial solid concentration (R_{MA})
 - (b) Calculate the fluid (Eq. (6.39)) and solid concentration (Eq. (6.38)) until $\varphi = \varphi_{max}$
2. Freezing in region II
 - (a) Calculate the amount of trace elements that arrives in the emplacement zone (R_{TP})
 - (b) Account for compression into a smaller volume (R_{EV})
 - (c) Calculate the solid (Eq. (6.40)) and fluid concentration (Eq. (6.41)) until $\varphi = 0$

Those two steps have to be repeated for each melting event.

To compare the results of the 2D to the 0D model, horizontally averaged vertical

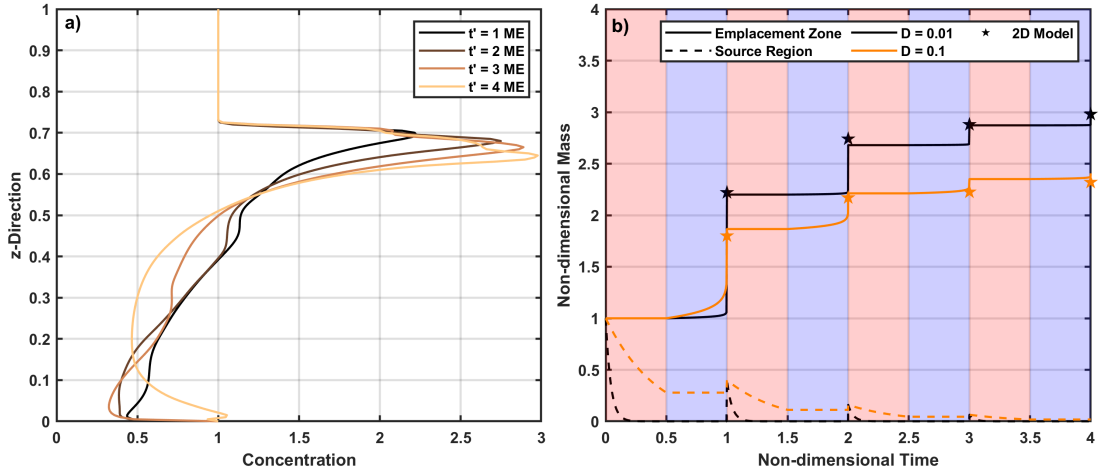


Figure 6.6: In a) horizontally averaged vertical profiles of the total concentration after four different melting events are shown of a 2D model with $Rt = 10$, $t_r = \infty$ and $D = 0.01$. b) compares the 2D model results with a 0D model. A time of 1 means one melting event has happened. The stars give the maximum concentration of the 2D model for $D = 0.01$ (black) and $D = 0.1$ (orange). Solid lines give 0D model concentrations of the solid in the emplacement zone for both D . Dashed lines show the solid concentration of the source region. The background color shows whether melting is taking place in the source region (red) or freezing is taking place in the emplacement zone (blue).

profiles are used after each melting event (Fig. 6.6a). As already mentioned, the total enrichment within the layer increases with every melting event, but the addition to the enrichment also decreases with every event as the source region becomes depleted during this process.

In Fig. 6.6b the two steps of melting and freezing are marked with a red (melting in the source region) and blue (freezing in the emplacement zone) background, respectively, and both steps together take a nondimensional time of $t' = 1$. The figure gives the results for a run with $\varphi_{max} = 0.12$, $t_r = \infty$ and $D = 0.1$ and 0.01 . D and t_r are taken from the 2D model parameters, and φ_{max} is the maximum melt fraction we achieve in the model. The *emplacement volume ratio* is taken to be equal to 3, which is a result from the 2D model as well and in general should be a function of the viscosity law and the model geometry prescribed. The *transport ratio* can be estimated from the result of the first melting event and is taken to be 0.4. This value is a function of the permeability and melt density or Rm and Rt and means that 40% of the trace element mass is transported into the emplacement zone. The last value, the *melt area ratio*, is also taken to be 0.4, which is just a coincidence, as it is not directly related to the *transport ratio*. This value can be estimated from the following melting events and means that the initial trace element concentration of each melting event is just 40% of the previous event. All these values are either estimates from evaluating the 2D model or are chosen just to fit the results. The 2D model it is compared to uses

$Rt = 1$ and the same parameters describing the trace elements.

The same fitting can be repeated for a model with different Rt . Changing Rt in a model strongly influences the melt fractions. While $Rt = 1$ leads to $\varphi_{max} = 0.12$, $Rt = 5$ leads to $\varphi_{max} = 0.18$. As the retention number gives the resistance of the melt to percolate through a matrix, a higher value refers to less effective separation between solid and melt. Therefore, in the 0D-model, the *transport ratio* needs to be adjusted to a lower value. A selection of 0.2 gives a good fit.

All in all, there are 6 parameters that need to be fitted or chosen, but the results from the 0D and 2D model can be fitted by a simple equation with just two variables of the form

$$c_s = c_{asy} \cdot (1 - e^{-\gamma n_{me}}) + 1. \quad (6.42)$$

Here c_{asy} is the increase from the source material (i.e., $c_0 = 1$) to the asymptotic value of c_s , γ is the decay rate of the growth and n_{me} is the number of melt events. Only the *melt area ratio* has an influence on the decay rate, while all other parameters effect the maximum enrichment. In addition, γ is decreased with higher *melt area ratio*, leading to a slower increase and more melting events necessary to approach the asymptotic value. Decreasing the partition coefficient sharply increases c_{asy} , and increasing any of the *transport*, *depletion* and *emplacement volume ratios* increases the asymptotic value linearly. Consequently, doubling these ratios lead to a doubling of c_{asy} . The maximum degree of melting has an influence, as long as it is smaller or in the order of D . Highly incompatible elements completely enter the melt for already small melt degrees. Therefore, it is irrelevant how high the degree of melting is after it has reached this certain threshold value, as nearly all trace elements are already in the melt. The 2D models that are used to compare to the 0D model do not allow for re-equilibration, but we can still obtain results by giving a finite t_r in the conceptual model, leading to a decrease in c_{asy} for stronger re-equilibration.

For example, the model in Fig. 6.6 with $Rt = 10$ leads to $c_{asy} = 2$ and $\gamma = 0.9163$, while the model with $Rt = 5$ leads to $c_{asy} = 0.8626$ and the same γ .

In Fig. 6.7, the effect of Rt and t_r on the redistribution is shown. The retention number has a large influence, as it not only changes the maximum enrichment but also changes the dynamics of the model and leads to different emplacement depths. Allowing for two-phase flow strongly reduces the maximum melt fraction, and reducing Rt leads to even lower fractions. The viscosity law used causes a rapid decrease in viscosity for already low melt fractions, and reducing the retention number and ultimately the melt porosity leads to much higher viscosity within the partially molten plume, making penetration more difficult into the highly viscous overburden. Therefore, stronger segregation (low Rt) leads to less highly elevated enrichment but nevertheless causes higher degrees of enrichment. While the depth of maximum concentration might be similar, the maximum elevation of enriched material and the thickness of the enriched layer increases with decreasing Rt . Decreasing the retention number from 10 to 5 approximately doubles the degree of enrichment. Reducing it further from 5 to 1 leads to a similar increase.

Re-equilibration has an influence not on the dynamics but on the degree of enrichment. With full non-equilibrium (i.e., $t'_r = \infty$) the highest degree of enrichment

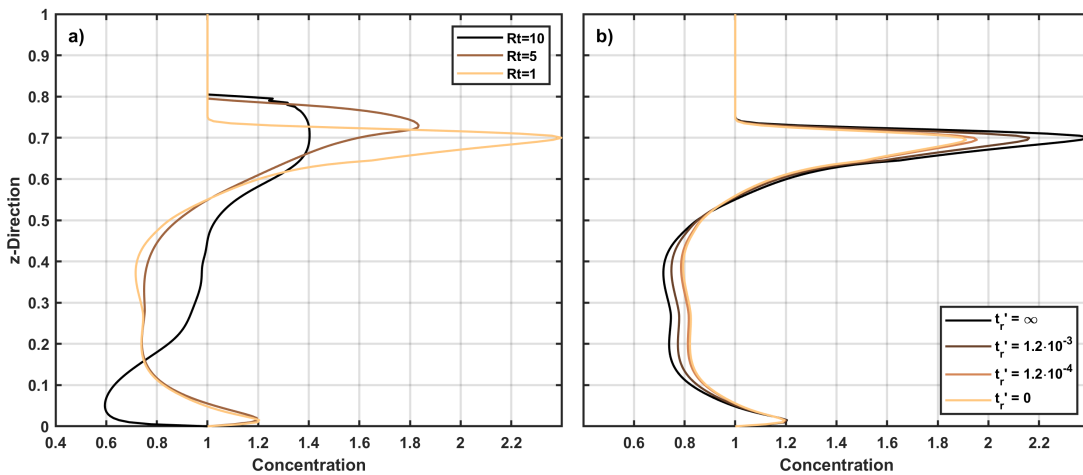


Figure 6.7: Horizontally averaged vertical profiles of 2D models with a) different retention numbers, Rt , and b) different reaction times, t_r . Both model series are carried out using $D = 0.01$. In a), all models are carried out with $t_r = \infty$ and in b), all models are carried out with $Rt = 1$. All profiles are taken shortly after the first melting event.

with 1.4 is reached. This is the same model as $Rt = 1$ in Fig. 6.7a. Allowing for re-equilibration leads to smaller concentrations, and $t_r = 0$ refers to instantaneous re-equilibration. In that case, the maximum degree of enrichment is decreased by 35% to 0.9. Re-equilibration takes place only as long as the melt is present. Once the enriched material leaves the partially molten plume, there is no exchange possible, and concentrations stay untouched until they are remelted. However, during the rise of a plume, constant exchange of trace elements between the solid and fluid is taking place and shorter reaction times have a large influence. All in all, re-equilibration becomes more important the longer the melting event lasts.

The Damköhler number Da can be used to represent the amount of re-equilibration taking place during advection. The nondimensional number is the ratio of the reaction rate to the advective mass transport rate (Spiegelman et al., 2001) and can be also stated in terms of time, where Da is equal to the advective time scale over reaction time. The advective time scale can be stated as the time the fluid melt needs to travel one compaction length, which is a typical length scale in compaction problems (McKenzie, 1984). For $t_r = 0$ (i.e., instantaneous equilibrium), Da becomes infinite. For $t_r = \infty$, Da is 0. In a typical model of ours in a rising plume with melt fractions of approximately 10%, a nondimensional reaction time of $t_r' = 1.2 \cdot 10^{-4}$ equals a Da of approximately 30, and $t_r' = 1.2 \cdot 10^{-3}$ yields $Da \approx 3$. As the compaction length is strongly changing in time and space, it is not suitable to use a constant Da value but rather a constant reaction time.

6.5 Discussion

Choosing the parameters for the conceptual 0D model to fit a certain region inside the Earth can be hard, often even impossible. In that case, 2D models are a good tool to

achieve more insights on the processes in this region. However, some estimates can be carried out. In the case of a mantle wedge, seismic imaging can be helpful to obtain values for the *melt area ratio*. This value is in some way dependent on the ratio of melt region to the whole source region, and from Wiens et al. (2008), one can see that the melt is present in very wide areas from depths of 120 km up to 30 km. The whole source region might be hard to estimate as constantly new material is brought there due to convection, but converted to our model setup, this leads to ratios of approximately 50% or even higher. The *transport ratio* is mainly dependent on the retention number, which is again dependent on permeability of the matrix and fluid viscosity. Basaltic melts usually have viscosities between 10^{-1} and 10^3 Pa s (Best, 2003), but the value can be much higher for other types of melt. The permeability depends on the grain size a , with typical values of $10^{-3} m^2$ (Dannberg et al., 2017) and a geometric factor K of order 100 (McKenzie, 1984) ($k_0 = a^2/K$). For our model setup, we then obtain Rt at values between $1.4 \cdot 10^{-4}$ and 1.4. With $Rt = 1$, which lies just at the upper value, we can fit the results with a *transport ratio* of 0.4. For $Rt = 5$, a value of 0.2 is found. Smaller Rt values, which tend to be more unstable in a model, lead to higher *transport ratios*, but these ratios cannot be larger than 1. The *emplacement volume ratio* depends on the size of the convection cell, which can be very different depending on the area of observation. The emplacement area should be always of a similar order in size. *Emplacement volume ratios* in the order of 1–10 are reasonable. The proposed 2D model setup might be applicable to a volcanic arc of an oceanic lithosphere subducting below another one. Between the two plates, a mantle wedge becomes present, which is the topic of many studies (e.g. van Keken, 2003; Hirth and Kohlstedt, 2003; Grove et al., 2006). Due to dehydration of the subducting slab (e.g. Iwamori, 1998, 2007) the solidus temperature is decreased, and melting occurs, which eventually leads to volcanic eruptions at the volcanic arc. Our model is not able to transport melt to the very surface as it reaches a brittle region, where the melt is usually transported through dykes, which are not covered by our model’s physical description. However, our model is capable of describing the transport of melt from the melt source region to the ductile-brittle boundary, where the melt accumulates, leading to enrichment in trace and major elements. What is usually measured by geochemists are the trace element concentrations in the melt that reaches the top, but those are, among others, a result of the melt degree, partition coefficient and source material concentration. Especially with regards to the melt degree and source material, numerical models can be helpful to achieve better understanding of what is happening. The model used in this work is rather simple and should be adjusted in the future to better reflect nature, but one can already take fluid concentrations out of the model and compare them with real measurements. In Fig. 6.8 melt concentrations are taken out of a first melt event from a model with different Rt and $t'_r = 0$. Partition coefficients are taken from Ayers et al. (1997) and the results are compared to average arc values relative to MORB basalt from McCulloch and Gamble (1991). To compare those values, it is assumed in our model that the whole model starts with trace element concentrations equal to those of MORB. It can be seen that higher retention numbers lead to better fits. Compatible elements in general are not fitted adequately, and changing Rt gives only minor changes. However, incompatible

elements can be fitted quite nicely, and the best fit can be achieved with $Rt = 40$, which is, as shown above, too high. What needs to be addressed is that for our model setup, $Rt = 40$ gives the best results, but different temperature profiles or melting curves also have major influences on the concentrations, which might explain why Rt is so high. Adjusting the model to better represent certain areas would probably give smaller retention numbers.

As already mentioned, in our model, lava-lamp convection is achieved, which leads to trace element enrichment horizontally distributed over the whole model. This is probably not what we would expect below a volcanic arc. One difference in our model compared to nature is that we use a constant depth-dependent solidus and liquidus over the whole model, while in nature, these coexistence curves are strongly dependent on the water content. During subduction, a plate dehydrates in a specific depth, which leads to strongly depressed solidus curves just above this point. It is questionable how the lava-lamp convection would react to this, but melting would most certainly occur above the dehydration point only, even with reversed convection. Therefore, horizontally distributed trace element enrichment is not probable, and the total enrichment would increase slower, as only every other plume would create melt.

To further adjust the model, the model box should be changed, giving a mantle wedge

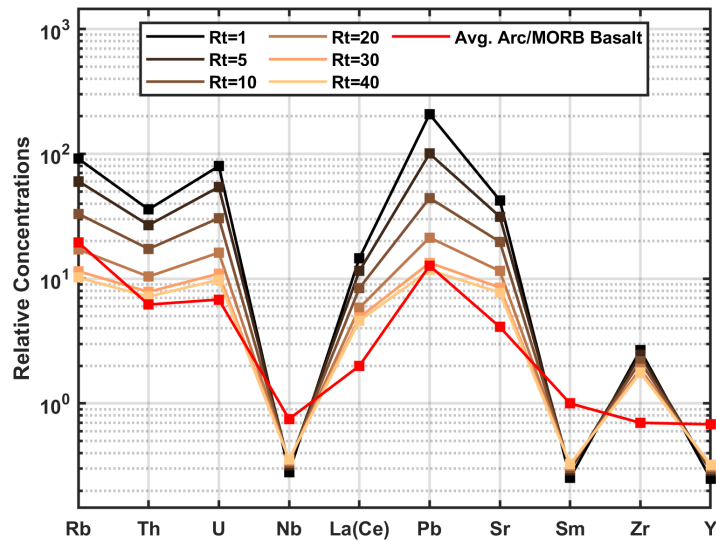


Figure 6.8: Relative concentrations for different trace elements, using partition coefficients from (Ayers et al., 1997), in a model with different Rt and $t'_r = 1 \cdot 10^{-5}$. The fluid concentrations are the maximum value at the time of maximum melt fraction during the first melting event. Brown lines show the 2D model results for different retention numbers. The red line gives the average arc concentration relative to that of MORB basalt from (McCulloch and Gamble, 1991).

with possible inflow from the one side, to allow for constant supply of fertile material. Temperature profiles would have to be adjusted as well to fit the mantle wedge. In a future model, transport of volatiles could be also implemented to allow for consistent

feedback on the solidus. Calculation of partition coefficients, based on the temperature, pressure and composition, are possible with a physical description of our model as an important step.

6.6 Conclusions

Models of various kinds are capable of explaining trace element concentrations of a melt reaching the surface. While some models are rather simple, 2D or even 3D models are helpful to obtain better insights on the processes taking place. In this work, we show that our code is capable of giving a fully consistent redistribution of major and trace elements, including melting, freezing, and re-equilibration of trace elements and transport in 2D. In a simple representation of a volcanic back arc, lava-lamp convection can be observed, and the influence of the retention number and re-equilibration on trace element redistribution are investigated. Different retention numbers not only lead to different degree of enrichment but also change the whole dynamics of the system, allowing for higher emplacement but lower enrichment with low Rt .

A numerical 0D model is introduced that can explain the 2D results for various model parameters, and a simple function can be fitted to reflect it.

In a closed convection system, trace element concentrations reach an asymptotic value that depends on many parameters such as the partition coefficient, re-equilibration, mobility of melt and the ratio of the convection area to the emplacement area. The time or the numbers of melting events that is needed to approach the asymptotic value depends only on how large the partially molten region is compared to the whole convection source region.

References

- Allen, M. B. (1985). Numerical modelling of multiphase flow in porous media. *Adv. Water Resources*, 8(December).
- Ayers, J. C., Dittmer, S. K., and Layne, G. D. (1997). Zone Processes. *Earth and Planetary Science Letters*, 150:381–398.
- Baitsch-Ghirardello, B., Stracke, A., Connolly, J. A., Nikolaeva, K. M., and Gerya, T. V. (2014). Lead transport in intra-oceanic subduction zones: 2D geochemical-thermo-mechanical modeling of isotopic signatures. *Lithos*, 208:265–280.
- Bercovici, D., Ricard, Y., and Schubert, G. (2001). A two-phase model for compaction and damage: 1. General Theory. *Journal of Geophysical Research*, 106(B5):8887.
- Best, M. G. (2003). *Igneous and metamorphic petrology*. Blackwell Science Ltd, New Jersey, 2 edition.
- Bo, T., Katz, R. F., Shorttle, O., and Rudge, J. F. (2018). The Melting Column as a Filter of Mantle Trace-Element Heterogeneity. *Geochemistry, Geophysics, Geosystems*, 19(12):4694–4721.
- Boyd, F. and McCallister, R. (1976). SiO₂ appears to be somewhat below the average Na₂ (Table it to be near pyrolite in composi- Partial fusion experiments Densities of Peridotites SiO Chayes [1969] was used to calculate the modes. *Geophysical Research Letters*, 3(9):509–512.
- Costa, A. (2006). Permeability-porosity relationship: A reexamination of the Kozeny-Carman equation based on a fractal pore-space geometry assumption. *Geophysical Research Letters*, 33(2):1–5.
- Dannberg, J., Eilon, Z., Faul, U., Gassmüller, R., Moulik, P., and Myhill, R. (2017). The importance of grain size to mantle dynamics and seismological observations. *Geochemistry, Geophysics, Geosystems*, 18(8):3034–3061.
- Davaille, A. (1999). Simultaneous generation of hotspots and superwells by convection in a heterogeneous planetary mantle. *Nature*, 402(6763):756–760.
- Dohmen, J. and Schmeling, H. (2021). Magma ascent mechanisms in the transition regime from solitary porosity waves to diapirism. *Solid Earth*, 12:1549–1561.
- Gaetani, G. A. and Grove, T. L. (1998). The influence of water on melting of mantle peridotite. *Contributions to Mineralogy and Petrology*, 131(4):323–346.
- Gast, P. W. (1968). Trace element fractionation and the origin of tholeiitic and alkaline magma types. *Geochimica et Cosmochimica Acta*, 32:1057–1086.
- Grove, T. L., Chatterjee, N., Parman, S. W., and Médard, E. (2006). The influence of H₂O on mantle wedge melting. *Earth and Planetary Science Letters*, 249(1-2):74–89.

- Hirth, G. and Kohlstedt, D. (2003). Rheology of the Upper Mantle and the Mantle Wedge : A View from the Experimentalists. *Geophysical Monograph*, 138:83–106.
- Holness, M. B. and Richter, F. M. (1989). Possible effects of spreading rate on MORB isotopic and rare earth composition arising from melting of a heterogeneous source. *Journal of Geology*, 97(3):247–260.
- Ikemoto, A. and Iwamori, H. (2014). Numerical modeling of trace element transportation in subduction zones: Implications for geofluid processes. *Earth, Planets and Space*, 66(1):1–10.
- Iwamori, H. (1993). Dynamic disequilibrium melting model with porous flow and diffusion-controlled chemical equilibration. *Earth and Planetary Science Letters*.
- Iwamori, H. (1998). Transportation of H₂O and melting in subduction zones. *Earth and Planetary Science Letters*.
- Iwamori, H. (2007). Transportation of H₂O beneath the Japan arcs and its implications for global water circulation. *Chemical Geology*, 239(3-4):182–198.
- Karato, S.-I. and Wu, P. (1993). Rheology the Upper Mantle : Synthesis. *Science*, 260(May).
- Katz, R. F., Spiegelman, M., and Langmuir, C. H. (2003). A new parameterization of hydrous mantle melting. *Geochemistry, Geophysics, Geosystems*, 4(9):1–19.
- Keller, T. and Katz, R. F. (2016). The role of volatiles in reactive melt transport in the asthenosphere. *Journal of Petrology*.
- Keller, T., Katz, R. F., and Hirschmann, M. M. (2017). Volatiles beneath mid-ocean ridges: Deep melting, channelised transport, focusing, and metasomatism. *Earth and Planetary Science Letters*.
- Kimura, J. I. (2017). Modeling chemical geodynamics of subduction zones using the Arc Basalt Simulator version 5. *Geosphere*, 13(4):992–1025.
- Langmuir, C. H., Bender, J. F., Bence, A. E., Hanson, G. N., and Taylor, S. R. (1977). Petrogenesis of basalts from the FAMOUS area: Mid-Atlantic Ridge. *Earth and Planetary Science Letters*, 36(1):133–156.
- McCulloch, M. T. and Gamble, J. A. (1991). Geochemical and geodynamical constraints on subduction zone magmatism. *Earth and Planetary Science Letters*, 102(3-4):358–374.
- McKenzie, D. (1984). The generation and compaction of partially molten rock. *Journal of Petrology*, 25(3):713–765.
- Mckenzie, D. and O’nions, R. K. (1992). Corrections to ‘partial melt distributions from inversion of rare earth element concentrations’. *Journal of Petrology*, 33(6):1453.

- McNutt, M. (1999). The mantle's lava lamp. *Nature*, 402(6763):739–740.
- Plank, T. and Langmuir, C. H. (1992). Effects of the melting regime on the composition of the oceanic crust. *Journal of Geophysical Research*, 97(B13).
- Ribe, N. M. (1985). The generation and composition of partial melts in the earth's mantle. *Earth and Planetary Science Letters*.
- Rollinson, H. R. (1993). *Using Geochemical Data: Evaluation, Presentation, Interpretation*. Pearson Education Limited, Essex, 1st edition.
- Schmeling, H. (2000). *Partial melting and melt segregation in a convecting mantle*. Springer.
- Schmeling, H., Kruse, J. P., and Richard, G. C. (2012). Effective shear and bulk viscosity of partially molten rock based on elastic moduli theory of a fluid filled poroelastic medium. *Geophysical Journal International*, 190(3):1571–1578.
- Schmeling, H., Marquart, G., Weinberg, R., and Wallner, H. (2019). Modelling melting and melt segregation by two-phase flow: New insights into the dynamics of magmatic systems in the continental crust. *Geophysical Journal International*, 217(1):422–450.
- Schubert, G., Turcotte, D. L., and Olson, P. (2001). *Mantle Convection in the Earth and Planets*. Cambridge University Press.
- Scott, D. R. (1988). The competition between percolation and circulation in a deformable porous medium. *Journal of Geophysical Research*, 93(B6):6451–6462.
- Scott, D. R. and Stevenson, D. J. (1984). Magma solitons. *Geophysical Research Letters*, 11(11):1161–1164.
- Scott, D. R. and Stevenson, D. J. (1986). Magma ascent by porous flow. *Journal of Geophysical Research B*, 91(B9):9283.
- Shaw, D. M. (1970). Trace element fractionation during anatexis. *Geochimica et Cosmochimica Acta*, 34(2):237–243.
- Solano, J. M., Jackson, M. D., Sparks, R. S., and Blundy, J. D. (2014). Evolution of major and trace element composition during melt migration through crystalline mush: Implications for chemical differentiation in the crust. *American Journal of Science*, 314(5):895–939.
- Spiegelman, M. (1996). Geochemical consequences of melt transport in 2-D: The sensitivity of trace elements to mantle dynamics. *Earth and Planetary Science Letters*, 139:115–132.
- Spiegelman, M., Kelemen, P. B., and Aharonov, E. (2001). Causes and consequences of flow organization during melt transport: The reaction infiltration instability in compactible media. *Journal of Geophysical Research*, 106:2061–2077.

REFERENCES

- Stolper, E. and Walker, D. (1980). Melt Density and the Average Composition of Basalt. *Contributions to Mineralogy and Petrology*, 74:7–12.
- Turcotte, D. L. and Schubert, G. (2014). *Geodynamics*. Cambridge University Press, 3. edition.
- van Keken, P. E. (2003). The structure and dynamics of the mantle wedge. *Earth and Planetary Science Letters*, 215(3-4):323–338.
- Wiens, D. A., Conder, J. A., and Faul, U. H. (2008). The seismic structure and dynamics of the mantle wedge. *Annual Review of Earth and Planetary Sciences*, 36:421–455.
- Wilson, C. R., Spiegelman, M., van Keken, P. E., and Hacker, B. R. (2014). Fluid flow in subduction zones: The role of solid rheology and compaction pressure. *Earth and Planetary Science Letters*, 401:261–274.

Chapter 7

Unpublished Manuscript

Transport of Volatiles and Trace Elements in Solitary Porosity Waves

Unpublished (2022)

Janik Dohmen¹ & Harro Schmeling¹

¹Institute for Geoscience, Goethe University Frankfurt, Frankfurt, Germany

Abstract

Magmatic phenomena such as volcanic eruptions on the Earth's surface show, among others, that melt is able to ascend from partially molten regions in the Earth's mantle. Thereby it firstly flows through the partially molten source region and then through the unmolten lithosphere until it eventually reaches the surface. The governing processes in this source region are poorly understood. Since McKenzie (1984) introduced his equations for two-phase flow, which include a fluid phase (melt) and a porous deformable matrix, the physics of this region are of broad interest. One of the features which were studied is the emergence of solitary porosity-waves. Using these two-phase flow equations the transport of volatiles and trace elements in ascending magmas is investigated. To do this two additional mass equations for the concentration of a volatile or trace element in the solid and the fluid are solved. The equations assume non-equilibrium, meaning re-equilibration between solid and fluid is not possible. Melting and freezing is not allowed, rather an initial concentration is assumed that is transported with solid and fluid separately.

Before Jordan et al. (2018) showed that solitary porosity waves are able to transport mass within its center it was thought that mass is just passed through these waves. Our models can reproduce the outcomes of Jordan et al. (2018) using a full two-phase flow approach which allows for self consistently evolving porosity waves. They show that material slightly above the original melt source region gets captured within the waves, as it needs some time to evolve from an arbitrary melt perturbation.

7.1 Introduction

Shortly after McKenzie (1984) published his equations describing the movement of melt and matrix of a partially molten system it was shown that these equations are capable of producing solitary porosity waves (e.g. Scott and Stevenson, 1984; Barcilon and Richter, 1986; Scott and Stevenson, 1986; Barcilon and Lovera, 1989). These waves are regions of higher melt porosity that ascend with constant velocity and in constant shape through a constant partially molten background. Their ascent is controlled by decompaction of the matrix in front of the wave and compaction behind it. Until today solitary porosity waves are of interest to the community and are still not fully understood (e.g. Dohmen et al., 2019; Dohmen and Schmeling, 2021; Omlin et al., 2018; Stubblefield et al., 2020; Yarushina et al., 2015). For a long time it was thought that these waves are not able to transport mass because they migrate faster upwards than the segregating melt within the wave (Watson and Spiegelman, 1994). While this is true for solitary waves in 1D models it is not always the case in 2D. Jordan et al. (2018) showed that for waves that are faster than three times the background velocity a recirculating area within the wave builds up that is completely separated from its surroundings. Material that is encapsulated in this area circulates and has effectively higher velocities than the wave itself.

7.2 Governing Equations

The equations shown here describe a two-phase system, based on McKenzie (1984) and Schmeling (2000) and are slightly simplified for the purpose of modeling solitary porosity waves. More insights on these equations can be found in Dohmen et al. (2019) and Dohmen and Schmeling (2021). Here we show the already non-dimensionalized equations using the background compaction length δ_{c0} and the background fluid velocity v_{sc} . The compaction length is given by

$$\delta_c = \sqrt{\frac{\xi + \frac{4}{3}\eta}{\mu} k_\varphi} \quad (7.1)$$

where ξ is the volume viscosity, η the shear viscosity, μ the viscosity of the fluid and k_φ the melt fraction dependent permeability. The permeability is given by

$$k_\varphi = k_0 \varphi^n. \quad (7.2)$$

φ is the volumetric melt fraction and n a power law exponent equal to 2 or 3. The compaction length is a length scale naturally emerging from the equations.

The scaling velocity is given by

$$v_{sc} = \frac{k_\varphi}{\mu \varphi} \Delta \rho g. \quad (7.3)$$

$\Delta \rho$ is the difference between solid and fluid density and g is the gravitational acceleration.

It is common to non-dimensionalize the melt fraction by the background melt fraction φ_0 . Shear and volume viscosity are normalized by the intrinsic shear viscosity η_0 . The viscosities are calculated using simple laws

$$\eta = \eta_0 (1 - \varphi), \quad (7.4)$$

$$\xi = \eta_0 \frac{1 - \varphi}{\varphi}. \quad (7.5)$$

With all these parameters we arrive for the mass conservation of the melt at

$$\frac{\partial \varphi}{\partial t} + \vec{\nabla} \cdot (\varphi \vec{v}_f) = 0 \quad (7.6)$$

and for the solid at

$$\frac{\partial (1 - \varphi)}{\partial t} + \vec{\nabla} \cdot ((1 - \varphi) \vec{v}_s) = 0. \quad (7.7)$$

\vec{v}_s and \vec{v}_f are the solid and fluid velocity, respectively. The right-hand side of these equations is equal to zero because we do not allow for melting or freezing.

For the momentum conservation of the melt we achieve

$$\vec{v}_f - \vec{v}_s = \varphi^{n-1} \left[(1 - \varphi_0 \varphi) \vec{e}_z - \frac{\eta_0}{\xi_0 + \frac{4}{3}\eta_0} \frac{1}{\varphi_0} \frac{\partial \tau_{ij}}{\partial x_j} \right] \quad (7.8)$$

with

$$\tau_{ij} = \eta \left(\frac{\partial v_{si}}{\partial x_j} + \frac{\partial v_{sj}}{\partial x_i} \right) + \delta_{ij} \left(\xi - \frac{2}{3}\eta \right) \vec{\nabla} \cdot \vec{v}_s. \quad (7.9)$$

Here, τ_{ij} is the effective viscous stress tensor of the matrix and δ_{ij} is the Kronecker delta.

The momentum conservation of the solid becomes

$$\left(\frac{\partial^2}{\partial x^2} - \frac{\partial^2}{\partial z^2} \right) \left[\eta \left(\frac{\partial^2 \psi}{\partial x^2} - \frac{\partial^2 \psi}{\partial z^2} \right) \right] + 4 \frac{\partial^2}{\partial x \partial z} \left[\eta \frac{\partial^2 \psi}{\partial x \partial z} \right] = \varphi_0^2 \frac{\xi_0 + \frac{4}{3}\eta_0}{\eta_0} \frac{\partial \varphi}{\partial x} + A(\chi) \quad (7.10)$$

with

$$A(\chi) = -2 \frac{\partial^2}{\partial x \partial z} \left[\eta \left(\frac{\partial^2 \chi}{\partial x^2} - \frac{\partial^2 \chi}{\partial z^2} \right) \right] + 2 \left(\frac{\partial^2}{\partial x^2} - \frac{\partial^2}{\partial z^2} \right) \left[\eta \frac{\partial^2 \chi}{\partial x \partial z} \right]. \quad (7.11)$$

To get Eqs. (7.10) and (7.11) the solid velocity is, following Sramek et al. (2012), split into incompressible flow and irrotational (compaction) flow velocity, which eventually allows us to solve for the stream function ψ and the irrotational velocity potential χ . The latter is given by the Poisson equation

$$\nabla^2 \chi = \vec{\nabla} \cdot \vec{v}_s. \quad (7.12)$$

The divergence term can be achieved from

$$\vec{\nabla} \cdot \vec{v}_s = -\vec{\nabla} \cot(\varphi(\vec{v}_f - \vec{v}_s)). \quad (7.13)$$

The transport of trace elements or isotopes in term of concentration is described by two mass conservation equations:

$$\frac{\partial c^s}{\partial t} + \vec{v}_s \cdot \vec{\nabla} c^s = 0 \quad (7.14)$$

$$\frac{\partial c^f}{\partial t} + \vec{v}_f \cdot \vec{\nabla} c^f = 0 \quad (7.15)$$

where c^s and c^f are the concentrations of the trace element in the solid and the fluid, respectively. As we do not allow for freezing or melting there is no exchange between the solid and the fluid. Non-equilibrium is assumed, meaning that no exchange between solid and fluid is assumed in order to achieve equilibrium. The equations are solved using an explicit upwind scheme.

Additionally to the concentration equations a marker, following the fluid velocity, is added. Advection of the markers is solved for using Eq. (7.15) with the 4th order Runge-Kutta method.

7.3 Results

7.3.1 Passing through an Enriched Layer

To test what happens when a solitary wave passes through a trace element enriched layer we start with a 1x1 model box. The whole box is partially molten with a background porosity φ_0 of 0.5% and a small Gaussian bell shaped melt perturbation is placed on top of it at $x' = 0.5$ and $z' = 0.2$. This perturbation does not exactly represent a solitary wave but will during ascend inevitably evolve into one. To take care of the buoyancy of the background melt an inflow of melt at the bottom and an outflow at the top is prescribed. On the left and the right mirroring boundary conditions are applied. Trace elements are equally distributed between solid and fluid, in a way that the total concentration ($c_{tot} = c^s (1 - \varphi) + c^f \varphi$) is equal to 10^{-6} in the whole model. Slightly above the initial wave an enriched layer is placed. Here the fluid concentration is increased to give a total concentration of $2 \cdot 10^{-6}$. Following Jordan et al. (2018) the ascending wave will, depending on its non-dimensional velocity, either encapsulate some of the enriched material of the layer or just pass through the layer, slightly lifting the material. In our model we achieve these two cases by varying the permeability-porosity relation exponent n between 2 and 3. For $n = 2$ the phase velocity is, at least for our waves with maximum melt fractions of about 40 (non-dimensional), always too slow ($v' \approx 2$) to incorporate material. In Fig. 7.1a one can see how the wave has passed through the layer and lifted it to about the order of the wave diameter. The wave itself is just slightly enriched after it has passed through the layer, probably still from the layer. With further ascending it will leave this enriched material behind.

In Fig. 7.1b the same model with $n = 3$ is shown. The wave has a velocity of about 8 times the background velocity. At the time where the wave arrives at $z' = 0.7$, the enriched layer just slightly ascended, as the wave is now much faster than this layer, that travels with the background velocity. At the point where the wave has pierced

through the layer it is totally disturbed. Material that was originally situated in the layer has now traveled upwards together with the wave. In the wave itself it looks like the material is situated within the wave, but as the wave is very fast, no material should be encapsulated in the center of the wave. In fact, it can be seen, that the center itself is slightly less enriched, compared to its surroundings. That we observe enriched material in the center of the wave at all might be due to numerical diffusion. Due to limited resolution a solitary wave in a Finite Difference model is never perfect

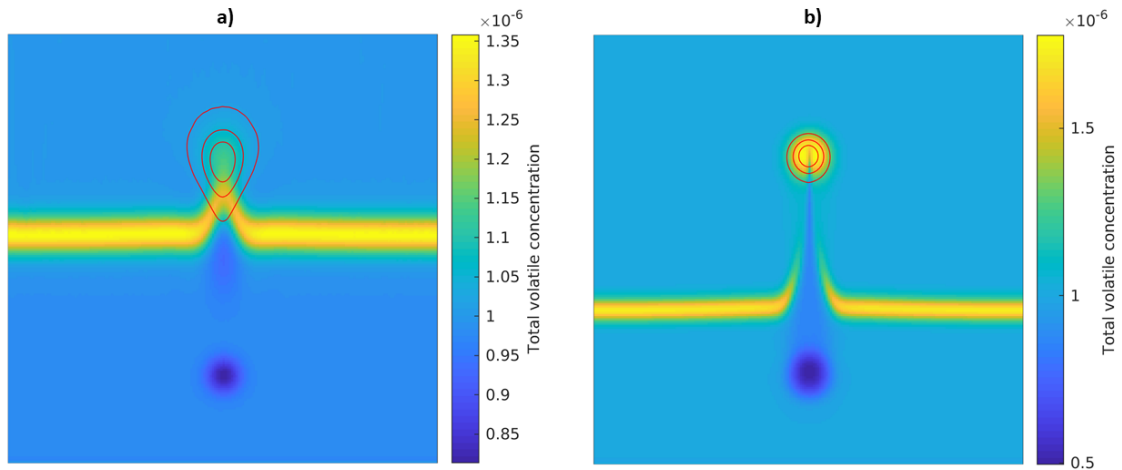


Figure 7.1: In color the total concentration of a trace element is shown at the point where the solitary waves have reached $z' = 0.7$. The red lines are contour lines of the melt fraction and show the position of the solitary wave. a) shows a slow, non-mass transporting solitary wave, using $n = 2$. b) shows a fast, mass transporting wave with $n = 3$.

and will inevitably lose volume, leaving a trail of melt behind during ascent. The loss in volume is compensated by a decrease in amplitude and as the phase velocity of a porosity wave is dependent on the amplitude the wave will become slower. Both, the maximum segregation velocity and the phase velocity decrease but the segregation velocity decreases faster and at some point, in the case of the segregation velocity being initially faster, the phase velocity will overtake and become dominant. Following Jordan et al. (2018), at this point the segregation is not fast enough to maintain the separated area in the wave and will no longer transport mass. In Fig. 7.2 both velocities of a fast solitary wave that started in the mass transport regime is shown. With time, both velocities decrease and at a velocity of about 3.6 the phase velocity becomes faster and we observe a regime switch from mass transporting solitary wave to non-transporting solitary wave. Jordan et al. (2018) observed this switch at a velocity of 3, but in contrast to them we did not neglect the solid shear (the first term on the right side of Eq. (7.9)) and did not apply the small porosity limit simplification, which

leads to a non-moving solid matrix.

A look at the marker field gives a better understanding of what happens to the material

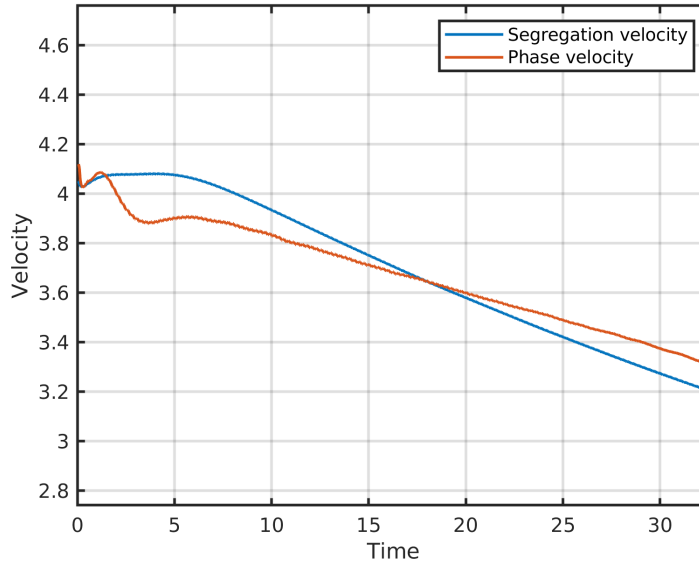


Figure 7.2: Non-dimensional phase and segregation velocity as a function of time of a solitary wave that is initially fast enough to transport mass but loses velocity and phase velocity becomes faster at $v' = 3.6$. The solitary wave shown needs some time to build up and receives the status of a solitary wave at about $t' = 8$ from where on both velocities decrease nearly linearly.

and where it is seated after the wave has passed through it, as numerical diffusion is not an issue. In Fig. 7.3 the marker fields to the models already shown in Fig. 7.1 are shown. The enriched layer is marked in brown while the background is yellow. In Fig. 7.3a the slow solitary wave gives the enriched layer just a lift and leaves the marker than behind after passing through. But in Fig. 7.3b one can see that the enriched material is not situated within the center of the wave as one might expect after investigating Fig. 7.1b. This supports the hypothesis that the enriched material in the center of the wave in Fig. 7.1b is there due to numerical diffusion. The layer is pushed upwards in front of the wave and is left behind at the sides of the wave. With further ascending the enriched layer in front of the wave will most certainly become thinner and thinner until it can no longer be seen in the marker field.

In Fig. 7.4 some marker trajectories are shown that explain what happens. The green markers are placed within the initial wave perturbation and the red markers are placed in the enriched layer. The green wave markers get trapped within the wave and stay there to the end. By the time they reach the enriched layer no material can be added to the wave center and the red layer markers make place to the wave by flowing to the side. After that they flow back to the x -Position before they were affected. Only the red marker directly in front of the wave travels all the way up in front of the wave, which can be hardly seen in the picture. The nearer the markers are to the center the further they travel upwards together with the wave.

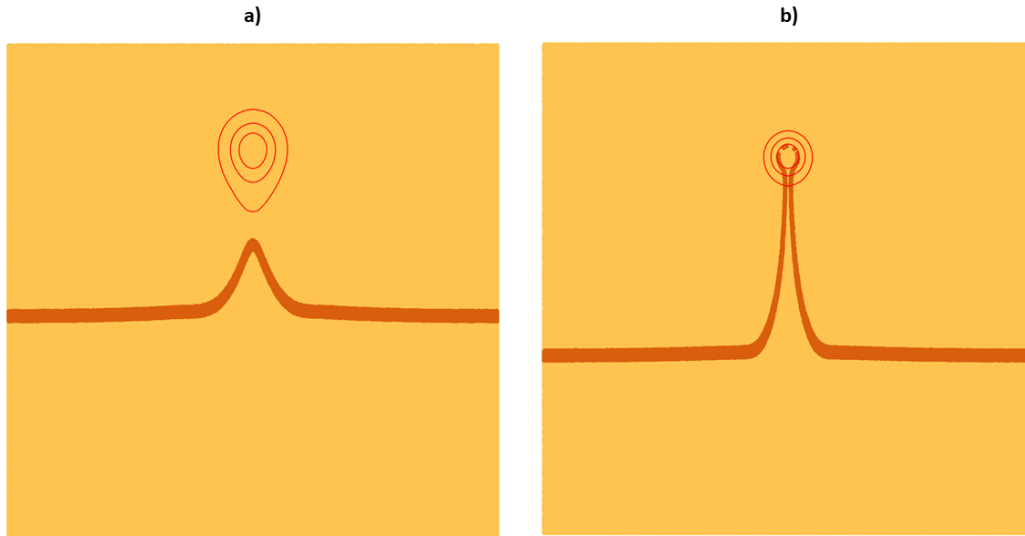


Figure 7.3: Marker fields from the models already shown in Fig. 7.2. The enriched layer is shown in brown. The background is yellow. The contour lines are the melt fraction and show the position of the solitary wave. The marker field is passive and has no influence on the model. a) $n = 2$, b) $n = 3$.

7.3.2 Origin of the Encapsulated Material

To investigate the origin of the material that gets trapped within the center of a solitary wave the initial conditions of the model are changed slightly. In Fig. 7.5a the model at $t' = 0$ is shown. Close to the bottom of the model a horizontal layer with a non-dimensional melt fraction of 8 is placed. Five different marker areas are introduced that have no influence on the model and just give information on where they were initially situated. The horizontal melt layer depicts a 1D wave in a 2D model which will during ascent break up into several 2D solitary waves because 1D waves are not stable in 2D (see Scott and Stevenson, 1986). To fasten this breakup a 1% white noise is added to the initial porosity perturbation. The material that leaves the upper boundary of the model enters the model again at the bottom.

In Fig. 7.5b the model is shown shortly before the solitary waves reach the upper boundary. From the horizontal perturbation 7 solitary waves have build up that contain material of the lower layers and pierce through the upper ones. Below the first front of solitary waves 2 secondary solitary waves build up that used the remaining melt that was not used for the first generation of solitary waves.

Zooming into one of these waves (Fig. 7.6) gives clearance about where the material in the center originated. Most of the material is from the third layer from the bottom and a smaller part is from the second layer. Nearly no material of the first layer, where the

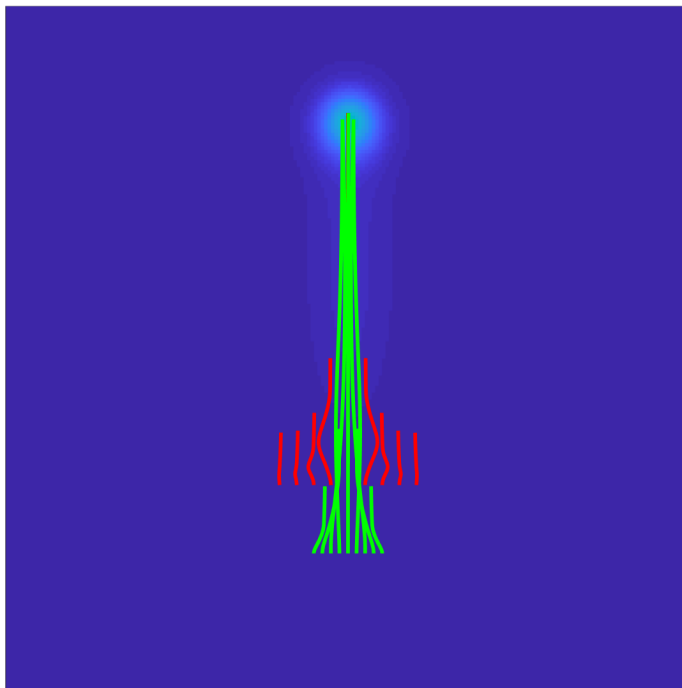


Figure 7.4: The figure shows trajectories of a few selected markers. The green markers were originally situated within the initial melt fraction perturbation and the red ones in the enriched layer. The colored background shows the melt fraction.

1D melt wave was placed, is situated in the wave and once the wave reaches the fourth layer the process of building up the separated area is already finished and no material from this layer can be build in. From this experiment one can expect that solitary waves contain material not, at least in full non-equilibrium, from its original melt layer but from a region that is 5-10 wave diameters above the original depth. Jordan et al. (2018) shows that assuming equilibrium, the transport of elements depends on the partition coefficient and some material from the original layer might be encapsulated in that case as well. The region from where material is build in the wave, in our case 5–10 wave diameters above the original depth, depends on the time that is needed to build up the wave. Dohmen and Schmelting (2021) shows that this time depends on the diapiric proportion of the ascent. The greater it is, the longer the wave needs to build up.

7.4 Conclusions

With our model, which solves the full equations without neglecting the shear stress term and the small porosity limit, the results of Jordan et al. (2018) could be reproduced. But in contrast to Jordan et al. (2018) we get the switch from transporting to non-transporting solitary waves at a non-dimensional velocity of 3.6 and not 3.

When a mass transporting wave travels through an enriched layer the enriched material is transported together with the wave but is not placed within the center of the

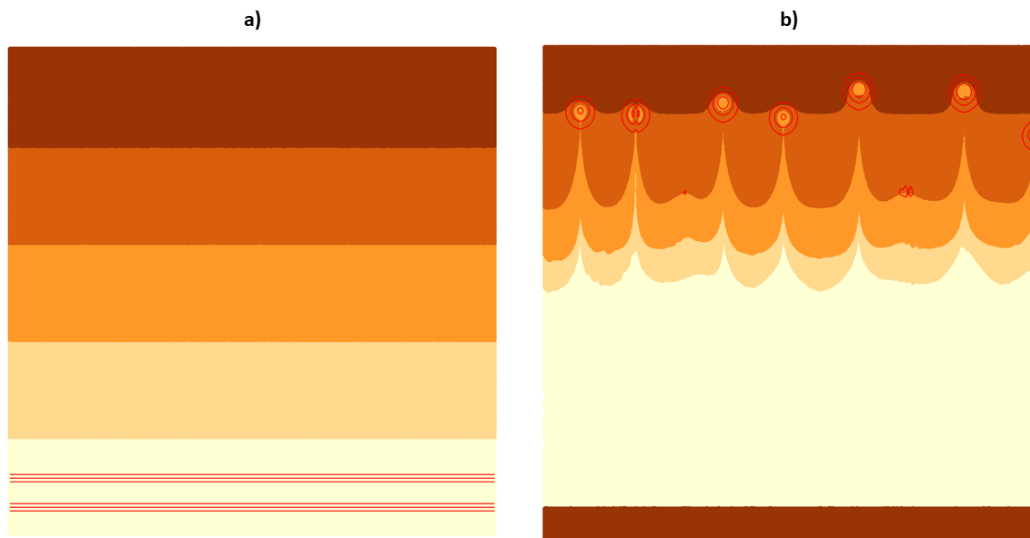


Figure 7.5: Marker fields a) in the beginning and b) at the end of a model with a 1D porosity wave initially placed at the bottom of the model box. The red lines are contour lines of the melt fraction. The different colors of the markers have no influence on the model and reflect only the original depth.

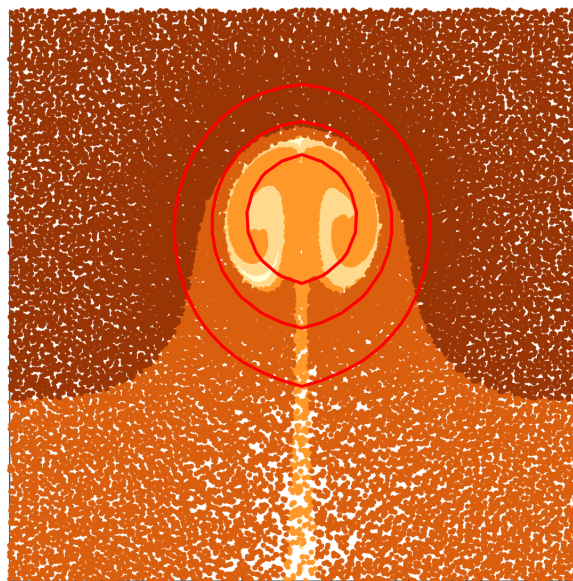


Figure 7.6: Figure shows a zoom of Fig. 7.5b on the second solitary wave from the right.

wave. The separated area stays intact and pushes the enriched material in front of it, but during ascent more and more of that material will get lost as it skids along the flanks of the wave. Only the material that is situated in the center of the wave during build up stays with the wave to the end. Material that is originally located at the

flanks of the wave is lost during ascent as well, depending on the size of the separated area.

Starting from a melt layer we can observe that the material which is transported with the wave is not from the original melt layer but from an area that is 5–10 wave diameters above this layer. This might be of particular importance for analyzing geochemical observations.

References

- Barcilon, V. and Lovera, O. M. (1989). Solitary waves in magma dynamics. *Journal of Fluid Mechanics*, 204(1989):121–133.
- Barcilon, V. and Richter, F. M. (1986). Nonlinear waves in compacting media. *Journal of Fluid Mechanics*, 164(1986):429–448.
- Dohmen, J. and Schmeling, H. (2021). Magma ascent mechanisms in the transition regime from solitary porosity waves to diapirism. *Solid Earth*, 12:1549–1561.
- Dohmen, J., Schmeling, H., and Kruse, J. P. (2019). The effect of effective rock viscosity on 2-D magmatic porosity waves. *Solid Earth*, 10(6):2103–2113.
- Jordan, J. S., Hesse, M. A., and Rudge, J. F. (2018). On mass transport in porosity waves. *Earth and Planetary Science Letters*, 485:65–78.
- McKenzie, D. (1984). The generation and compaction of partially molten rock. *Journal of Petrology*, 25(3):713–765.
- Omlin, S., Räss, L., and Podladchikov, Y. Y. (2018). Simulation of three-dimensional viscoelastic deformation coupled to porous fluid flow. *Tectonophysics*, 746(August 2017):695–701.
- Schmeling, H. (2000). *Partial melting and melt segregation in a convecting mantle*. Springer.
- Scott, D. R. and Stevenson, D. J. (1984). Magma solitons. *Geophysical Research Letters*, 11(11):1161–1164.
- Scott, D. R. and Stevenson, D. J. (1986). Magma ascent by porous flow. *Journal of Geophysical Research B*, 91(B9):9283.
- Sramek, O., Milelli, L., Ricard, Y., and Labrosse, S. (2012). Thermal evolution and differentiation of planetesimals and planetary embryos. *Icarus*, 217(1):339–354.
- Stubblefield, A. G., Spiegelman, M., and Creyts, T. T. (2020). Solitary waves in power-law deformable conduits with laminar or turbulent fluid flow. *Journal of Fluid Mechanics*, 886.
- Watson, S. and Spiegelman, M. (1994). Geochemical Effects of Magmatic Solitary Waves—I. Numerical Results. *Geophysical Journal International*, 117(2):284–295.
- Yarushina, V. M., Podladchikov, Y. Y., and Connolly, J. A. (2015). (De)compaction of porous viscoelastoplastic media: Solitary porosity waves. *Journal of Geophysical Research : Solid Earth*, pages 1–20.

Chapter 8

Conclusions

In the framework of this thesis two-phase flow in general and features that are solely connected to two-phase flow in particular were investigated. Namely, these features are solitary porosity waves and the transport of trace elements with melt which were examined using numerical models obtained by Finite Difference method. Several important observations and results could be obtained.

It could be shown that solitary porosity waves emerge out of a porosity perturbation, despite using much more realistic, quickly decreasing viscosity laws for the porosity dependence. These laws don't have a big influence on phase velocity or shape of the wave as long as the background porosity is rather small. However, bigger background porosities lead to a narrowing of the wave and a strong discrepancy between our models and analytical solutions can be observed. In general, with low melt fractions our models are in agreement to the analytical solutions that neglect the shear stress term, because the matrix shear contribution of the downward segregation flow is taken over by the increase of the compaction contribution. Furthermore, a switch of matrix velocity direction can be observed for different viscosity laws. For very low viscosities, the matrix in the center of the wave flows downwards contrary to the wave propagation direction, but in most cases the matrix flows upwards.

Additionally, it could be shown that, depending on the extent of a partially molten region the resulting ascent of melt may not solely occur by solitary waves or diapirism, but by a composed mechanism, where a diapir splits up into several solitary waves which then ascend together in formation. If the waves phase velocity is small, the formation will stay in the shape of a diapir, just slowly elongating due to the bigger main solitary wave at the very top. Depending on the ratio of the melt anomaly to the compaction length the ascent behavior can be classified into two regimes: (ia+b) Solitary wave a and b, and (ii) diapirism-dominated. In regime (ia) the matrix in the center of the wave sinks, contrary to the wave, and in (ib) the matrix ascends together with the wave, but very slowly. The further we are in regime (i) the less solitary waves will emerge, until only one emerges. In regime (ii), even though diapirism is dominant, solitary waves will emerge. Further in (ii), the time needed to build up a solitary wave becomes longer. Only at the end member of (ii) no solitary waves will emerge, as segregation is no longer possible.

When it comes to two-phase flow, not only solitary waves will appear, but redistri-

bution of trace elements, due to their behavior during melting, will occur. In this work, a model could be introduced giving a fully self-consistent physical description of trace element transport with melt, including melting, freezing and re-equilibration. In a closed convecting system, the convection cell will deplete in incompatible elements and an enriched layer will build up above it. The degree of enrichment in this layer will increase with every melting event, but eventually will reach an asymptotic value. A numerical 0D model could be introduced to explain the 2D model results. This 0D model consists of a convecting source region, where melting takes place, and an emplacement zone where the produced melt freezes again. Three additional parameters are introduced describing the ratio of molten material reaching the emplacement zone, the ratio of emplacement zone to source region, and the ratio of the sizes of partially molten region to whole source region. A simple equation can be used to fit the numerical results. Only the ratio of melt- to source region describes the time needed to reach the asymptotic value. All others, including trace element parameters, only affect the maximum enrichment reached.

Whether solitary waves are able to transport material just recently was shown, as they were thought to just pass through material during ascent. In this work it could be demonstrated that solitary waves, without neglecting the shear stress term, are able to transport material as well. The transition between mass transporting and non-transporting waves depends on the phase velocity. While earlier studies saw this switch at a non-dimensional velocity of 3, we, applying the full equations, see it at 3.6. Starting from a melt layer it could be shown, that the material captured within the wave is not from this melt layer, but from a region, depending on model parameters, approximately 5 to 10 wave diameters above the original melt zone. As the wave needs some time and distance to emerge and establish the separated area in the center, the material is from the area where this transition is completed.

This thesis helped to achieve better insights on under which conditions solitary waves build up and what parameters are important in this kind of modeling. In publication 1,2 and 4 solitary waves are observed while in publication 3 no solitary waves build up. Here, a subduction back arc is modeled and melting and freezing is possible, which is known to suppresses the emergence of solitary waves and might explain why we do not observe them. Another point is that no background porosity is prescribed. In order for solitary waves to build up it is necessary to make decompaction in front of the wave possible, which is usually achieved by applying a background porosity. One could see an uprising plume in the model as a partially molten background, but melt fractions here are relatively high, leading to very large compaction lengths and resulting solitary waves would be larger than the model domain. Additionally, diapiric rise might be too dominant to allow for solitary waves to build up in the short time of the plume rising as it was shown in publication 2. However, solitary waves might be possible in back arcs where a broader area is partially molten to a smaller degree. In that case numerical resolution might play an important role in order to sufficiently resolve the small waves in such a broad model domain.

In publication 3 it could be shown that two-phase flow is an important tool to model the transport of trace elements. Even though solitary waves cannot be observed here, modeling these waves from publication 1 and 2, and adding the capability for trans-

8. *Conclusions*

port of trace elements with melt, which is done in the unpublished manuscript, shows that those waves might have significant influence on geochemical markers and further work has to be carried out to get an idea on how this is important in a more realistic model as in publication 3.

Kapitel 9

Fazit

In Rahmen dieser Arbeit wurde Zwei-Phasen Strom im Allgemeinen, und im Speziellen Besonderheiten, die nur Zwei-Phasen Strom zuzuordnen sind, untersucht. Zum einen sind dies solitäre Porositätswellen und zum anderen der Transport von Spurenelementen in Schmelze, was mit Hilfe von numerischen Finite Differenzen Modellen untersucht wurde.

Es konnte gezeigt werden, dass sich solitäre Wellen aus einer Porositätsstörung herausbilden können, und dies obwohl sehr viel realistischere, schnell abfallende Viskositätsgesetze für die Porositätsabhängigkeit von Schmeling et al. (2012) genutzt wurden. Diese Gesetze haben keinen großen Einfluss auf die Phasengeschwindigkeit und Form der Welle, solange die Hintergrundporosität relativ klein ist. Höhere führen jedoch zu einem Verengen der Welle und zu einer zunehmenden Diskrepanz zu analytischen Lösungen. Im Allgemeinen sind unsere Modelle bei kleinen Schmelz-Porositäten im Einklang mit den analytischen Lösungen, welche den Scher-Term vernachlässigen, da der Scheranteil der Matrix durch einen Anstieg in der Kompaktion ausgeglichen wird. Weiterhin konnte ein Wechsel der Richtung der Matrixgeschwindigkeit für verschiedene Viskositäten beobachtet werden. Für sehr kleine Viskositäten strömt die Matrix im inneren der Welle nach unten, entgegen der Wellenausbreitungsrichtung. Allerdings strömt sie in den meisten Fällen aufwärts.

Zusätzlich konnte gezeigt werden, dass, abhängig von der Ausdehnung der partiell geschmolzenen Zone, der Aufstieg nicht alleine durch Diapirismus oder solitäre Wellen, sondern viel mehr durch eine Mischung von beiden geschieht. Dabei spaltet sich die Störung in zahlreiche solitäre Wellen auf und steigt dann in Formation auf. Sind die Phasengeschwindigkeiten der Wellen klein, behalten sie ihre Diapir-Formation bei und werden nur etwas länger, da die Hauptwelle etwas größer ist als die anderen. Abhängig vom Verhältnis der Größe der Schmelz-Störung und der Kompaktionslänge kann der Aufstieg in zwei Regime unterteilt werden: (ia+b) Solitäre Wellen a und b, und (ii) Diapirismus-dominierend. In Regime (ia) sinkt die Matrix im Inneren der Welle, während sie in (ib) zusammen mit der Welle aufsteigt. Je weiter man in Regime (i) ist, umso weniger solitäre Wellen entstehen. Zuletzt entsteht nur noch eine einzige. In Regime (ii) entstehen, obwohl Diapirismus dominant ist, immer noch solitäre Wellen, jedoch nimmt die Zeit zur Entwicklung einer Welle mit zunehmender Tiefe im Regime zu. Nur im Endglied von (ii), wo Segregation nicht mehr möglich ist, können keine

Wellen mehr entstehen.

Beim Zwei-Phasen Strom treten nicht nur solitäre Wellen auf, es findet aufgrund des Verhaltens während der Schmelze auch eine Umverteilung von Spurenelementen statt. In dieser Arbeit wird ein Modell eingeführt welches eine konsistente physikalische Beschreibung von Spurenelement-Transport in Schmelze, einschließlich Aufschmelzen, Gefrieren und Re-Equilibrierung beschreibt. In einem geschlossenen konvektierenden System wird die Konvektionszelle an inkompatiblen Spurenelementen verarmen und eine angereicherte Schicht darüber entsteht. Der Grad der Anreicherung nimmt mit jedem Schmelzereignis zu, aber wird sich schließlich einem asymptotischen Wert annähern. Ein numerisches 0D-Modell wurde eingeführt, welches die 2D-Ergebnisse erklärt. Es besteht aus einer konvektierenden Quellzone, in der Material aufgeschmolzen wird, und einer Ablagerungszone, in der die Schmelze wieder gefriert. Drei zusätzliche Parameter wurden eingeführt, die den Anteil der Schmelze, die die Ablagerungszone erreicht, das Verhältnis von Quellregions- zu Ablagerungszonen-Größe, und das Verhältnis von partiell geschmolzener Region zu ganzer Quellregion, beschreiben. Zur Beschreibung der numerischen Gleichung wird eine einfache Gleichung genutzt. Nur das Verhältnis von Schmelz- zu Quellregion beeinflusst dabei die Zeit, die benötigt wird, um sich dem asymptotischen Wert anzunähern. Alle anderen, einschließlich der Spurenelement Parameter, beeinflussen nur den maximalen Grad der Anreicherung. Dass solitäre Wellen Material transportieren können wurde erst kürzlich gezeigt. Zuvor wurde angenommen, dass eine Welle Material nur durchströmt. Das Verhalten für das vollständige Gleichungssystem für Zwei-Phasen Strom, welche den Scherterm nicht vernachlässigen, konnte in dieser Arbeit bestätigt werden. Der Übergang von transportierenden zu nicht-transportierenden Wellen wurde dabei bei einer non-dimensionalen Phasengeschwindigkeit von 3.6 gefunden und nicht 3, für die einfacheren Gleichungen. Startet man von einer Schmelzschicht konnte gezeigt werden, dass das Material, das im inneren der Welle eingefangen ist, nicht von der ursprünglichen Schmelzschicht stammt sondern von einer Schicht etwa 5 bis 10 Wellendurchmesser darüber. Da die Wellen einiges an Zeit und Strecke benötigen, um sich zu bilden, und den abgetrennten Bereich aufzubauen, stammt das Material von dort, wo dieser Übergang vollzogen wurde.

Diese Thesis hat dabei geholfen einen besseren Einblick darin zu erhalten unter welchen solitäre Wellen entstehen können und welche Parameter dabei entscheidend sind. In den Publikationen 1,2 und 4 konnte solitäre Wellen beobachtet werden, während in Publikation 3 sich keine gebildet haben. Hier wurde ein Subduktions Backarc modelliert und Schmelzen und Gefrieren ist möglich, was, wie bekannt ist, das Aufkommen von solitären Wellen verhindern kann. Das könnte das Fehlen dieser Wellen erklären. Ein anderer Punkt ist, dass keine Hintergrund-Porosität vorgegeben ist. Um das Aufkommen von Porositätswellen zu ermöglichen, ist es nötig Dekompaktion vor der Welle zu erlauben, was normalerweise durch ein porösen Hintergrund erreicht wird. Man könnte den aufsteigenden Plume als einen partiell geschmolzenen Hintergrund annehmen, doch die Schmelzanteile sind vergleichsweise groß und führen zu sehr großen Kompaktionslängen. Resultierende Wellen wären größer als die Modell-Domäne. Hinzu kommt, dass Diapirismus zu dominant sein könnte um Wellen zu erlauben in der kurzen des Aufstiegs sich zu bilden. Solitäre Wellen können sich potenziell bilden, wenn

ein größerer Bereich im Modell zu einem geringen Teil geschmolzen ist. Dann spielt die numerische Auflösung eine wichtige Rolle, da die kleinen Wellen in so einer großen Modell-Domäne hinreichend aufgelöst werden müssten.

In Publikation 3 konnte gezeigt werden, dass Zwei-Phasen Strom ein wichtiges Werkzeug ist den Transport von Spurenelementen zu modellieren. Auch wenn sich hier solitäre Wellen nicht bilden, konnten Modelle von diesen Wellen aus Publikation 1 und 2, zusammen mit der Möglichkeit des Spurenelement-Transports, was im letzten Manuskript getan wurde, zeigen, dass sie einen signifikanten Einfluss auf geochemische Marker haben können. Mehr Arbeit ist nötig um die Wichtigkeit bei realistischeren Modellen wie in Publikation 3 zu untersuchen.

Kapitel 10

Zusammenfassung

Das Schmelzen von Gesteinen im inneren der Erde ist ein häufig vorkommendes Phänomen und kann an vielen verschiedenen Orten auf der Oberfläche der Erde beobachtet werden. Hier ist die Schmelze durch den Mantel und die Kruste geströmt bis sie schließlich die Oberfläche erreicht und dort Vulkane oder sogar ganze lithographische Schichten, wie zum Beispiel die ozeanische Kruste, bildet. Oft ist diese Schmelze eine gute Quelle von Informationen die wir aus den Tiefen der Erde ziehen können und es ist daher unerlässlich die Prozesse des Schmelzens und deren Segregation durch die feste Matrix zu fassen. Um ein besseres Verständnis davon zu erhalten, untersucht diese Thesis sie mit Hilfe von numerischen Modellen.

Der benutzte Ansatz ist ein so genanntes Zwei-Phasen Strom Modell, welches die Fähigkeit von Schmelze, durch eine viskos verformende, poröse Matrix zu segregieren, beschreibt. Eine Besonderheit von Zwei-Phasen Strom ist das Auftreten von solitären Porositätswellen. Dies sind Wellen von lokal erhöhter Porosität, die durch eine partiell geschmolzene Matrix, mit konstanter Geschwindigkeit und gleichbleibender Form, aufsteigen. Angetrieben werden sie durch Dekompaktion und Kompaktion vor und hinter der Welle.

Ein Parameter beim Modellieren von porösen Wellen ist das Viskositätsgesetz für Scher- und Volumenviskosität. In früheren Studien wurden diese meist stark vereinfacht, indem die Porositäts-Abhängigkeit unterschätzt oder sogar der Einfluss der Porosität auf Volumenviskosität gänzlich vernachlässigt wird. In dieser Thesis werden realistischere Modelle von Schmeling et al. (2012) verwendet. Sie basieren auf vorgegebenen Schmelzgeometrien, bestehend aus Filmen und Röhren, woraus Viskositäten numerisch berechnet werden. Sie nehmen bei kleinen Porositäten bereits stark ab. Die verwendeten Gesetze führen bereits bei Porositäten von 20–40% zu kompletter Disaggregation. Die Ergebnisse der numerischen Berechnung wurden parametrisiert und anschließend in einen bestehenden 2D Finite Differenzen-Mantel-Konvektions Code mit Zwei-Phasen Strom eingearbeitet. Der Code, FDCON, wurde verwendet um die Ausbreitung von Porositätswellen zu modellieren.

Eine Gauß-förmige Welle wurde mit einer vorgeschriebenen Amplitude und Weite in eine partiell leicht aufgeschmolzene Region (Hintergrundporosität) platziert. Die Form einer Gauß-Glocke entspricht nicht der einer solitären Welle, kommt dieser jedoch nahe und wird verwendet, da die exakte Form einer zweidimensionalen solitären Welle nicht

bekannt ist.

Es konnte gezeigt werden, dass eine anfängliche Gauß-Welle sich innerhalb kürzester Zeit in eine solitäre Welle umwandelt, auch mit den neuen realistischeren Viskositäten. Je nachdem wie groß die Anfangs-Welle im Vergleich zur letztendlichen Porositätswelle ist, passt sich die Amplitude an. Nach dem Erreichen der Dispersionskurve, nimmt die Amplitude aufgrund von numerischen Ungenauigkeiten ab und so können mit einigen wenigen Modellen bereits große Teile der Dispersionskurve abgedeckt werden. Es konnte weiterhin gezeigt werden, dass, solange die Hintergrundporosität relativ klein ist, sich die Wellen nicht stark von vereinfachten semi-analytischen Lösungen unterscheiden. Mit zunehmender Hintergrundporosität nimmt der Unterschied jedoch drastisch zu. Höhere Porositäten von bis zu 15% führen zu bis zu 20% geringeren Phasengeschwindigkeiten. Das liegt unter anderem daran, dass bei höheren Porositäten die Disaggregations-Grenze erreicht werden kann. Die einzelnen festen Körner sind nicht mehr mit einander verbunden und die Viskosität nimmt schlagartig ab. Dieses Verhalten ist, erstens, bei früheren Untersuchungen mit vereinfachten Viskositätsgesetzen nicht berücksichtigt worden und, zweitens, unterliegt anderen physikalischen Gesetzen, die in unserem Modell nicht berücksichtigt werden und eventuell das Aufkommen von solitären Wellen sogar verhindern könnten.

Auch das Ändern der Geometrie des Schmelz-Netzwerks hat einen enormen Einfluss. Bei 100% Filmen und variierenden Seitenverhältnissen der einzelnen Filme ändert sich zwar die Phasengeschwindigkeit nicht signifikant, jedoch ändert sich die Weite der Welle um über 25%. Bei einer Schmelzgeometrie bestehend aus 50% Filmen und 50% Röhren, bleiben Geschwindigkeit und Weite der Welle nahezu konstant.

Die Matrix-Geschwindigkeit im Zentrum der Welle hat vergleichsweise wenig Einfluss auf die Welle. Verringert man jedoch das Seitenverhältnis der Filme, führt das zu einer Vorzeichenänderung in der Matrixgeschwindigkeit. Für mittel bis hochviskose Viskositäten bewegt sich die Matrix mit der Welle nach oben. Niedrige Viskositäten führen zu einem Absinken der Matrix, entgegen der Wellenbewegung.

Von besonderem Interesse bei solitären Porositätswellen ist, wann und wie sie entstehen. In bestimmten Fällen bilden sich Diapire, in anderen wiederum bilden sich eine oder sogar mehrere solitäre Wellen aus einer einzigen Gauß-Glocken-förmigen Störung. Hier ist wichtig zu erwähnen, dass solitäre Wellen immer eine gleiche Größe von etwa 3 bis 4 Kompaktionslängen haben, während Diapire jegliche Größenordnungen annehmen können. Die Kompaktionslänge ist eine charakteristische Länge beim Zwei-Phasen-Strom und gibt die Größenordnung wieder in der Kompaktion an einer impermeablen Grenzschicht stattfindet. Sie hängt von der Permeabilität der Matrix, sowie der Matrix- und Fluidviskosität ab. Ein Vergrößern der Anfangsstörung, bzw. das Verringern der Kompaktionslänge, führt somit zu einer kleineren solitären Welle im Vergleich dazu. Um den Übergang von Diapirismus zu solitären Wellen besser zu verstehen, kann man Segregations- und Stokeseschwindigkeit der Anfangsstörung bestimmen und vergleichen. Es zeigt sich, dass der Anfangsstörungs-Radius in Bezug auf die Kompaktionslänge hier entscheidend ist. Große Radien führen zu einer Stokes-dominierenden Bewegung, während für kleinere Radien Segregation dominiert. Die Stokeseschwindigkeit stellt dabei die Geschwindigkeit des aufsteigenden Diapirs durch Gravitation dar. Auch die Amplitude der Störung spielt eine Rolle, wobei größere Amplituden eher

solitäre Wellen bzw. Segregation stärken.

Zur besseren Untersuchungen wurden 2D-Modellierungen in einem sich bewegendem Koordinatensystem durchgeführt. Die Auflösung der Kompaktionslänge im Modell ist ein wichtiger Faktor, da diese hinreichend aufgelöst werden muss damit sich überhaupt solitäre Wellen bilden können und deren Eigenschaften zufriedenstellend genau wiedergegeben werden. Zu grobe Auflösungen verwaschen die Welle, führen zu kleineren Amplituden und erlauben nicht das Aufkommen von sekundären Wellen. Erst bei einer Auflösung, bei der eine Kompaktionslänge durch mindestens zwei Gitterlängen aufgelöst wird, sind alle Eigenschaften erkennbar.

Es wurden verschiedene Anfangsstörungs-Radien in Bezug auf die Kompaktionslänge gewählt. Mit der Zeit bilden sich daraus immer solitäre Wellen. Nur für den Fall einer Kompaktionslänge von null, d.h. Segregation ist nicht möglich, kann sich auch über lange Zeit keine solche Welle bilden. Selbst im Stokes-dominierenden Grenzbereich bildet sich an der Spitze der aufsteigenden Störung eine Welle, die sich jedoch nur unmerklich schneller bewegt und sich dementsprechend auch über längere Aufstiegszeiten nicht von den Störung trennen kann. Im Übergangsbereich von Diapirismus zu solitären Wellen bilden sich mehrere sekundäre Wellen, welche zusammen mit der Störung aufsteigen. Die primäre Welle ist jedoch etwas größer und damit schneller, was zu einer Verlängerung in der Vertikalen der Störung führt.

Auch wenn in allen Fällen, in denen Segregation möglich ist, sich irgendwann solitäre Wellen bilden, heißt das nicht, dass sich diese auch bilden. Mit zunehmenden Störungsradius nimmt auch die Zeit zu, die benötigt wird, damit sich eine Welle ausbildet. Sie nimmt exponentiell zu und im Diapirismus-dominanten Bereich kann sie zu groß sein, als dass sich in natürlichen Umgebungen welche bilden könnten.

Bei der Betrachtung vom Massenfluss von Matrix und Fluid, kann man den Einfluss des zunehmend stärker werdenden Diapirismus bei zunehmendem Radius erkennen. Bei einem Anfangsstörungs-Radius von 2,4 mal der Kompaktionslänge wird das Aufströmen des Fluids durch ein Herabströmen der Matrix kompensiert. Beides findet hauptsächlich innerhalb der Wellenregion statt. Nimmt der Radius zu, wird die solitäre Welle kleiner. Das Aufströmen des Fluids findet fast ausschließlich innerhalb der Wellenzone statt und wird durch ein Herabströmen der Matrix, hauptsächlich außerhalb der Wellenregion, kompensiert. Weiter zunehmender Radius führt zu einem Aufströmen der Matrix in der Wellenregion, wird jedoch auch durch ein stärkeres Herabströmen an den Rändern kompensiert.

Mit der Hilfe von Massenfluss der Schmelze und Matrix, und der Geschwindigkeit der Matrix werden Koeffizienten definiert, mit denen man wiederum zwei Regime bestimmen kann. In Regime (ia) und (ib) sind solitäre Wellen dominant, wobei in (ia) die Matrix im inneren der Welle nach unten sinkt, während sie in (ib) mit der Welle aufsteigt. Je weiter man in diesem Regime ist, desto weniger solitäre Wellen bilden sich aus der Anfangsstörung, bis sich zuletzt nur eine einzige ausbildet. In Regime (ii) ist Diapirismus dominant, es bilden sich jedoch immer noch solitäre Wellen aus, die nur unmerklich schneller sind als der Diapir. Je tiefer man in diesem Regime ist, desto länger ist die benötigte Zeit zum Umwandeln in eine Welle. Das Endglied von (ii) ist reiner Diapirismus, welcher jedoch nur erreicht wird wenn Segregation gänzlich verhindert wird.

Vor allem im Bereich des Übergangs von solitären Wellen zu Diapirismus-dominierend spielt die räumliche Auflösung eine wichtige Rolle. Hier wird die Kompaktionslänge so klein, dass sie nur schwierig hinreichend aufgelöst werden kann, solitäre Wellen haben gleichzeitig aber immer noch einen großen Einfluss auf den Aufstieg. Weiter im Diapirismus-dominierenden Regime kann zwar die Kompaktionslänge nicht mehr aufgelöst werden, solitäre Wellen sind aber kaum noch relevant für den Aufstieg des Diapirs als Ganzes.

Ein anderer wichtiger Aspekt von Zwei-Phasen Strom ist die mögliche Umverteilung von Elementen. Inkompatible Elemente bevorzugen es während eines Schmelzvorgangs vom Kristallgitter in die Schmelze zu gehen. Diese angereicherte Schmelze segregiert wegen niedrigerer Dichte durch die poröse Matrix nach oben und sorgt so für eine Umverteilung der Elemente hin zu höheren Lagen.

Als Teil dieser Arbeit wurde ein bestehender Zwei-Phasen Strom-Konvektions Code, FDCON, erweitert um den Transport von Spurenelementen in der Schmelze zu ermöglichen. Hierzu werden zwei weitere Massenerhaltungs-Gleichungen, eine für die Element-Masse in der Schmelze und eine in der Matrix, voll konsistent gelöst. Dies bezieht Schmelzen, Gefrieren und Re-Equilibrierung ein. Der Quellterm der Gleichungen beinhaltet die Konzentrationen des zu beobachtenden Elements in Matrix und Schmelze und den Partitionierungs-Koeffizienten zwischen Matrix und Schmelze. Abhängig ob gefroren oder geschmolzen wird, müssen unterschiedliche Quellterme gelöst werden. Die Re-Equilibrierung wird unter Einsatz der Reaktionszeit berechnet. Dabei wird die Differenz von aktuellen Konzentrationen hin zu Equilibrium-Konzentrationen berechnet.

Ein Modell mit porositäts- und temperaturabhängiger Viskosität wurde erzeugt. Es bildet sich eine Konvektionszelle im unteren, niedrig-viskosem Bereich des Modells, wo sich von Zeit zu Zeit ein partiell geschmolzener Plume bildet, der in die hoch-viskose Schicht darüber eindringen kann.

Hier konnte gezeigt werden, wie sich inkompatible Elemente in einem partiell geschmolzenen Plume am oberen Ende anreichern und schließlich abtrennen, um dort zu verweilen. Während des Aufstiegs eines Plumes bewegt sich die Schmelzfront mit einer größeren Geschwindigkeit als die Matrix nach oben. Währenddessen sammelt sich angereicherte Schmelze im oberen Teil des Plumes an und sorgt dort für eine erhöhte totale Konzentrationen. Zu einem bestimmten Zeitpunkt überholt die Matrix-Geschwindigkeit die der Schmelzfront und sorgt so für ein Abtrennen der angereicherten Matrix von der Schmelze. Das Verzögern der Schmelzfront ist erklärbar durch das Sinken der Temperatur und dem Anstieg der Viskosität, welche Dekompaktion erschwert.

In einer konvektierenden Zelle wird jedes Schmelzereignis zu einer Anreicherung führen und gleichzeitig die Quellregion verarmen. Ein 0D-Modell wurde erstellt, welches dieses Anreicherungsverhalten widerspiegelt. Es besteht aus zwei Zonen: einer Quellregion in der Material aufgeschmolzen wird und einer Ablagerungszone in der dieses Material wieder gefriert und abgelagert wird. Dieses Modell beinhaltet sechs frei wählbare Parameter. Darunter fallen das *Transportverhältnis*, das *Ablagerungs-Volumenverhältnis*, das *Schmelzbereichsverhältnis* und der maximale Schmelzgrad. Sie beschreiben Aspekte, die nur schwierig abzuschätzen sind. Dazu kommen Element-abhängige Parameter

wie Partitionierungs Koeffizient und Re-Equilibrierungskonstante bzw. Reaktionszeit. Es wird gezeigt, dass die Anreicherung einen asymptotischen Wert annimmt, welcher von allen Parametern beeinflusst wird. Die Zeit, die benötigt wird, diesen zu erreichen hängt jedoch nur vom *Verarmungsverhältnis* ab.

Die Retentionszahl, also der Widerstand den ein Fluid beim Segregieren durch die poröse Matrix erfährt, hat einen enormen Einfluss auf den Grad der Anreicherung. Eine niedrigere Retentionszahl, d.h. stärkere Segregation, führt zu kleineren Schmelzgraden. Diese führen wiederum zu deutlich höheren Viskositäten, was das Eindringen in die hoch viskose Schicht darüber erschwert. Das hat einen enormen Einfluss auf die Dynamik des Modells und führt zu geringeren Eindringtiefen. Der Grad der Anreicherung nimmt jedoch trotzdem mit abnehmender Retentionszahl zu.

Die Reaktionszeit, also die Zeit die zur Re-Equilibrierung benötigt wird, hat keinerlei Einfluss auf die Dynamik des Modells, führt jedoch zu unterschiedlichen Graden der Anreicherung. Kleinere Reaktionszeiten, also schnellere Re-Equilibrierung, führen zu deutlich kleineren Anreicherungen.

Auch wenn das Modell nicht den Transport von Schmelze and die Oberfläche ermöglicht, können dennoch die Fluid-Konzentrationen im Modell genutzt werden, um sie mit realen Messungen zu vergleichen. Der Modellaufbau könnte beispielsweise für einen Vulkan-Bogen an einer Subduktionszone genutzt werden. Hier zeigt sich, dass bei unseren Modellen eher große Retentionszahlen zu passenderen Werten führen. Kleinere Retentionszahlen sind jedoch wahrscheinlicher in der Natur. Diese Diskrepanz lässt sich womöglich durch den Modellaufbau und die Rahmenbedingungen erklären, die diesem Bogen nicht gut genug entsprechen.

Auch solitäre Porositätswellen können Material transportieren. Dies wurde erst kürzlich bestätigt und wurde für viele Jahre für nicht möglich gehalten. Es wurde gezeigt, dass es einen Übergang, abhängig von der non-dimensionalen Geschwindigkeit der Welle, gibt. Bei langsamen Wellen wird Material in die Welle eingezogen, aber sofort auch wieder ausgetragen. Bei schnellen Wellen bildet sich allerdings ein abgetrennter Bereich im inneren der Welle, welcher Material einschließt und mit sich mitträgt bis die Welle irgendwann zerfällt. Mit unseren vollen Gleichungen ohne Vereinfachungen erhalten wir diesen Übergang bei 3.6.

Benutzt man Marker, um den Ursprung des Materials im inneren der Welle zu untersuchen, stellt man fest, dass es nicht aus der ursprünglichen Schmelzschicht stammt, sondern aus einem Bereich etwas oberhalb. Eine solitäre Welle benötigt Zeit bis sie sich aus einer Schmelzschicht in mehrere Wellen aufspaltet. Bis dies nicht passiert ist, ist auch der abgetrennte Bereich nicht im Stande Material aufzunehmen. Es stammt aus einer Schicht etwa 5 bis 10 Wellen-Durchmessern oberhalb der Schmelzschicht.

Im Rahmen dieser Arbeit konnten zahlreiche Erkenntnisse bezüglich Zwei-Phasen Strom und dessen Besonderheiten gewonnen werden. Insbesondere konnte gezeigt werden, unter welchen Bedingungen sich solitäre Porositätswellen bilden und wann diese wichtig für das gesamte Modell sind. Es konnte gezeigt werden, dass sich solitäre Wellen auch bei realistischeren Viskositätsgesetzen bilden und wie groß der Einfluss auf Form und Geschwindigkeit der Welle ist. Weiterhin konnte gezeigt werden, dass solitäre Wellen auch mit der vollen physikalischen Beschreibung in der Lage sind Material zu transportieren. Es konnten Einsichten in den Ursprung des Materials innerhalb

der Welle gewonnen werden. Zuletzt konnte eine voll konsistente Beschreibung für den Transport von Spurenelementen in Schmelze mit Hilfe von Zwei-Phasen Strom eingeführt werden, welche Schmelzen, Gefrieren und Re-Equilibrierung beinhaltet.

Personal Contribution to Publications

This doctoral thesis was created under the supervision of Prof. Harro Schmeling. All publications and manuscripts are the result of a collaboration of the co-authors mentioned below the titles of each manuscript and me. My personal contributions to each manuscript are described in the following:

Publication 1: The effect of effective rock viscosity on 2D magmatic porosity waves

I am the first of three authors of this publication. I prepared the majority of the script and all figures. I carried out all models and evaluated the results. I changed parts of the code FDCON to allow for the modelling of solitary waves using new viscosity laws. The manuscript was reviewed by two reviewers and I edited it according to their comments.

Publication 2: Magma ascent mechanisms in the transition regime from solitary porosity waves to diapirism

I am the first of two authors of this publication. I prepared the script and all figures. I carried out all models and evaluated the results. I modified the code to have a moving coordinate system, following the maximum of the melt fraction. The manuscript was reviewed by three reviewers and I edited it according to their comments.

Publication 3: Modeling trace element transport in melt using two-phase flow: Investigation of element redistribution in the upper earth

I am the first of three authors of this publication. I prepared the the script and all figures. I carried out all models and evaluated the results. To model the transport of trace elements, I extended the code FDCON to be capable for it. The manuscript is submitted.

Unpublished manuscript: Transport of volatiles and trace elements in solitary porosity waves

I am the first of two authors of this manuscript. I prepared the script and all figures. I carried out all models and evaluated the results. I changed the code FDCON to have marker following the fluid. So far, the manuscript is not published or submitted.

Eidesstattliche Erklärung

Ich erkläre hiermit, dass ich die vorgelegte Dissertation über *Numerical Modeling of two-phase flow for solitary porosity waves and transport of trace elements within melt* selbstständig angefertigt und mich anderer Hilfsmittel als der in ihr angegebenen nicht bedient habe, insbesondere, dass alle Entlehnungen aus anderen Schriften mit Angabe der betreffenden Schrift gekennzeichnet sind. Ich versichere, die Grundsätze der guten wissenschaftlichen Praxis beachtet, und nicht die Hilfe einer kommerziellen Promotionsvermittlung in Anspruch genommen zu haben.

Ort, Datum

Unterschrift